

**Response of the Ionosphere-Plasmasphere System to  
Periodic Forcing**

by

**Nicholas M. Pedatella**

B.S., The Pennsylvania State University, 2007

A thesis submitted to the  
Faculty of the Graduate School of the  
University of Colorado in partial fulfillment  
of the requirements for the degree of  
Doctor of Philosophy  
Department of Aerospace Engineering Sciences

2011

This thesis entitled:  
Response of the Ionosphere-Plasmasphere System to Periodic Forcing  
written by Nicholas M. Pedatella  
has been approved for the Department of Aerospace Engineering Sciences

---

Kristine M. Larson

---

Jeffrey M. Forbes

Date \_\_\_\_\_

The final copy of this thesis has been examined by the signatories, and we find that both the content and the form meet acceptable presentation standards of scholarly work in the above mentioned discipline.

Pedatella, Nicholas M. (Ph.D., Department of Aerospace Engineering Sciences)

Response of the Ionosphere-Plasmasphere System to Periodic Forcing

Thesis directed by Kristine M. Larson and Jeffrey M. Forbes

The role of different mechanisms for generating periodic variability in the ionosphere and plasmasphere is studied in this dissertation. The impact of vertically propagating waves of lower atmospheric origin on introducing periodic spatial and temporal variability in the ionosphere and plasmasphere is first investigated. This is comprised of several different aspects. Initial focus is on the seasonal, local time, and altitude dependence of longitude variations due to nonmigrating tides in the F-region and topside ionosphere/plasmasphere using a combination of observations and numerical models. This is facilitated by the development of a new method for mitigating the effect of multipath on low-Earth orbit (LEO) satellite Global Positioning System (GPS) observations. The impact of large-scale changes in tropospheric convection due to the El-Niño Southern Oscillation on the ionosphere is also explored observationally. The influence of nonmigrating tides on the global ionosphere is revealed through study of the longitude variations in the solar quiet current system. Periodic temporal variability in the ionosphere due to planetary waves originating in the lower atmosphere is also investigated. The response of the global ionosphere to the quasi-16 day planetary wave is first presented. This is followed by observational evidence demonstrating that the nonlinear interaction between planetary waves and tides is the primary mechanism responsible for low-latitude ionospheric variability during sudden stratospheric warmings.

Periodic temporal variability in the ionosphere and plasmasphere of solar origin is also studied. During the declining phase of solar cycle 23, near-Earth geospace was routinely disturbed due to high-speed solar wind streams emanating from solar coronal holes. The nature of the coronal holes was such that the Earth's upper atmosphere exhibited periodic behavior due to recurrent geomagnetic activity. A study of the latitude and local time response of the ionosphere to recurrent geomagnetic activity is performed herein. A method for estimating the location of the plasma-

pause from LEO GPS observations is also developed and applied to study periodic oscillations in the plasmopause.

## Acknowledgements

I am forever grateful for the guidance of Drs. Jeffrey Forbes and Kristine Larson. As co-advisors they have provided the necessary direction to my studies over the past several years. At the same time they have encouraged and supported the pursuit of research areas that are of interest to me personally. It has been a truly rewarding experience to work under their supervision during my graduate studies. I also wish to thank the other committee members for their various contributions and useful discussions. The assistance of Astrid Maute, Tzu-Wei Fang and George Millward in the development of and assistance running the coupled TIEGCM-GIP model is also recognized. Discussions with Jiuhou Lei as well as the preparation of TIMED satellite data by Xiaoli Zhang and Jens Oberheide are also greatly appreciated.

I also wish to thank the various providers of data that are used in this thesis. Without making this data freely available to the public much, if not all, of this dissertation would not have been possible.

## Contents

<b>Chapter</b>		
<b>1</b>	<b>Introduction</b>	<b>1</b>
1.1	Ionospheric Variability due to Geomagnetic Storms . . . . .	2
1.2	Ionospheric Variability due to Planetary Waves . . . . .	4
1.3	Ionospheric Variability due to Nonmigrating Tides . . . . .	6
1.3.1	Overview of atmospheric tides . . . . .	6
1.3.2	Connection between nonmigrating tides and the ionosphere . . . . .	7
1.4	Research Objectives . . . . .	9
<b>2</b>	<b>Calculation of topside ionosphere/plasmasphere TEC from the COSMIC</b>	<b>12</b>
2.1	Determination of TEC from GPS observations . . . . .	14
2.2	TEC from COSMIC Precise Orbit Determination Receivers . . . . .	17
2.2.1	COSMIC Satellite Description . . . . .	17
2.2.2	Calculating the Relative TEC: Data Preprocessing and Multipath Mitigation	17
2.2.3	Calculating absolute TEC: COSMIC differential code biases . . . . .	24
2.3	Errors introduced by multipath . . . . .	24
<b>3</b>	<b>Spatial variations in the ionosphere due to nonmigrating tides</b>	<b>26</b>
3.1	Intra-annual variability of the low-latitude ionosphere due to nonmigrating tides . .	27
3.1.1	Introduction . . . . .	27
3.1.2	Data and Analysis . . . . .	27

3.1.3	Results and Discussion . . . . .	29
3.1.4	Conclusions . . . . .	33
3.2	Longitudinal variations in the F-region ionosphere and the topside ionosphere/plasmasphere: observations and model simulations . . . . .	34
3.2.1	Introduction . . . . .	34
3.2.2	COSMIC TEC Observations . . . . .	36
3.2.3	Model Description . . . . .	38
3.2.4	Results . . . . .	42
3.2.5	Discussion . . . . .	48
3.2.6	Conclusions . . . . .	54
3.3	Inter-annual variability in the longitudinal structure of the low-latitude ionosphere due to the El-Niño Southern Oscillation . . . . .	56
3.3.1	Introduction . . . . .	56
3.3.2	Data and Methods . . . . .	57
3.3.3	Results and Discussion . . . . .	60
3.3.4	Conclusions . . . . .	68
3.4	Seasonal and longitudinal variations of the solar quiet ( <i>Sq</i> ) current system during solar minimum determined by CHAMP satellite magnetic field observations . . . . .	69
3.4.1	Introduction . . . . .	69
3.4.2	Data and Methods . . . . .	72
3.4.3	Results and Discussion . . . . .	80
3.4.4	Conclusions . . . . .	94
4	Influence of planetary waves on the low-latitude ionosphere	96
4.1	Modulation of the Equatorial F-Region by the Quasi-16-day Planetary Wave . . . . .	97
4.1.1	Introduction . . . . .	97
4.1.2	Data and Methods . . . . .	98

4.1.3	Results and Discussion . . . . .	99
4.1.4	Conclusions . . . . .	105
4.2	Evidence for Stratosphere Sudden Warming-Ionosphere Coupling due to Vertically Propagating Tides . . . . .	106
4.2.1	Introduction . . . . .	106
4.2.2	Data and Methods . . . . .	108
4.2.3	Results and Discussion . . . . .	109
4.2.4	Conclusions . . . . .	115
<b>5</b>	<b>Periodic variations in the ionosphere and plasmasphere due to recurrent geomagnetic activity</b>	<b>116</b>
5.1	Ionosphere response to recurrent geomagnetic activity: local time dependency . . . .	117
5.1.1	Introduction . . . . .	117
5.1.2	Data and Methods . . . . .	118
5.1.3	Results . . . . .	120
5.1.4	Discussion . . . . .	124
5.1.5	Conclusions . . . . .	129
5.2	Routine determination of the plasmopause based on COSMIC GPS TEC observa- tions of the mid-latitude trough . . . . .	130
5.2.1	Introduction . . . . .	130
5.2.2	Data Processing . . . . .	133
5.2.3	Results and Discussion . . . . .	134
5.2.4	Conclusions . . . . .	140
<b>6</b>	<b>Summary and Conclusions</b>	<b>143</b>
	<b>Bibliography</b>	<b>147</b>

## Tables

### Table

2.1	Comparison of leveling biases calculated with and without data weighting. . . . .	23
3.1	Local time, height and mean $F_{10.7}$ for the time periods considered in the present study. The height range corresponds to the change that occurs between $-30^\circ$ and $+30^\circ$ latitude. . . . .	28
3.2	Geographic locations of the ground based magnetic observatories used in the calculation of the equivalent external $Sq$ current system from 2006-2008. . . . .	79

## Figures

### Figure

- 2.1 (a) One phase connected arc of data for COSMIC-6 on December 21, 2006. The carrier phase TEC was leveled to the pseudorange TEC using equal data weights.  
 (b) Same as (a) except for high-elevation angle data only. . . . . 20
- 2.2 One phase connected arc of data for COSMIC-6 on December 21, 2006. The carrier phase TEC was leveled to the pseudorange TEC using equal data weights. For this arc, multipath causes the large oscillations in the pseudorange TEC at high-elevation angles. . . . . 21
- 2.3 SNR and linear multipath combination for the data arc shown in Figure 2.2. A polynomial fit has been removed from the SNR data. The mean value has also been removed for both the SNR and multipath combination. . . . . 23
- 2.4 The data weights,  $w_i$ , based on Eq. (2.10) for the data arc shown in Figures 2.2 and 2.3. . . . . 23
- 3.1 Month-to-month variability in the equatorial zonal wind nonmigrating tidal amplitudes at 100 km derived from TIMED. Data represents a five-year mean from 2002-2006. The bracketed value indicates the longitudinal structure that is observed when the nonmigrating tide is viewed at a fixed local time. . . . . 31
- 3.2 10-day mean CHAMP in-situ electron densities. Left panel is data that has been binned in latitude and longitude and averaged. The right panel is the CTR wavenumber spectrum. Note that a different color scale is used for each figure. . . . . 32

3.3	Geographic longitude and magnetic latitude variations of the TEC at 17 LT around September equinox for (a) COSMIC observations below 800 km, (b) COSMIC observations above 800 km, (c) GIP-TIEGCM simulation below 800 km without tidal forcing, (d) GIP-TIEGCM simulation above 800 km with tidal forcing, (e) GIP-TIEGCM simulation below 800 km without tidal forcing, and (f) GIP-TIEGCM simulation above 800 km without tidal forcing. . . . .	44
3.4	Same as Figure 3.3 except for December solstice conditions. . . . .	45
3.5	The local time and longitude variation of the TEC around September equinox for (a) COSMIC observations below 800 km, (b) COSMIC observations above 800 km, (c) GIP-TIEGCM simulation below 800 km, and (d) GIP-TIEGCM simulation above 800 km. The results for the TEC below 800 km are averages between 10-20°N magnetic latitude and the TEC above 800 km are averaged between $\pm 10^\circ$ magnetic latitude. The dashed lines in (a) and (c) indicate a phase shift of $90^\circ/24$ hr LT which is the expected phase speed of the <i>DE3</i> in a fixed local time frame. . . . .	49
3.6	Same as Figure 3.5 except for December solstice conditions. . . . .	49
3.7	The seasonal variation of the longitude structures observed by COSMIC below 800 km (a) and above 800 km (b). The TEC is averaged between 12-18 local time and 10-20°N magnetic latitude for the observations below 800 km and $\pm 10^\circ$ for above 800 km. . . . .	50
3.8	Median GPS TEC between 15-16 local time in August 2008 and the location of the ionosonde stations in Maui and Yamagawa (white x's). . . . .	58
3.9	Monthly GPS TEC ratio anomalies (black) and the GPS TEC wave-4 amplitude between 10-20° N magnetic latitude (red). . . . .	61
3.10	Ratio of the monthly median foF2 value between the ionosonde stations in Maui and Yamagawa between local times of 15-16 hrs (solid black) from January 1960 to June 1993. The 81-day smoothed F10.7 cm solar radio flux (red) and the solar cycle fit (dashed black) are also shown. . . . .	63

3.11 (A) Monthly foF2 ratio anomalies (black) and ONI values (red) from January 1960 to June 1993. (B) Yearly extreme value of ONI (red) and the extreme value of foF2 ratio anomalies in the subsequent five months (black). . . . .	64
3.12 (A) Wavelet power spectra of the time series of ONI from January 1960 to June 1993. (B) Wavelet power spectra of the time series of monthly foF2 ratio anomalies. The overlaid contours correspond to the ONI wavelet power spectra. . . . .	66
3.13 <i>Sq</i> current functions during June solstice for (a) CHAMP zonal mean and (b) ground based magnetometers. (c) and (d) are the same as (a) and (b) except for December solstice. . . . .	82
3.14 Seasonal variation of the current function at 12 local time as a function of magnetic latitude for (a) CHAMP zonal mean and (b) ground based magnetometer observations.	84
3.15 <i>Sq</i> current functions derived from CHAMP magnetometer observations for geographic longitudes of $37.5^\circ$ (a, c, e, and g) and $232.5^\circ$ (b, d, f, and h) for the seasons indicated on each panel. . . . .	87
3.16 Longitudinal variation of current function at 12 local time as a function of magnetic latitude for (a) March equinox, (b) June solstice, (c) September equinox, and (d) December solstice. . . . .	88
3.17 Seasonal variation for different longitudinal wavenumber amplitudes in the (a) Northern and (b) Southern Hemispheres. (c) Phases of the longitudinal wavenumbers in the Southern Hemisphere. The phase is defined as the longitude of maximum (or one of multiple maxima when $s > 1$ ) in the range $-60^\circ$ to $300^\circ/s$ , where $s$ is the longitudinal wavenumber. The wavenumbers are based on the average of the current function at 12 local time between $15^\circ$ and $45^\circ$ magnetic latitude in each hemisphere.	92
4.1 (a) $s = 0$ and (b) $s = 1$ SABER temperature average amplitudes with 12-18 day periods at 110 km. . . . .	100

- 4.2 Lomb-Scargle periodograms during the time period of 1 Dec. 2005 - 1 Mar. 2006.  
 (a)  $K_p$  (b) SOHO EUV flux in 0.1-50nm (c) CHAMP in situ electron density for ascending portion of the orbit at the magnetic equator (solid) and  $15^\circ$  magnetic latitude (dashed) (d) same as (c) except for the descending portion of the orbit (e) TEC at 10 LT at the magnetic equator (solid) and  $15^\circ$  magnetic latitude (dashed) (f) same as (e) except for 22 LT . . . . . 102
- 4.3 (a) Zonal-mean CHAMP in situ electron densities for the descending portion of the orbit prior to the removal of a cubic polynomial. (b) Electron density residuals for the descending portion of the orbit expressed as a percentage of the trend. (c) Bandpass-filtered electron density residuals for the descending portion of the orbit expressed as a percentage of the trend. The LT of equatorial crossing is overlaid. (d) Same as (c) except for the ascending portion of the orbit. (e) Bandpass filtered TEC and CTR at 10 LT. Filtered TEC is expressed as a percentage of the cubic polynomial that was removed. (f) Same as (e) except for at 22 LT. . . . . 103
- 4.4 GPS TEC observations during the 2009 SSW for tidal components  $n=0$   $s=0$  (A), the westward propagating nonmigrating semidiurnal tide with zonal wavenumber 1,  $SW1$  (B) and the migrating semidiurnal tide,  $SW2$  (C). The  $K_p$  index is overlaid in A. NCEP reanalysis temperature at  $90^\circ N$  and zonal mean zonal wind at  $60^\circ N$  are overlaid in B and C, respectively. . . . . 110
- 4.5 (A) NCEP planetary wave-1 amplitude of geopotential height at  $60^\circ N$  and 10hPa. The  $SW1$  (westward propagating nonmigrating semidiurnal tide with zonal wavenumber 1) component of GPS TEC at  $15^\circ N$  geomagnetic latitude is also shown and is shifted by 5-days. (B) Same as (A) except for planetary wave-2 and  $S0$  (nonmigrating semidiurnal tide with zonal wavenumber 0). . . . . 112

- 5.1 (A) Lomb-Scargle periodograms of GPS TEC at  $45^\circ$  magnetic latitude and 12 LT (solid) and  $K_p$  (dashed). The horizontal lines indicate the 95% significance level. (B) Raw GPS TEC observations at 12 LT as a function of magnetic latitude and time for days 25-100, 2005. Solid black line is the  $K_p$  index during this time period. (C-D) Same as (A-B) except for at 4 LT. The units of the GPS TEC observations are TECu where  $1 \text{ TECu} = 10^{16} \text{ electrons/m}^2$ . . . . . 121
- 5.2 (A) Lomb-Scargle periodogram of CHAMP in-situ electron density measurements at  $45^\circ$  magnetic latitude for the descending portion of the orbit. The 95% significance level is indicated by the horizontal dashed line. (B) Descending in-situ electron densities as a function of magnetic latitude and time for days 32-100, 2005. The local time of the equatorial crossing is indicated by the solid black line and is nearly constant for the range of latitudes shown. (C) Bandpass filtered electron density residuals. Residuals are expressed as a percentage of the 11-day running mean. Overlaid are the bandpass filtered  $K_p$  values. (D-F) Same as (A-C) except for the ascending portion of the orbit. . . . . 123
- 5.3 Bandpass filtered GPS TEC residuals at different local times for days 25-100, 2005. Results are expressed as a percentage of the 11-day running mean. The bandpass filtered  $K_p$  is overlaid. . . . . 125
- 5.4 Vertical TEC observations for a single COSMIC pass. The estimate of the plasmopause location is indicated by the vertical dashed line. See text for details on determination of the plasmopause location. . . . . 135
- 5.5 COSMIC observations of the plasmopause location during 2008 as a function of the maximum  $K_p$  in the previous 24 hours for all local times. The linear best-fit based on COSMIC observations is shown along with the Moldwin et al. [2002] relationship determined from CRRES observations. Coefficients for both fits are provided in the text. . . . . 137

5.6	COSMIC observations of the plasmapause during 2008 as a function of magnetic local time for different levels of geomagnetic activity. Individual observations are indicated by the grey + symbol. The solid black line indicates the mean and standard deviation within 2 hour local time bins. . . . .	138
5.7	Lomb-Scargle periodograms of the COSMIC plasmapause location during 2008 for the daytime (top) and nighttime (middle) as well as $K_p$ (bottom). The 95% significance level is indicated by the horizontal dashed lines. . . . .	141

## Chapter 1

### Introduction

The existence of an electrically conducting layer in the Earth's atmosphere was first proposed in the 1800s to explain the regular daily variation observed by geomagnetic observatories [Gauss, 1841; Stewart, 1883]. The transmission of radio signals across the Atlantic Ocean in 1901 by Marconi further confirmed the existence of a conducting layer. This additionally demonstrated the importance and influence that this region has on radio wave propagation. Shortly thereafter, it was hypothesized that the conducting layer surrounding the Earth was generated through ionization of neutral particles by solar radiation [Lodge, 1902]. This region subsequently became known as the ionosphere. In the decades following its initial discovery, the ionosphere attracted significant attention in terms of both observations and theory. This resulted in drastic improvements in understanding of the ionosphere, and the theoretical understanding of the ionosphere is now relatively mature as exemplified by the detailed works of Rishbeth and Garriott [1967], Schunk and Nagy [2000], and Kelley [2009].

The above works provide the theoretical underpinnings of the electrical, physical, and chemical processes occurring in the ionosphere. The understanding of the ionosphere from a theoretical perspective is sufficient to capture the salient features, such as latitude, local time, and seasonal variations, that have been observed. This is demonstrated by the number of first-principle physics-based models that can generally reproduce large-scale ionospheric features that are revealed by observations [e.g., STEP Handbook of Ionospheric Models, 1996]. While such models can adequately describe the state of the ionosphere for many instances, observations reveal considerable

variability that is often not fully captured by theoretical models. Developing a comprehensive view of ionospheric variability from an observational perspective is therefore of fundamental importance in order to develop an understanding of what variability may not be adequately described by theoretical numerical models.

The origin of ionospheric variability is often thought of as either coming from above or from below. Forcing from above is related to variability originating at the Sun. The Sun introduces both long and short term variations in the upper atmosphere associated with the approximately 11 year solar cycle and geomagnetic storms, respectively. The ionosphere is also forced from below due to vertically propagating waves that originate in the lower atmosphere. The lower atmosphere introduces both temporal and spatial variability due to planetary waves and nonmigrating tides. Forcing from above and from below are both capable of considerably perturbing the Earth's upper atmosphere, and it is thus vital to develop a comprehensive understanding of their respective influences. In particular, the study of periodic behavior presents the opportunity to investigate a single source of variability, allowing for improved understanding of the system as a whole, and this is the overarching objective of the present thesis. The following sections provide a historical perspective of the understanding of periodic variability in the ionosphere due to geomagnetic activity, planetary waves and tides. This is followed by section 1.4 where the specific questions to be addressed in this dissertation are outlined.

## **1.1 Ionospheric Variability due to Geomagnetic Storms**

The most pronounced form of ionospheric variability is due to interaction of the solar wind with the Earth's magnetosphere. Due to the related disturbances in the Earth's magnetic field, these variations are termed geomagnetic disturbances or, alternatively, geomagnetic storms. Geomagnetic storms significantly impact the entirety of near-Earth geospace, and investigations of their effects on the ionosphere began shortly after the initial discovery of the ionosphere [Appleton and Ingram, 1935; Berkner et al., 1939]. There is thus a long history of studying geomagnetic storms and their influence on the ionosphere [see reviews by Prölss, 1995; Buonsanto, 1999; Mendillo, 2006; Burns

et al., 2008]. Owing to the number of excellent reviews on the ionospheric response to geomagnetic storms, only a brief summary of their effects is discussed herein.

The global ionosphere becomes disturbed during geomagnetic storms due to the large energy deposition that occurs at high-latitudes. Storm time changes in thermospheric neutral composition, temperature, and winds as well as electric fields act together to perturb the ionosphere globally. Significant changes are observed in the ionospheric peak height, electron densities, and total electron content (TEC) [e.g., Prölss, 1995; Buonsanto, 1999; Mendillo, 2006]. Depending on the local time, latitude, and geomagnetic storm phase, both the maximum ionospheric density ( $N_mF_2$ ) and the TEC are seen to increase or decrease relative to their quiet time values. These effects are known as positive and negative storm responses, respectively. In general, negative storm effects tend to occur in the morning while positive storm effects occur in the afternoon and evening. Positive storm effects are also most frequently observed in the winter hemisphere, while negative storm effects are more common in the summer hemisphere. This simplified view of positive and negative storm time effects can be explained largely on the basis of variations in the neutral winds alone [Buonsanto, 1999]. This is, of course, an overly simplified view of positive and negative storm effects, and individual storms can exhibit drastically different behavior.

Historically, geomagnetic storms have been considered to be isolated events that occur in response to a single episode of enhanced solar activity. In particular, geomagnetic storms are typically considered the result of coronal mass ejections (CMEs) or corotating interaction regions (CIRs) associated with solar coronal holes [Tsurutani and Gonzalez, 1997; Zhang et al., 2007]. Geomagnetic activity has, however, been observed to occur on a periodic basis. Periodic geomagnetic activity was first attributed to solar wind sector boundary crossings. This can introduce variations in geomagnetic activity at periods less than the  $\sim 27$  day solar rotation period [Wilcox, 1968; Low et al., 1975]. Mendillo and Schatten [1983] demonstrated that, although the response is smaller, similar changes are observed in the ionosphere during solar wind sector boundary crossings as observed during large geomagnetic storms. More recently, during the declining phase of solar cycle 23, periodic oscillations in thermospheric neutral density, composition, and global ionospheric

TEC were observed [Crowley et al., 2008; Lei et al., 2008a,b; Thayer et al., 2008]. The periodic behavior of the upper atmosphere was connected to recurrent geomagnetic activity associated with rotating solar coronal holes and the corresponding high-speed solar wind streams. The extension of geomagnetic storms from isolated events to recurrent features is highly advantageous as it permits isolation of the ionospheric response to a single forcing mechanism. Study of the impact of recurrent geomagnetic activity on the ionosphere therefore represents an opportunity to considerably improve understanding of the ionospheric response to geomagnetic storms. Further, the recurrent nature of this phenomena indicates a sense of predictability to variability in the ionosphere, representing a step forward in the ability to predict space weather.

## 1.2 Ionospheric Variability due to Planetary Waves

Traveling planetary waves are global scale oscillations with periodicities ranging from about two to 20 days. The dominant planetary wave periodicities correspond to normal modes in the atmosphere and are centered around 2, 5, 10, and 16 days [Forbes, 1995]. It should be noted that planetary waves can also be stationary; however, throughout the following, planetary wave refers to traveling planetary waves. The presence of periodicities in the atmosphere due to planetary wave activity was first noted in the troposphere and stratosphere. Detailed discussion of observations and theory of planetary waves in the troposphere and stratosphere can be found in the reviews by Madden [1979] and Salby [1984]. Subsequent observations of winds in the mesosphere and lower thermosphere (MLT) (80-150 km) revealed the presence of planetary wave oscillations at these altitudes as well [e.g., Manson et al., 1981; Vincent, 1990; Forbes et al., 1995a]. These studies illustrated the large amplitude that planetary waves can achieve in the MLT. The similarity of the oscillations in the MLT to those in the troposphere and stratosphere indicate that planetary waves propagate vertically. That is, the planetary waves in the MLT are originally of tropospheric origin (as opposed to being generated in-situ). The vertical propagation of planetary waves and the connection between planetary waves in the troposphere and MLT is supported by several numerical modeling studies [e.g., Salby, 1981a,b; Pogoreltsev et al., 2007].

In addition to modulating winds and temperatures in the MLT, planetary wave oscillations have been observed in the ionosphere. Perhaps the first indication of the effect of planetary waves on the ionosphere was in the day-to-day changes of the geomagnetic daily variation [Chapman and Bartels, 1940; Hasegawa, 1960]. At the time, these authors did not connect the day-to-day variations directly to planetary wave activity, but did acknowledge that they were likely to be connected to day-to-day variations in the neutral winds. It was not until the aforementioned observational and modeling studies revealed the large amplitude of planetary waves in the MLT that the importance of the lower atmosphere on introducing ionospheric variability was fully recognized. A number of observational studies have since revealed the existence of periodic behavior due to planetary waves in various ionospheric measurements such as the equatorial electrojet, F-layer peak height (HmF2) and density (NmF2) [Chen, 1992; Forbes and Leveroni, 1992; Yi and Chen, 1993; Altadill and Apostolov, 2003; Altadill et al., 2003; Pancheva et al., 2006; Vineeth et al., 2007]. These studies have, however, been fairly limited in scope owing to the absence of sufficient global observations. The present understanding of the influence of planetary waves on the ionosphere is therefore somewhat limited due to the lack of a global context.

Although a number of observational and modeling studies have demonstrated that planetary waves can introduce considerable temporal variability in the ionosphere, the mechanism by which planetary waves influence the ionosphere remains partly unknown. Pogoreltsev et al. [2007] studied the vertical propagation of planetary waves and found that they do not propagate above  $\sim 100$ - $110$  km. Thus, planetary waves are not able to directly influence the F-region ionosphere and an indirect mechanism is needed. The present understanding is that planetary waves can influence E-region winds and in-turn modulate the low-latitude electric fields that are generated by the dynamo mechanism [e.g., Forbes, 1996; Pogoreltsev et al., 2007]. This generates oscillations at F-region altitudes, since the low-latitude electric fields control the strength and formation of the equatorial ionization anomaly (EIA). It is also important to note that even though planetary waves may be restricted in altitude or latitude, they are capable of modulating MLT winds, dynamo-generated electric fields, and the ionospheric F-region globally. The global influence of planetary

waves was established in the modeling study by Liu et al. [2010]. Liu et al. [2010] demonstrated that both migrating and nonmigrating tides (atmospheric tides are discussed in detail in section 1.3) are perturbed globally even in the case of a planetary wave restricted to high-latitudes. The changes in the low-latitude tides result in perturbations to the low-latitude ionosphere. It should be noted that there is also significant observational evidence for tidal perturbations during periods of planetary wave activity [e.g., Forbes et al., 1995b; Angelats i Coll and Forbes, 2002; Pancheva et al., 2009].

### **1.3 Ionospheric Variability due to Nonmigrating Tides**

#### **1.3.1 Overview of atmospheric tides**

Prior to discussion of ionospheric variability due to nonmigrating tides, it is useful to provide a brief overview of atmospheric tides and their sources. Atmospheric tides are global scale oscillations in the atmosphere that are driven primarily by the periodic absorption of solar radiation. Solar thermal tides are dominated by diurnal and semidiurnal oscillations, having periods of 24 and 12 hours, respectively. Tidal oscillations can further be classified as either migrating or nonmigrating. A migrating tide travels westward with the apparent motion of the Sun and, in a fixed local time frame, is longitudinally invariant. Conversely, nonmigrating tides exhibit longitudinal variability when viewed from a fixed local time perspective. Nonmigrating tides are characterized by their longitudinal wavenumber and propagation direction (eastward or westward).

Zonal symmetry of the periodic solar radiation leads to the generation of migrating tides, and this explains their longitude invariance. However, since nonmigrating tides exhibit longitudinal differences, they must be generated by a longitudinal dependent source. The tropical troposphere plays a key role in generation of nonmigrating tides through large-scale latent heat release in convective regions. Owing to land-sea differences in the tropics, latent heating is not zonally symmetric, and this leads to the generation of nonmigrating tides [Hagan and Forbes, 2002, 2003]. Although nonmigrating tides originate in the troposphere, they propagate vertically and achieve

large amplitudes in the MLT, where they eventually dissipate. Nonmigrating tides can also be generated through the nonlinear interaction between planetary waves and tides [Teitelbaum and Vial, 1991; Angelats i Coll and Forbes, 2002]. Due to the fact that nonmigrating tides produced by the nonlinear interaction of planetary waves and tides can further interact with the original planetary wave this mechanism can lead to generation of a large spectrum of nonmigrating tides [Palo et al., 1999].

Throughout the remainder of the text different nonmigrating tides will be discussed along with the longitudinal wavenumber they may impose on the ionosphere when viewed from a fixed local time perspective. It is therefore useful to provide an overview of the tidal nomenclature used herein. A solar thermal tide can be characterized by its frequency,  $n\Omega$ , where  $\Omega = \frac{2\pi}{24} \text{ h}^{-1}$  and  $n = 1, 2, 3$  (i.e., diurnal, semidiurnal, terdiurnal) and zonal wavenumber  $s$  [ $s < 0$  ( $s > 0$ ) corresponding to eastward (westward) propagation]. Throughout the following, the convention of *DWs* or *DEs* to denote a westward- or eastward-propagating diurnal tide, respectively, with zonal wavenumber  $s$  will be used. For semidiurnal and terdiurnal oscillations let *S* and *T* replace *D*. The corresponding zonally-symmetric oscillations are denoted *D0*, *S0*, *T0*, and stationary planetary waves (*SPW*) with zonal wavenumber  $s$  are expressed as *SPWs*. Last, note that from a fixed local time perspective, a tide appears as a longitude variation with zonal wavenumber  $k_s = |s - n|$ . So, for example, it is simple to see that *DE3* ( $n = 1, s = -3$ ) and its various manifestations (e.g., electric fields, composition variations) produce wave-4 ( $k_s = 4$ ) structures in a local time frame. However, it is also apparent that *SE2* ( $n = 2, s = -2$ ), *DW5* ( $n = 1, s = 5$ ), *SW6* ( $n = 2, s = 6$ ), *SPW4* ( $n = 0, s = 4$ ), and so on, also appear as  $k_s = 4$ . By the same token, a number of other combinations of  $n$  and  $s$  can produce  $k_s = 1, 2$  and  $3$  signatures.

### 1.3.2 Connection between nonmigrating tides and the ionosphere

A direct connection between nonmigrating tides and spatial variability in the ionosphere was first proposed by Sagawa et al. [2005] to explain longitudinal variability observed at a fixed local time in nighttime 135.6-nm emissions. Sagawa et al. [2005] proposed that nonmigrating tides

in the MLT introduce longitudinal perturbations to the E-region dynamo, which in-turn drives longitudinal variability in the EIA. It is worth noting that this mechanism is similar to that outlined in section 1.2 for planetary waves; however, nonmigrating tides introduce a spatial variability. As a historical note, the existence of longitudinal variability in the ionosphere was originally observed by Thuillier et al. [1976]. However, it was several decades until observations and models revealed the large amplitude of nonmigrating tides in the MLT [e.g., Lieberman, 1991; Talaat and Lieberman, 1999; Forbes et al., 1995b; Hagan and Forbes, 2002, 2003] allowing for the connection between the lower and upper atmosphere as proposed by Sagawa et al. [2005].

Following the work of Sagawa et al. [2005], a large body of observational and modeling work arose on the topic of longitudinal variability in the upper atmosphere. Longitudinal variability has been observed in ionospheric TEC and electron densities [Lin et al., 2007; Liu and Watanabe, 2008; Scherliess et al., 2008; Wan et al., 2008], the equatorial electrojet [Alken and Maus, 2007; England et al., 2006; Lühr et al., 2008],  $\mathbf{E} \times \mathbf{B}$  drift velocities [Kil et al., 2008; Fejer et al., 2008; Hartman and Heelis, 2007], and thermospheric winds, O/N<sub>2</sub> ratio, nitric oxide density, and exospheric temperature [Forbes et al., 2009; Häusler et al., 2010; He et al., 2010; Oberheide and Forbes, 2008a]. While these studies clearly demonstrate the presence of longitudinal variability in the Earth's upper atmosphere, they do not fully reveal the source mechanism. A number of modeling studies have, however, confirmed the hypothesis of ? that nonmigrating tides originating in the troposphere are largely responsible for the generation of longitude variability in the ionosphere and thermosphere [England et al., 2010; Hagan et al., 2007; Jin et al., 2008; Ren et al., 2010]. When observed at a fixed local time, throughout most of the year, the ionosphere and thermosphere exhibit a wave-4 variation in longitude, and these modeling studies have supported the suggestion of Immel et al. [2006] that this variation is due to the eastward propagating nonmigrating diurnal tide with zonal wavenumber-3 (*DE3*). This connection is further supported by observational studies demonstrating the similar seasonal variation observed in the *DE3* and ionospheric wavenumber-4 (or wave-4) longitude structure [Kil et al., 2008; Pancheva and Mukhtarov, 2010; Wan et al., 2008].

Based on the aforementioned studies, it is now well accepted that nonmigrating tides of

tropospheric origin significantly influence the ionosphere and thermosphere. These studies have largely focused on the *DE3* and its generation of a wave-4 longitudinal structure in the upper atmosphere. However, it is important to note that there are other nonmigrating tides in the MLT that can also significantly influence the low-latitude ionosphere and thermosphere. This is particularly relevant during November-February when the amplitude of the *DE3* is small and other nonmigrating tides may be of greater importance [e.g., Forbes et al., 2008]. Additionally, the wave-4 structure that is observed in the ionosphere can be generated by other vertically propagating waves, such as the stationary planetary wave-4 (*SPW4*), or the semidiurnal eastward propagating tide with zonal wavenumber-2 (*SE2*) [Hagan et al., 2009; Oberheide et al., 2011].

#### 1.4 Research Objectives

While the sources of ionospheric variability discussed in the preceding sections may, at first, appear unconnected, they may be combined under the general designation of periodic behavior in the ionosphere. Periodic behavior can be viewed as either temporal, as in the case of recurrent geomagnetic activity and planetary waves, or spatial, as in the case of nonmigrating tides. It is the overarching objective of this dissertation to further understand the influence of the aforementioned mechanisms on introducing periodicities in the ionosphere. This is first pursued with regard to the coupling between the lower atmosphere and ionosphere. As previously mentioned, the connection between the lower atmosphere and ionospheric variations is a relatively recent discovery, and it is therefore a rapidly developing field with many unanswered questions. This fact combined with the recent deep solar minimum and advances in observational methods have made the past years ripe for detailed investigation of the coupling between the lower and upper atmosphere. A combination of observations and numerical models are used to develop an understanding of how vertically propagating waves of lower atmospheric origin introduce both periodic spatial and temporal variability in the ionosphere. This dissertation specifically aims to address the following scientific questions:

- (1) How does the seasonal variation of nonmigrating tides influence longitude variations at

different altitudes in the ionosphere?

- (2) Does interannual variability in the lower atmosphere introduce similar variations in the longitude structures in the ionosphere?
- (3) How is the global  $Sq$  current system influenced by nonmigrating tides?
- (4) What is the global response of ionospheric densities to planetary wave activity?
- (5) Is there observational evidence for the nonlinear interaction between planetary waves and tides in the ionosphere?

All of the above questions address periodic variations in the ionosphere related to forcing from the lower atmosphere. During the declining phase of solar cycle 23, the Earth's upper atmosphere also exhibited periodic variations of solar origin [e.g., Gibson et al., 2009]. The final portion of this dissertation addresses this fascinating solar-terrestrial connection. While the existence of periodic behavior in the upper atmosphere related to periodic solar activity is not itself a new discovery, there remain some unexplored aspects of this connection, and these are investigated herein. The following scientific questions are addressed:

- (6) What is the local time and latitude dependence of the ionospheric response to periodic geomagnetic activity and what drives these differences?
- (7) Can Global Positioning System (GPS) receivers onboard low-Earth orbit satellites be used to study plasmopause variability? Furthermore, can such a technique be applied for studying periodic behavior of the plasmopause?

The subsequent four chapters are dedicated to answering the scientific questions that are posed above and are organized as follows. Chapter two provides details concerning the development of a new data set of TEC observations from the Constellation Observing System for Meteorology, Ionosphere, and Climate (COSMIC) satellites. This data set will be used to help answer some of the aforementioned scientific questions. Chapter three is devoted to the influence of nonmigrating

tides on the ionosphere, and addresses the above items (1)-(3). The influence of planetary waves on ionospheric densities is addressed in chapter four. The ionospheric response to periodic geomagnetic activity is studied in chapter five. The final chapter summarizes the work presented herein, and outlines some of the remaining questions concerning periodic behavior in the Earth's upper atmosphere.

## Chapter 2

### Calculation of topside ionosphere/plasmasphere TEC from the COSMIC

The GPS transmits signals on two different frequencies. Owing to the dispersive nature of the ionosphere, it introduces a signal delay that is frequency dependent. Because of this frequency dependence, it is possible for precise positioning users with observations on both frequencies to correct for the ionospheric effect. Alternatively, observations on both frequencies can be used as a measurement tool for ionospheric science. The advent and proliferation of the GPS in the past few decades has provided a new tool for observational studies of the ionosphere. The high-temporal and spatial (over certain regions) resolution makes GPS a unique observational method. Because of this, the GPS has contributed significantly to ionospheric science [Coster and Komjathy, 2008, and references therein]. For example, the connection between storm enhanced density to plasmaspheric erosion by Foster et al. [2002] was made possible by the extensive network of GPS receivers in North America, and would have been difficult to make with other methods of observation.

While the GPS has contributed significantly to ionospheric science, it is not without its limitations. The primary limitation of GPS is that it is a path integrated measurement of electron density, and thus only measures the line-of-sight TEC. For ground-based receivers, this means that the GPS provides the TEC integrated from the surface of the Earth to  $\sim 20200$  km. The lack of information on the vertical structure of the ionosphere in GPS TEC observations can be overcome using tomographic inversion [e.g., Yin et al., 2004; Yizengaw et al., 2007]; however, the vertical resolution is relatively coarse. Occulting signals between GPS satellites and a GPS receiver onboard a low-Earth orbit (LEO) satellite can be used to obtain high resolution electron density

observations. This technique is known as GPS radio occultation, and has been employed by a number of satellite missions such as GPS/MET, CHAMP, GRACE, SAC-C, and, most recently the Constellation Observing System for Meteorology, Ionosphere and Climate (COSMIC). These missions have demonstrated the utility of GPS radio occultation for studying both the neutral atmosphere and the ionosphere [Anthes et al., 2008; Anthes, 2011]

GPS radio occultation and ground-based GPS TEC measurements are also limited in that they primarily provide information about the E- and F-regions of the ionosphere. GPS radio occultation provides vertical profiles of electron densities in the altitude range of  $\sim 60$ -800 km. Electron densities in the F-region contribute approximately two-thirds to ground-based TEC observations [Klobuchar, 1996; Mendillo, 2006]. Variations in the ground-based TEC are thus reflective of changes that are occurring at predominately F-region altitudes. More recently, precise orbit determination (POD) GPS receivers onboard LEO satellites have been used to study processes taking place above the F-region peak [Mannucci et al., 2005, 2008; Yizengaw et al., 2006; Pedatella et al., 2009]. The use of GPS TEC observations from LEO satellites has two primary advantages. First, it permits separation of the TEC into distinct altitude regions which allows separate study of the structure and dynamics of the F-region ionosphere and the topside ionosphere and plasmasphere. Additionally, LEO satellites provide more complete global coverage compared to ground-based observations.

Although there have been a number of studies utilizing GPS TEC observations from LEO satellites, these have been relatively limited in scope in that they have focused on single events. However, the large number of LEO satellites with GPS POD receivers that are now in orbit (largely due to the launch of the COSMIC satellites in 2006, see Section 2.2.1), provides a wealth of data that can be employed for a variety of scientific purposes. Rather than studying single events, portions of this dissertation seek to use GPS TEC observations from LEO satellites to gain insight into the topside ionosphere/plasmasphere in a more general sense. Observations from the COSMIC satellites are utilized in portions of subsequent chapters, and the present chapter provides details on the data processing necessary to obtain the topside ionosphere/plasmasphere TEC from the COSMIC. The

remainder of the chapter is organized as follows. Section 2.1 gives a general overview of using the GPS to determine the TEC. Specific details on the methodology that is applied to the COSMIC GPS observations is provided in Section 2.2. A brief discussion of the errors present and precision of the COSMIC TEC observations is given in Section 2.3.

## 2.1 Determination of TEC from GPS observations

Methods for determining the TEC from dual frequency GPS observations are well established, and have proven to be a useful tool for studying the ionosphere [Klobuchar, 1996; Mannucci et al., 1998, 1999]. The TEC can be derived from dual frequency observations of the pseudorange or carrier phase. On the two frequencies,  $f_1 = 1575.42MHz$  and  $f_2 = 1227.6MHz$ , the observables are given by

$$P1 = \rho_{nondispersive} + \frac{40.3TEC_{rel}}{f_1^2} + \epsilon_{\rho 1} \quad (2.1)$$

$$P2 = \rho_{nondispersive} + \frac{40.3TEC_{rel}}{f_2^2} + \epsilon_{\rho 2} \quad (2.2)$$

$$L1 = \rho_{nondispersive} - \frac{40.3TEC_{rel}}{f_1^2} + \lambda_1 n_1 + \epsilon_{\phi 1} \quad (2.3)$$

$$L2 = \rho_{nondispersive} - \frac{40.3TEC_{rel}}{f_2^2} + \lambda_2 n_2 + \epsilon_{\phi 2} \quad (2.4)$$

where,  $P1$  and  $P2$  are the pseudorange observations on  $f_1$  and  $f_2$ , respectively, and  $L1$  and  $L2$  are the corresponding carrier phase measurements converted to units of distance.  $\lambda_1$  and  $\lambda_2$  are the wavelengths of  $f_1$  and  $f_2$ , respectively.  $n_1$  and  $n_2$  are the corresponding carrier phase cycle ambiguities.  $\rho_{nondispersive}$  represents terms that are frequency independent such as geometric range (i.e., distance between the satellite transmitter and receiver), satellite and receiver clock biases, troposphere delay (for ground-based receivers), and relativity effects. Several important differences exist between the pseudorange (Eqs. (2.1) and (2.2)) and carrier phase (Eqs. (2.3) and (2.4)) observations. First, the carrier phase observations are biased by an unknown cycle ambiguity,  $\lambda n$ . Second, the pseudorange error term,  $\epsilon_{\rho}$ , is roughly two orders of magnitude larger than  $\epsilon_{\phi}$ , the

carrier phase error. Errors result from both measurement noise, and any unmodeled effects, such as multipath. Owing to the dispersive nature of the ionosphere, the ionospheric term is frequency dependent. The line-of-sight TEC can thus be determined from dual-frequency GPS observations.

A relative value of the line-of-sight TEC can be found by combining Eqs. (2.1) and (2.2):

$$P2 - P1 = \frac{40.3TEC_{rel}}{f_2^2} - \frac{40.3TEC_{rel}}{f_1^2} + \epsilon_{\rho}12 = TEC_{rel} \frac{40.3(f_1^2 - f_2^2)}{f_1^2 f_2^2} + \epsilon_{\rho}12 \quad (2.5)$$

$$TEC_{rel} = \frac{f_1^2 f_2^2}{40.3(f_1^2 - f_2^2)} (P2 - P1) + \epsilon_{\rho}12 \quad (2.6)$$

The carrier phase observations in Eqs. (2.3) and (2.4) can similarly be combined yielding

$$TEC_{rel} = \frac{f_1^2 f_2^2}{40.3(f_1^2 - f_2^2)} (L1 - L2) + b + \epsilon_{\phi}12 \quad (2.7)$$

where,  $b$  is an unknown bias that arises from the carrier phase cycle ambiguities. Eqs (2.6) and (2.7) provide two different approaches for determining the relative line-of-sight TEC, each offering advantages and disadvantages. The primary advantage of determining the line-of-sight TEC from Eq. (2.6) is that an absolute value of TEC can be determined based on pseudorange observations. However, pseudorange observations are more susceptible to multipath effects and measurement noise which can degrade the precision of pseudorange-based TEC observations. Note also that by subtracting  $P1$  from  $P2$  the error is increased. That is,  $\epsilon_{\rho}12$  is greater than  $\epsilon_{\rho}1$  and  $\epsilon_{\rho}2$ . Because of their shorter wavelength, carrier phase observations are considerably less impacted by multipath and measurement noise and, thus, Eq. (2.7), provides a more precise measurement of TEC compared to Eq. (2.6). The drawback of carrier phase observations is that the resulting TEC is ambiguous. It is, however, possible to combine the absolute nature of pseudorange observations with the low-noise carrier phase observations to determine the TEC with both high accuracy and precision. As described by Mannucci et al. [1998], for each phase-connected arc,  $j$ , the carrier phase bias,  $b_j$ , can be estimated as follows

$$b_j = \frac{\sum_{i=1}^{n_j} w_i [(P2 - P1)_i - (L1 - L2)_i]}{\sum_{i=1}^{n_j} w_i} \quad (2.8)$$

Eq. (2.8) represents a weighted mean between the pseudorange and carrier phase TEC observations with the data weights given by  $w_i$ . The bias for each phase-connected arc,  $b_j$ , is typically referred to as the leveling bias since Eq. (2.8) "levels" the ambiguous carrier phase observations to the absolute pseudorange observations. The data weights are typically chosen to reduce the effect of measurement noise on the calculation of the carrier phase bias. For ground-based receivers, a weighting function is typically selected that down weights lower-elevation angle data where pseudorange multipath tends to be the largest [e.g., Mannucci et al., 1998]. The selection of an appropriate weighting function for GPS receivers onboard LEO satellites, such as the COSMIC, is more complicated, and will be discussed in greater detail in Section 2.2.2.

It is important to note that the line-of-sight TEC value calculated using either Eq. (2.6) or (2.7) is a relative value, and two additional parameters must also be estimated. The absolute TEC is found after accounting for receiver and transmitter differential code biases (DCB). The absolute total electron content is then given by

$$TEC_{absolute} = TEC_{rel} + DCB_{receiver} + DCB_{satellite} \quad (2.9)$$

where  $DCB_{receiver}$  is the DCB of the receiver and  $DCB_{satellite}$  is the DCB of the transmitting GPS satellite. The DCBs result from instrumental (i.e. hardware) biases that are frequency dependent and are therefore different for each receiver and transmitter. The DCBs can also change over time and it is necessary to estimate them on a regular basis [Coco et al., 1991].

## 2.2 TEC from COSMIC Precise Orbit Determination Receivers

### 2.2.1 COSMIC Satellite Description

COSMIC consists of six micro-satellites and was launched in April 2006 to study the Earth's neutral atmosphere and ionosphere through the technique of GPS radio occultation. The satellites were initially launched into an orbit near 500 km altitude and over the following 17 months gradually moved into the final orbit configuration. In the final orbit, the six satellites are evenly distributed in longitude at an altitude of  $\sim 800$  km and an orbital inclination of  $72^\circ$  [Anthes et al., 2008]. The constellation nature of the COSMIC makes it well-suited for studying the ionosphere and plasmasphere due to the good local time and longitude coverage that it affords. To study both the neutral atmosphere and ionosphere, each satellite is equipped with multiple payloads, including two GPS antennae for GPS radio occultation (GOX), two GPS antennae for POD, a tiny ionospheric photometer, and a triband beacon [Rocken et al., 2000; Cheng et al., 2006]. Two GOX and POD antennas are necessary so that one pair can track GPS satellites rising above the limb of the Earth while the other pair tracks setting GPS satellites. Data from the GOX antennae are used to generate atmospheric and ionospheric profiles in support of the primary mission objective. The POD data are primarily used to meet the stringent orbit determination requirements of  $\sim 10$  cm in position and less than 1 mm/s in velocity that are necessary to achieve the desired accuracy of the atmospheric profiles [Kursinski et al., 1997].

### 2.2.2 Calculating the Relative TEC: Data Preprocessing and Multipath Mitigation

The methods outlined in Section 2.1 have been applied to the raw GPS POD observations from the COSMIC to determine the line-of-sight TEC. As a first step in the process, the raw GPS observations are preprocessed using the Jet Propulsion Laboratory GPS Inferred Positioning System (GIPSY) software to determine the phase-connected arcs, and identify and attempt to correct any cycle slips [Lichten and Border, 1987]. Phase connected arcs for the same satellite-receiver pair that are separated by less than one minute are then connected to form data arcs that are as long as

possible. This is accomplished by adjusting the  $L1$  values in the second arc of data by an integer number of wavelengths so that the beginning of the second phase connected arc is in agreement with the end of the first phase connected arc. Connecting adjacent data arcs is advantageous due to the relatively short nature of data arcs encountered on LEO satellites. By extending the data arc it is possible to obtain a more accurate estimate of the leveling bias.

Errors that may be present in ground-based GPS TEC observations are magnified in LEO GPS TEC observations due to the considerably smaller absolute levels of TEC above the altitude of LEO satellites. For example, a 1 TECu ( $1 \text{ TECu} = 10^{16} \text{ el/m}^2$ ) error in ground-based TEC observations may represent a few percent error, while a similar error may be greater than 10% for LEO observations. It is therefore of utmost importance to identify and mitigate potentially large sources of error when computing the TEC from LEO observations. Among the potentially large sources of error is the effect of multipath. This is of particular concern for the COSMIC observations which are susceptible to significant pseudorange multipath. Multipath effects in the COSMIC observations are thought to arise due to the GPS signal reflecting off of the solar panels, and also the use of patch GPS antennae that do not suppress multipath as well as other antennae. Additionally, the COSMIC solar panels are highly dynamic, and this may serve to increase the severity of the multipath effects. To illustrate both the intrinsic data noise as well as the effect of multipath, pseudorange and carrier phase relative TEC are shown for two data arcs in Figures 2.1 and 2.2. The different noise and error characteristics of pseudorange and carrier phase measurements of TEC are clearly evident in both figures. The high-frequency small-scale variations that are seen in Figures 2.1 and 2.2 in the pseudorange observations are due to intrinsic data noise and are related to the ability of the receiver to cross-correlate the incoming GPS signal with the receiver-generated copy. These variations are dominated by a random component that will likely average out over time when the leveling bias is computed. However, the large systematic oscillations present at high elevation angles in Figure 2.2 are cause for concern. The periodic nature of these oscillations is indicative of specular multipath which is thought to arise from reflections of the GPS signal off of the solar panels. These oscillations are  $\sim 40 \text{ TECu}$  peak-to-peak which is significant given the

absolute levels of TEC at high-elevation angles is on the order of 10 TECu. Note that the carrier phase observations are also effected by multipath; however, the effect of multipath on the GPS carrier phase observations is orders of magnitude less than the effect on the pseudorange and is thus not apparent in Figures 2.1 and 2.2.

Given the magnitude of the multipath effect, as demonstrated by Figure 2.2, and the relatively small values of absolute TEC, it is necessary to mitigate the effects of multipath to accurately estimate the leveling bias. An accurate estimate of the leveling bias is necessary so that the COSMIC GPS TEC observations are suitable for scientific studies. There are several methods which can be employed in order to minimize the effect of the pseudorange multipath. The first possible approach is to remove the multipath effects through appropriately modeling the multipath effect on the GPS signal. For example, ray-tracing algorithms can be used to model the GPS signal and any signal reflections to determine the multipath error. This approach has been used in the past for the GEOSAT Follow-On Satellite and TOPEX/Poseidon [e.g., Irish et al., 1998; Byun et al., 2002]. Unfortunately, the highly dynamic nature of the COSMIC satellite solar panels complicate using this approach for minimizing multipath present in the COSMIC observations. An alternative approach is to use the POD antenna signal-to-noise ratio (SNR) values to remove the pseudorange multipath. Oscillations that are present in pseudorange measurements due to multipath occur in phase with oscillations in the SNR [Ray and Cannon, 2001]. If the SNR data are scaled appropriately it can therefore be used to remove the pseudorange oscillations that occur due to multipath. While using the SNR data for multipath mitigation is theoretically possible, this method is found to be unsuitable for application to the COSMIC data. This can be observed in Figure 2.3 which shows the SNR data corresponding to Figure 2.2. The values of *MP1* and *MP2* are also overlaid and these are reflective of the pseudorange multipath. It is clear that changes in the SNR are not fully reflective of the multipath in the pseudorange data. In particular, while there are clearly oscillations in each, the phasing does not match. It is therefore clear that it is not feasible to use the SNR for multipath mitigation. The reasons for that lack of similarity in oscillations in the SNR and pseudorange are unknown but may be due to poor quality of the SNR

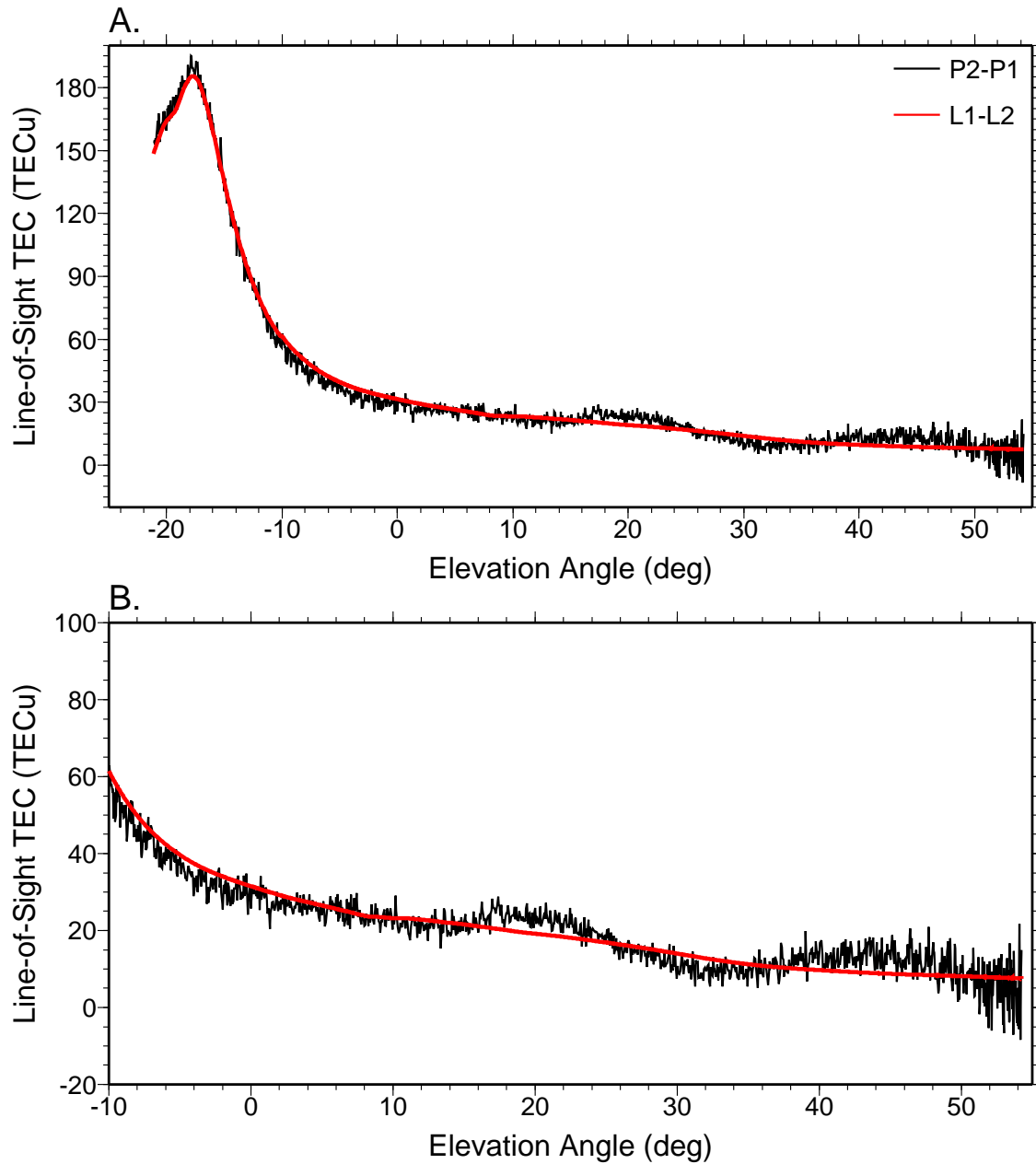


Figure 2.1: (a) One phase connected arc of data for COSMIC-6 on December 21, 2006. The carrier phase TEC was leveled to the pseudorange TEC using equal data weights. (b) Same as (a) except for high-elevation angle data only.

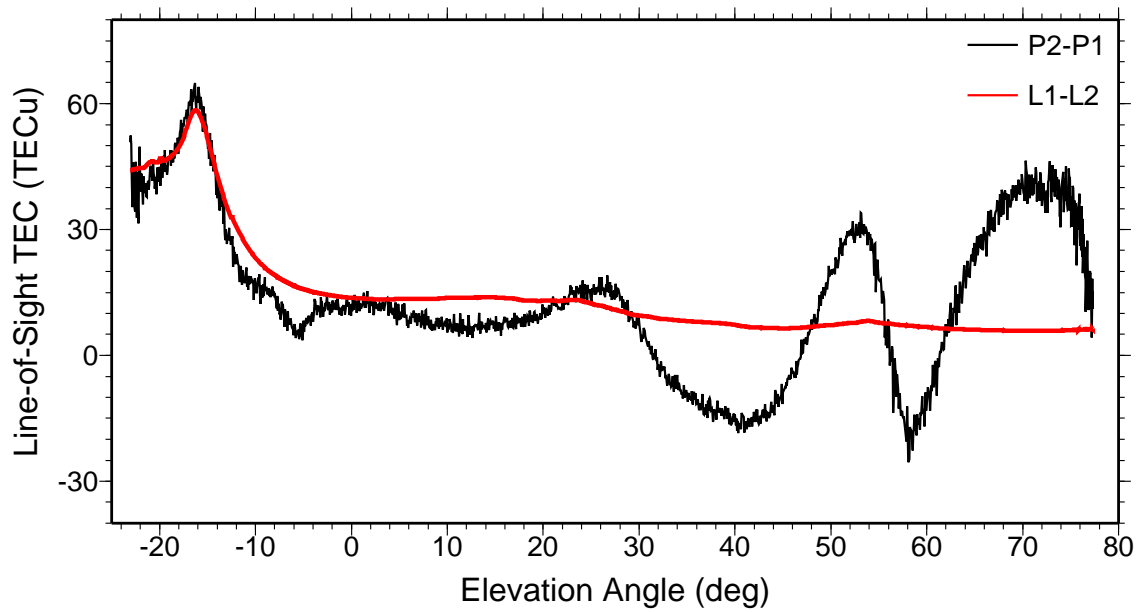


Figure 2.2: One phase connected arc of data for COSMIC-6 on December 21, 2006. The carrier phase TEC was leveled to the pseudorange TEC using equal data weights. For this arc, multipath causes the large oscillations in the pseudorange TEC at high-elevation angles.

data.

An alternative approach for mitigating the impact of pseudorange multipath on the leveling bias is through an appropriate selection of the data weights,  $w_i$ , in Eq. (2.8). As previously mentioned, for ground-based GPS observations this is typically done by downweighting low elevation angle data which is more susceptible to multipath. Due to the configuration of the COSMIC satellites as well as the dynamic nature of the solar panels, such a simplistic scheme would not be very effective. For the present study, a data weighting scheme is implemented where the data weight is based on the multipath observed for each individual data arc. The data weight for the  $i^{th}$  epoch is calculated based on Eq. (2.10).

$$w_i^{-1} = \left| [(P2 - P1)_i - (L1 - L2)_i] - \frac{1}{n_j} \sum_{k=1}^{n_j} [(P2 - P1)_k - (L1 - L2)_k] \right| + 1 \quad (2.10)$$

As an example, the data weights calculated from Eq. (2.10) for the data arc shown in Figures 2.2 and 2.3 are shown in Figure 2.4. Figure 2.4 demonstrates that using the multipath weighting scheme results in significantly less weight given to the high-elevation data where multipath is present. This should, in principle, minimize the influence of pseudorange multipath when the leveling bias is calculated. A brief comparison of the influence of this data weighting scheme on the leveling bias is given in Table 2.1. Table 2.1 gives the leveling bias estimates for the case of no weighting or assigning the weight based on Eq. (2.10) for the data arcs shown in Figures 2.1 and 2.2. When no significant multipath is present, the difference between the two methods is minimal and is  $\sim 0.02$  TECu. However, when significant multipath is present, the leveling bias estimates differ by almost 2 TECu. This represents roughly 20% of the absolute level of TEC at high-elevation angles. Given these differences, it is clear that data weighting significantly influences the leveling bias and, in-turn, the carrier phase observation of TEC. Further detail on how implementation of this data weighting scheme improves the results will be presented in Section 2.3.

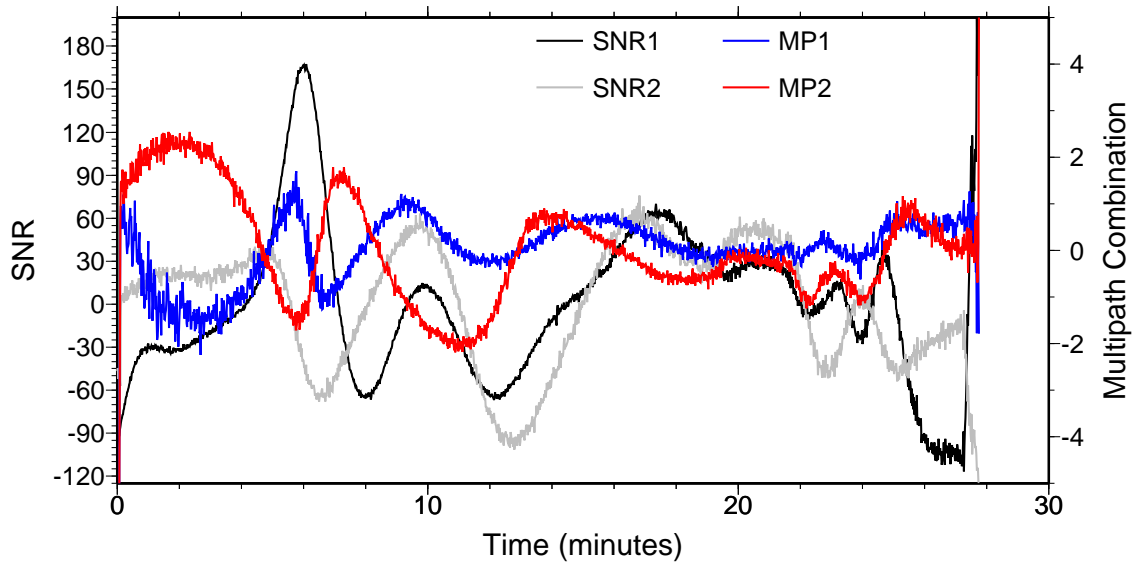


Figure 2.3: SNR and linear multipath combination for the data arc shown in Figure 2.2. A polynomial fit has been removed from the SNR data. The mean value has also been removed for both the SNR and multipath combination.

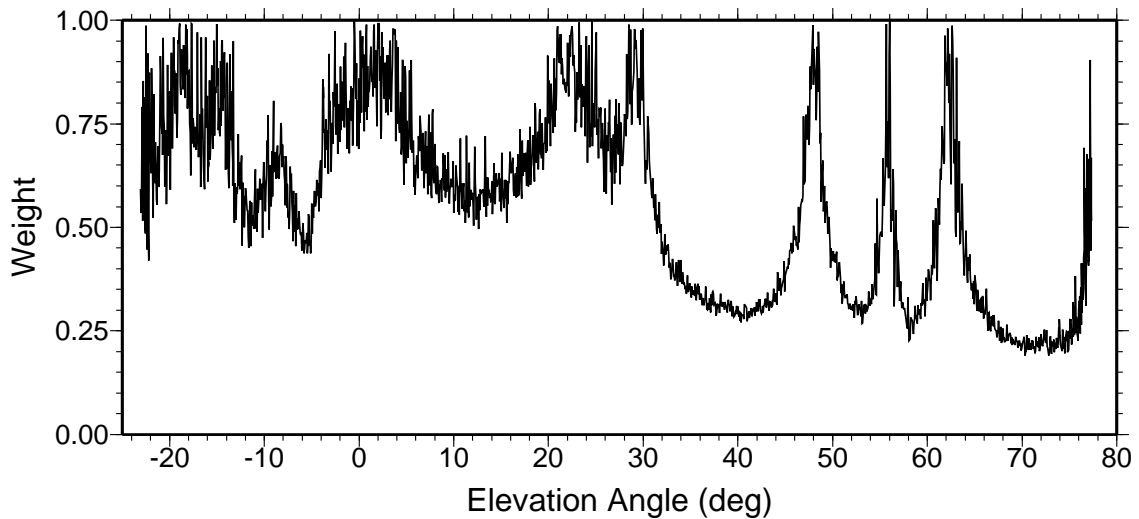


Figure 2.4: The data weights,  $w_i$ , based on Eq. (2.10) for the data arc shown in Figures 2.2 and 2.3.

Table 2.1: Comparison of leveling biases calculated with and without data weighting.

Case	Bias - Equal Weight (TECu)	Bias - Multipath Weight (TECu)
No Multipath (Figure 2.1)	197.389	197.368
Multipath (Figure 2.2)	26.051	24.648

### 2.2.3 Calculating absolute TEC: COSMIC differential code biases

The methods outlined in the preceding section provide the relative TEC and it is necessary to account for the COSMIC and GPS-transmitter DCBs to obtain the absolute TEC. GPS satellite biases are routinely estimated by the Center for Orbit Determination in Europe (CODE) [Hugentobler et al., 2004] and are used in the present study. The COSMIC DCBs also need to be estimated. This is done using a model-assisted method using only high-latitude, nighttime observations [Heise et al., 2002]. In this method, the Global Core Plasma Model [Gallagher et al., 2000] is used to determine a minimum value of vertical TEC (VTEC), and the DCB is estimated so that the high-latitude, nighttime observations exceed this minimum value. Note that the VTEC is calculated from the line-of-sight TEC using a geometric mapping function [e.g., Klobuchar, 1996]. To account for temporal changes, the COSMIC DCBs are first estimated daily and then smoothed using a 10-day running window. Following estimation of the COSMIC DCBs, the absolute line-of-sight TEC is calculated based on Eq. (2.9). Note that for the scientific studies that utilize the COSMIC TEC observations, only observations above  $65^\circ$  elevation angle are used. This is done in order to minimize the impact of potential errors due to mapping function and/or spatial gradients.

## 2.3 Errors introduced by multipath

Owing to the significant level of multipath present in the COSMIC POD observations, it is important to assess the errors that this introduces into the topside ionosphere/plasmasphere TEC determined from the COSMIC data. In doing so it is also possible to develop an understanding of how effectively the multipath mitigation technique is able to reduce these effects. Although it is not possible to determine the absolute accuracy of the individual VTEC observations, an estimate of the precision can be obtained by comparing simultaneous observations using different GPS satellites. If no errors are present and there are no spatial gradients, simultaneous observations of VTEC should be identical. On the basis of one month of observations, the average absolute difference between simultaneous observations is found to be 1.89 TECu when the observations are weighted as detailed

earlier. This compares to a difference of 2.42 TECu without implementing a weighting scheme to reduce the multipath effect. Note that any error introduced by spatial gradients is common to both of these, and the reduction can therefore be attributed to reducing the influence of multipath on estimating the leveling bias. The remaining error can be attributed to spatial gradients, mapping function error, and residual multipath effects. Clearly the weighting method is an effective means for mitigating the effect of multipath on estimating the absolute TEC. Minimizing this effect is desired to obtain a high-quality set of observations suitable for application to scientific studies.

## Chapter 3

### Spatial variations in the ionosphere due to nonmigrating tides

As discussed in section 1.3 a number of prior studies have clearly demonstrated the influence of nonmigrating tides of tropospheric origin on the low-latitude ionosphere. Nonetheless, many facets of this connection remain unexplored, and it is the aim of the present chapter to further investigate this fascinating connection. This begins by first developing an understanding of the seasonal changes to the observed longitude structures in the F-region ionosphere and how these are connected to different nonmigrating tides in section 3.1. This is further developed in section 3.2, where the seasonal and altitudinal dependence of the longitude variations are investigated using a combination of COSMIC observations and a numerical model. The influence of inter-annual variations in the nonmigrating tides that may result from the El-Niño Southern Oscillation on introducing ionospheric variability is presented in section 3.3. Lastly, the impact of nonmigrating tides on the solar quiet ( $Sq$ ) current system is demonstrated which indicates that the influence of nonmigrating tides are not restricted to low-latitudes but, rather, perturb the global ionosphere. Each of the following sections are organized as follows. First, a brief introduction is provided to provide both historical context as well as outline the objectives of each section. This is followed by an overview of the data analysis procedures. Results are then presented along with discussion. Each section is concluded with a summary of the results along with discussion of any potentially unanswered questions.

### **3.1 Intra-annual variability of the low-latitude ionosphere due to nonmigrating tides**

#### **3.1.1 Introduction**

Recent studies have shown that similar variability is observed in the wave-4 structure of the low-latitude ionosphere and the *DE3* tide [Immel et al., 2009; Liu and Watanabe, 2008; Scherliess et al., 2008; Wan et al., 2008]. Using SABER temperature data, Forbes et al. [2008] demonstrated that while *DE3* dominates the nonmigrating tidal spectrum during most months, other waves (e.g., *DE2*, *DW2*, *SW4*, *TW5*) also make important contributions and moreover some waves dominate over *DE3* during certain months. Similar conclusions are expected for dynamo-region winds, and Oberheide and Forbes [2008b] recently validated a method that uses tidal temperature and wind measurements to derive a full specification of tidal winds in the dynamo region. These studies raise the question of whether similar month-to-month variability exists in the longitude structure of the dynamo region and the low-latitude F-region ionosphere. The time periods when *DE3* is no longer the dominant tidal component are of particular interest as it is presently unclear how this impacts the longitudinal structure of the EIA. The primary aim of this section is to further explore the month-to-month variability of the longitudinal structure of the EIA with particular emphasis on time periods when *DE3* is not the dominant tidal component. F-region electron densities from the Planar Langmuir Probe (PLP) onboard the Challenging Minisatellite Payload (CHAMP) satellite and equatorial zonal winds derived from the SABER and TIDI instruments onboard the TIMED satellite are used to further explore the connection between E-region winds and the longitudinal structure of the EIA.

#### **3.1.2 Data and Analysis**

##### **3.1.2.1 CHAMP In-situ Electron Densities**

The CHAMP satellite is in a nearly Sun-synchronous orbit and it precesses in local time at the rate of  $\sim 5.44$  minutes per day. In-situ electron densities can be derived from the PLP onboard

Table 3.1: Local time, height and mean  $F10.7$  for the time periods considered in the present study. The height range corresponds to the change that occurs between  $-30^\circ$  and  $+30^\circ$  latitude.

Time Period	Local Time	Height (km)	Mean $F10.7(W/m^2/Hz)$
17-27 January 2003	15.2-14.2	409-419	127.8
11-21 July 2004	13.5-12.6	379-389	140.2
1-11 December 2004	12.4-11.5	369-380	92.8
13-23 December 2005	13.7-12.8	348-359	84.9

the CHAMP satellite [Rother et al., 2004] and are available from the Information Systems and Data Center operated by Geo Forschungs Zentrum (GFZ) Potsdam (<http://isdc.gfz-potsdam.de>).

We use CHAMP electron density data during the four time periods given in Table 3.1. Also given in Table 3.1 is the altitude of the CHAMP satellite between  $-30^\circ$  and  $+30^\circ$  latitude, the observed local time, and the mean  $F10.7$  flux. These time periods were selected because geomagnetic activity was low and CHAMP sampled mid-day local times when longitudinal structures are expected to be present.  $DE3$  is weakest during December-January and we have thus mainly focused on this time period. One time period in July is included in order to demonstrate that a wave-4 longitudinal structure is observed when  $DE3$  is the dominant nonmigrating tide. Due to the changing local time of the CHAMP satellite, only one time period in January was suitable. Two time periods in December were suitable and both have been included to provide additional confirmation of the results obtained during this time period. Representative global ionospheric maps are created for each time period by binning the data in 10 degrees longitude and 1 degree latitude. As shown in Table 3.1 the sampling altitude differs for each of the time intervals analyzed which will impact the observed electron densities. It is also uncertain where any given measurement falls with respect to the F-region peak density. However, all of the measurements fall within the 300-450 km height range that Lin et al. [2007] found to have a significant wave-4 structure indicating that the in-situ measurements are a suitable means for observing longitudinal structures in the F-region.

At each longitude, we characterize the strength of the EIA with the crest-to-trough ratio (CTR) (Eq. 3.1) [Lühr et al., 2007; Mendillo et al., 2000].

$$CTR = \frac{n_{e,n} + n_{e,s}}{2n_{e,t}} \quad (3.1)$$

where  $n_{e,n}$  and  $n_{e,s}$  are the electron densities of the north and south peaks and  $n_{e,t}$  is the electron density of the equatorial trough. The electron density profile at each longitude can then be characterized by a single number. Note that the CTR is set to 1 when the EIA has not been well established at satellite altitudes. Alternatively, the latitude separation of the EIA peaks may be used to characterize the strength of the EIA. We have obtained similar results using both approaches, and have chosen to use the CTR for the present analysis.

### 3.1.2.2 Zonal Wind Amplitudes from TIMED

The nonmigrating tidal amplitudes of the equatorial zonal wind at 100 km are determined using a Hough Mode Extension (HME) analysis of temperature and zonal and meridional wind measurements from the SABER and TIDI instruments onboard the TIMED satellite [Oberheide and Forbes, 2008b]. An altitude of 100 km is used due to superior data quality at this altitude. Since the nonmigrating tides are vertically propagating, observations at 100 km can be viewed as representative of the nonmigrating tides entering the dynamo region. A five-year mean (2002-2006) is used in order to determine the month-to-month variability in the leading nonmigrating tidal components. The equatorial zonal wind results are representative of the broader latitude region between  $\pm 30^\circ$  latitude.

### 3.1.3 Results and Discussion

The month-to-month variation of the equatorial zonal winds at 100 km for the leading nonmigrating tidal components is shown in Figure 3.1. The leading tidal components are *DE2*, *DE3*, and *SW4* which when viewed at a fixed local time appear as wave-3, wave-4, and wave-2, respectively. The amplitude of each nonmigrating tide exhibits significant month-to-month variability. In particular, it should be noted that during January the leading tidal component is *SW4* followed by *DE2* and *DE3*. During March-November *DE3* is greatest followed by *DE2* and *SW4*. In

December *DE2* is the primary component followed by *SW4* and *DE3*. Given the premise that the E-region tides are expected to induce a longitudinal dependence in the dynamo electric fields, one may expect to observe a similar variability in the longitudinal structure of the EIA. Therefore, the dominant longitudinal structure of the EIA is expected to be wave-2 in January, wave-4 in July, and wave-3 in December. Other tidal components, many of which appear as wave-2, -3, and -4, are also present and we have focused here on the three leading tidal components. A detailed discussion of the various nonmigrating tides that appear as wave-2, -3, and -4 and the relative strengths of each is given in Forbes et al. [2008].

Representative global electron density maps for the four time periods considered are displayed in the left panel of Figure 3.2. A Fourier fit is performed using the CTR values at each longitude and the resulting wavenumber spectra are shown in the right panel. Similar to the variations seen in the zonal wind amplitudes, the primary component of the CTR amplitude exhibits intra-annual variability. In January 2003, the dominant component is wave-2 followed by wave-3 and wave-4 is the weakest component. The primary component changes to wave-4 in July 2004 and a similar amplitude is seen for waves 1-3 during this time period. In December 2004 and 2005 the dominant wavenumber is 3 followed by wave-2, -1 and -4. There are also significant changes in the amplitudes from December 2004 to December 2005 which is thought to be due to changes in the orbital altitude of the CHAMP satellite and/or changes in the level of solar activity (see Table 3.1).

Although the primary focus is on *SW4*, *DE2*, and *DE3* and their corresponding signatures in the ionosphere, a significant wave-1 component is also present. The offset of the geomagnetic field with respect to the geographic equator and longitudinal variation in the neutral winds create hemispheric asymmetries in the longitudinal structure of the ionosphere [McDonald et al., 2008]. The resulting hemispheric asymmetries will impact the CTR value and may be partly responsible for the observed wave-1 component. A wave-1 component can also result from the nonmigrating tides *D0*, *DW2*, *SW1*, and *SW3*. These tides arise from nonlinear interaction of *SPW1* with *DW1* and *SPW1* with *SW2* [Angelats i Coll and Forbes, 2002; Hagan and Roble, 2001]. The months in question overlap with *SPW1* activity in the respective winter hemispheres indicating that the

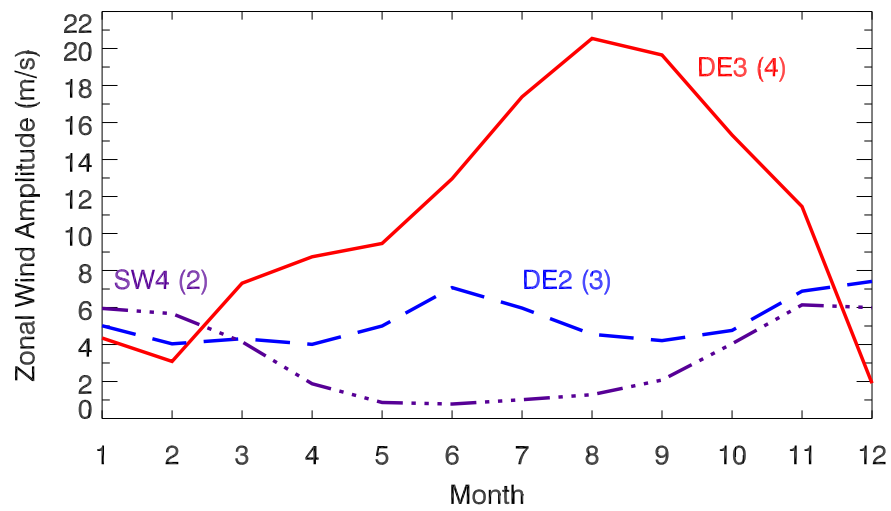


Figure 3.1: Month-to-month variability in the equatorial zonal wind nonmigrating tidal amplitudes at 100 km derived from TIMED. Data represents a five-year mean from 2002-2006. The bracketed value indicates the longitudinal structure that is observed when the nonmigrating tide is viewed at a fixed local time.

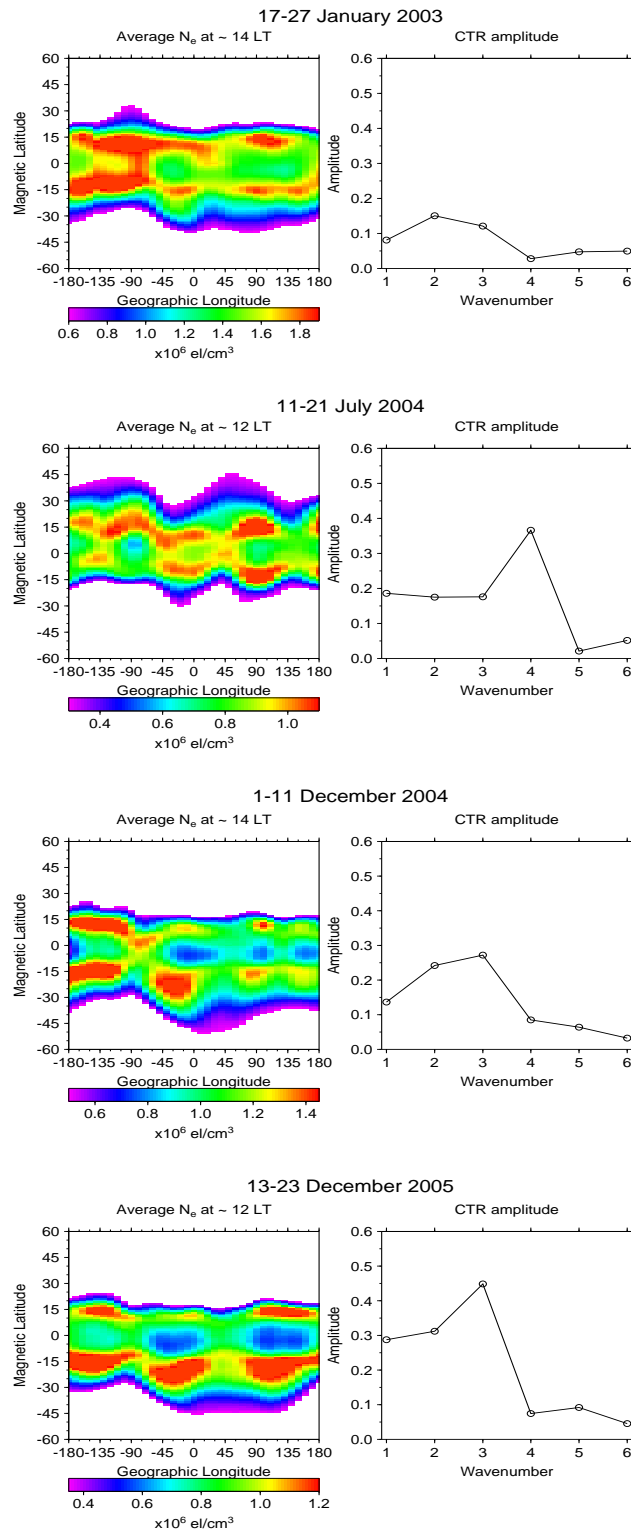


Figure 3.2: 10-day mean CHAMP in-situ electron densities. Left panel is data that has been binned in latitude and longitude and averaged. The right panel is the CTR wavenumber spectrum. Note that a different color scale is used for each figure.

observed wave-1 may partly be due to these nonmigrating tides.

We now turn our attention to discuss the results shown in Figure 3.2 in the context of Figure 3.1. Assuming that *SW4*, *DE2*, and *DE3* are comparable in terms of their efficiency in generating electric fields, we may expect similar seasonal variations in the CTR wavenumber spectrum and the zonal wind wavenumber spectrum at 100 km. This is a reasonable assumption considering the vertical structure of these tides presented by Forbes et al. [2008] indicates similar efficiency of electric field generation for these nonmigrating tides. In January the leading component in the zonal wind amplitude is *SW4* (wave-2) which is also the dominant wavenumber of the CTR. This demonstrates that *SW4* may be capable of modulating the dynamo electric fields in order to create a wave-2 longitudinal structure in the EIA during January. During this same time period, the second leading component is observed to be wave-3 in both the zonal wind amplitude as well as the CTR. A wave-4 (*DE3*) structure dominates the zonal wind amplitude in July and this is also the dominant wavenumber of the CTR. In July 2004 the CTR amplitude for wave-2 and wave-3 are equivalent whereas from Figure 3.1 it is expected that wave-3 be greater than wave-2. The results shown in Figure 3.1 represent a five year mean and this discrepancy may be the result of year-to-year variability in the zonal wind. Lastly, a wave-3 structure is observed to be the primary component of both the zonal wind amplitude and the CTR during December. In both December 2004 and December 2005, wave-2 is the second major component of the CTR which is in agreement with the zonal wind amplitudes. Similar to *SW4* in January, this demonstrates that *DE2* is likely able to influence the dynamo electric fields in order to create a wave-3 structure in the EIA during December.

#### 3.1.4 Conclusions

Recent studies that have explored coupling between the dynamo region and the F-region ionosphere have emphasized the similar variability that is observed in the wave-4 structure and *DE3* [Immel et al., 2009; Liu and Watanabe, 2008; Wan et al., 2008]. Through the inclusion of additional longitudinal structures and tidal components, the present section provides additional

insight into this coupling process. During January and December, *DE3* is no longer the dominant tidal component in the equatorial zonal winds and the dominant longitudinal structure of the EIA becomes wave-2 and wave-3, respectively. The change in the primary longitudinal structure of the EIA from wave-4 to wave-2 and wave-3 is thought to be due to the dominant nonmigrating tide no longer being *DE3*, but, being *SW4* in January and *DE2* in December. This demonstrates that, in addition to *DE3*, other nonmigrating tides are likely able to modulate the dynamo electric fields and subsequently influence the longitudinal structures in the F-region ionosphere. The four time periods used in the present analysis have provided observational evidence of longitudinal structures of the EIA other than wave-4 that develop when *DE3* is no longer the primary nonmigrating tide in the dynamo region. It is believed that this is a recurrent feature in January and December due the dominant nonmigrating tides being *SW4* and *DE2*, respectively.

## **3.2 Longitudinal variations in the F-region ionosphere and the topside ionosphere/plasmasphere: observations and model simulations**

### **3.2.1 Introduction**

Since nonmigrating tides considerably influence the strength and formation of the EIA, the ionospheric signature of nonmigrating tides is most pronounced in the low-latitude F-region [e.g., Lin et al., 2007]. However, observations and modeling results have demonstrated the presence of longitude variations in the topside ionosphere [Hartman and Heelis, 2007; Kil et al., 2008; Fang et al., 2009; Huang et al., 2010]. These studies have revealed the occurrence of longitude variations up to 840 km altitude. Furthermore, the longitudinal variations appear to evolve with altitude which may be related to the relative importance and differences in neutral winds, composition, and  $\mathbf{E} \times \mathbf{B}$  drift in different altitude regimes. While the modulation of the EIA strength by nonmigrating tides adequately explains the presence of longitudinal variations in the F-region, this mechanism alone may not fully explain the occurrence and structure of longitudinal variations in the topside ionosphere. In regions of large magnetic field declination, significant seasonal differences in the ion

density and  $\mathbf{E} \times \mathbf{B}$  drift velocity near 840 km based on measurements from the Defense Meteorological Satellites Program (DMSP) satellites are observed [Hartman and Heelis, 2007; Huang et al., 2010]. Both Hartman and Heelis [2007] and Huang et al. [2010] consider the geomagnetic field declination to play a fundamental role in generating longitude variations in the topside ionosphere. Huang et al. [2010] proposed that the neutral winds in combination with the magnetic field declination will enhance (reduce) the field-aligned wind resulting in regions of larger (smaller) ion density in the topside ionosphere. The seasonal variation in the winds will introduce a seasonal variation to the longitude variation in the topside ionosphere. In addition to the geomagnetic field orientation, longitudinal variations in the topside ionosphere may be connected to vertically propagating nonmigrating tides of tropospheric origin. This is supported by recent observations demonstrating the direct penetration of nonmigrating tides into the thermosphere [Forbes et al., 2009; Talaat and Lieberman, 2010]. Forbes et al. [2009] demonstrated tidal variations in exospheric temperature and this has the potential to introduce longitudinal variations in the topside ionosphere through influencing the topside ionosphere scale height.

While past studies have demonstrated the presence of longitude variations in the topside ionosphere, the mechanisms responsible for their formation and how they compare to similar features in the F-region remains unclear. The present study aims to further understand the longitude variations in the topside ionosphere and plasmasphere electron densities through both observations and numerical simulations. We utilize observations from the COSMIC satellites to obtain simultaneous observations of the TEC above and below 800 km altitude. This allows us to study the similarities and differences between longitude structures in the F-region and topside ionosphere/plasmasphere along with their local time and seasonal dependencies. We further present numerical model results which demonstrate the relative importance of nonmigrating tides and the geomagnetic field on generating longitude variations in the topside ionosphere.

### 3.2.2 COSMIC TEC Observations

In the present study we use COSMIC ionospheric observations of TEC from both the POD antennae and also from vertical electron density profiles obtained through the method of radio occultation. The TEC from the POD antennae provide information on electron densities above 800 km while the TEC from radio occultation provides details on the electron density up to 800 km. This method thus permits separation of the ionospheric densities into two distinct altitude regions. Further details on each of these observations are provided in the subsequent sections.

#### 3.2.2.1 Observations of TEC between 800 and 20200 km

The quasi-zenith directed POD antennae onboard the COSMIC satellites provides information on the TEC between the COSMIC orbital altitude ( $\sim 800$  km) and the GPS orbital altitude ( $\sim 20200$  km). The TEC in this region is representative of the electron densities in the topside ionosphere and plasmasphere. Based on these observations alone it is not possible to distinguish between these two regions and we thus refer to these observations as the topside ionosphere/plasmasphere TEC throughout the remainder of the text. The TEC is obtained based on the methods outlined in Chapter 2. For the present study, all of the quiet time ( $K_p < 3$ ) vertical TEC observations from the POD antennae during 2008 are binned in magnetic latitude, geographic longitude, local time and day of year. The bin sizes are  $2.5^\circ$  in magnetic latitude,  $24^\circ$  in geographic longitude and two hours in local time. Note that in the analysis we mix magnetic and geographic coordinates since the longitude variations in the ionosphere are typically considered in a geographic coordinate frame. Magnetic latitude is used since the TEC is generally symmetric about the magnetic equator. The binning is performed using a running 45-day window of observations centered on each day of the year. The observations are fairly evenly distributed throughout the data bins and each bin has  $\sim 400$ -500 data points. Although the COSMIC provides adequate sampling on shorter time scales, a 45-day window of observations is used to reduce the effect of data noise, which may arise due to multipath, while still providing an adequate characterization of the seasonal variations.

### 3.2.2.2 Observations of TEC below 800 km

In order to study the longitude variations at predominately F-region altitudes, COSMIC observations of vertical electron density profiles obtained through the technique of GPS radio occultation are used. The COSMIC electron density profiles extend up to  $\sim 800$  km altitude and are in general agreement with incoherent scatter radar and ionosonde observations [Lei et al., 2007; Kelley et al., 2009]. For the present study, we use electron density profiles during quiet time periods ( $K_p < 3$ ) of 2008 obtained through the COSMIC Data Analysis and Archive Center (CDAAC) (<http://cosmic-io.cosmic.ucar.edu/cdaac/>). For all profiles that extend upwards of 750 km, the measured electron densities are used to calculate the integrated TEC between the bottom and top of the profile. Only profiles with a maximum altitude of greater than 750 km are used so that all of the computed TEC values encompass roughly the same altitude domain. Although we integrate up to  $\sim 800$  km, the TEC in this altitude region will largely be dominated by electron densities in the F-region and thus these observations are suitable for studying variations primarily occurring at F-region altitudes. The COSMIC electron density profiles are not strictly vertical profiles and the computed TEC for each electron density profile is geographically located at the latitude and longitude of the tangent point corresponding to the maximum electron density. To facilitate comparison with the results for altitudes above the COSMIC satellite altitude, the TEC from the COSMIC electron density profiles are binned using the same method as discussed in section 3.2.2.1 for binning of the topside ionosphere/plasmasphere TEC. We do note, however, that there are considerably fewer data points for the COSMIC TEC below 800 km and each bin contains  $\sim 15$ -25 points. This difference is primarily driven by the different temporal sampling of GPS radio occultation compared the TEC observations from the POD antenna. While the POD data are nearly continuous, GPS radio occultation data are only available when the geometry between the COSMIC and a GPS satellite is suitable and thus there are significantly fewer GPS radio occultation observations.

### 3.2.3 Model Description

To investigate the source of the longitude variations in the F-region ionosphere and the topside ionosphere and plasmasphere we have coupled the Global Ionosphere Plasmasphere (GIP) model [Millward et al., 2007] to the National Center for Atmospheric Research (NCAR) Thermosphere Ionosphere Electrodynamics General Circulation Model (TIE-GCM) [Richmond et al., 1992]. A brief description of the individual models is provided below along with details regarding the coupling of the two models.

The GIP model is based on the ionosphere-plasmasphere part of the Coupled Thermosphere Ionosphere Plasmasphere (CTIP) model [Millward et al., 2001] and solves the coupled equations of continuity, momentum and energy balance in a magnetic coordinate system. Densities, temperatures and velocities are calculated for  $O^+$  and  $H^+$  ions and the additional ions ( $N^+$ ,  $N_2^+$ ,  $O_2^+$ ,  $NO^+$ ) are calculated based on chemical equilibrium. In the GIP model, the equations are solved along realistic geomagnetic field lines based on the magnetic apex coordinate system [Richmond, 1995b] and the International Geomagnetic Reference Field (IGRF). This represents a significant improvement upon the dipole geomagnetic field utilized in the CTIP model since the GIP includes distortions of the geomagnetic field which can have a significant influence on the ionosphere. The GIP model is separated into a low-mid latitude region where interhemispheric transport along flux tubes is taken into account and a high-latitude portion where there is no plasma flux across an upper boundary of 10000 km. For the present study we are only concerned with the low-mid latitude region which extends to  $L=4$ , where  $L$  is the L-shell [McIlwain, 1961]. The flux tubes in the low-mid latitude region are spaced  $4.5^\circ$  in magnetic longitude and each magnetic meridian includes 67 flux tubes in latitude (or altitude). The base of each magnetic flux tube is 90 km and they extend to  $\sim 19000$  km. Lastly, we note that the GIP only solves for the ions and electrons in the ionosphere and plasmasphere and does not include calculation of the thermosphere or electrodynamics. It thus requires input of the neutral thermosphere and  $\mathbf{E} \times \mathbf{B}$  drift velocities from an external source, such as an empirical model.

The TIE-GCM globally solves the dynamical equations for the thermosphere and ionosphere with self-consistent electrodynamics. The electrodynamics are calculated using a realistic geomagnetic field (IGRF) and magnetic apex coordinate system [Richmond, 1995b]. At each time step the model calculates the neutral temperature, winds, and densities of various atmospheric constituents as well as the ionospheric structure on fixed pressure levels. The resultant neutral winds, ion densities, and calculated conductivities are then used to solve for the electric potential at each time step. For the present study, the TIE-GCM is run with a horizontal resolution of  $2.5^\circ$  in geographic latitude and longitude and a vertical resolution of four points per scale height. The lower boundary of the model is at approximately 97 km and the upper boundary ranges from 400-700 km depending on solar flux conditions.

In an effort to improve upon the shortcomings in each model, we have coupled the GIP model to the TIE-GCM. Hereafter we will refer to the coupled model as GIP-TIEGCM. There are two significant advantages resulting from this coupling. First, the neutral thermosphere and electrodynamics that need to be specified for the GIP can be solved directly in a self-consistent manner and thus do not need to be based on empirical thermosphere or electrodynamic models. The coupling of these two models also eliminates the artificial upper boundary of the TIE-GCM. It is thus no longer necessary to specify ion number and electron heat fluxes between the ionosphere and plasmasphere across the model upper boundary. This should, in principal, improve the description of the low-latitude ionosphere and electrodynamics. Rather than including an interface between the two models at the upper boundary of the TIE-GCM, the models are completely coupled and the ionosphere in the TIE-GCM is entirely replaced by the GIP ionosphere. The TIE-GCM electrodynamics solver is used and the necessary field line integrals of conductivity and wind-driven current density are calculated along the GIP flux tubes. The electric fields calculated within the TIE-GCM are then used to calculate the vertical and zonal  $\mathbf{E} \times \mathbf{B}$  drift velocities used for the ionospheric calculations. In the GIP model we have included zonal  $\mathbf{E} \times \mathbf{B}$  drifts which represents an improvement upon the original CTIP model which only includes drift in the magnetic meridional plane. The inclusion of zonal drifts in the model is important for the present study since

they may contribute to longitudinal variations in the topside ionosphere [e.g., Huang et al., 2010]. The TIE-GCM also provides the neutral thermosphere densities, temperature, and winds that are required for the GIP calculations. Because it is not included in the TIE-GCM, the neutral hydrogen in the coupled model is still specified empirically based on the Mass Spectrometer Incoherent Scatter (MSIS) model [Picone et al., 2002]. Since the height domains of the GIP and TIE-GCM models are different, it is necessary to make some assumptions regarding the neutral thermosphere so that it encompasses the entire GIP grid. Above and below the TIE-GCM domain we assume constant winds and neutral temperatures. The individual constituents of the neutral atmosphere are extrapolated assuming a constant scale height where the scale height is determined at each latitude and longitude gridpoint from either the highest or lowest two gridpoints in the vertical direction. Note that the coupled GIP-TIEGCM is still in a developmental stage; however, for the purposes of the present study, it has been adequately tested to confirm that the model provides reasonable results.

The GIP-TIEGCM has been used to perform several simulations in an effort to reproduce and understand the causes of observed longitude variations in both the F-region as well as the topside ionosphere and plasmasphere. Simulations have been performed for September equinox and December solstice under solar quiet ( $F_{10.7}=60$ ) conditions. Note that this solar flux is slightly below the actual conditions during 2008. However, it was necessary to run the model at a slightly lower solar flux so that the F-region electron densities from the model match observations during 2008. Each simulation is initialized from a 20 day run of TIE-GCM (version 1.92). The coupled model is then run for 10 days so that the model reaches a steady state. Two simulations are performed for each season: one where the lower boundary of the model is forced with diurnal and semidiurnal migrating and nonmigrating tides and another with no tidal forcing at the lower boundary. This allows us to separate the effects of longitude variations due to nonmigrating tides and those that may be related to the orientation of the geomagnetic field. For the September simulation, the lower boundary forcing is based on the Global Scale Wave Model (GSWM) [Hagan and Forbes, 2002, 2003]. In September, as previously discussed and shown in the following section,

the daytime ionosphere exhibits a distinct wave-4 pattern and prior studies have connected this longitude variation to the *DE3* tide [e.g., Immel et al., 2006; Wan et al., 2008]. We have adjusted the *DE3* amplitude and phase at the lower boundary during September in order to achieve good agreement between the observations and model results for the TEC up to 800 km. It was necessary to increase the *DE3* amplitude by a factor of 1.5 and adjust the phase by 2.75 hours. As the present study is primarily concerned with the difference in longitude variations of TEC above and below 800 km we have chosen to adjust the model forcing so that the model results above 800 km should be representative of the actual conditions. Adjusting the model forcing in this manner permits a more accurate comparison with observations of the topside ionosphere/plasmasphere TEC. For December solstice, the GSWM tends to overestimate the *DE3* and this results in a significant wave-4 longitude structure in the ionosphere which is inconsistent with observations of wave-2 or wave-3 structures during this time period [e.g., Scherliess et al., 2008; Pedatella et al., 2008]. For the December solstice simulation, we have therefore chosen to use lower boundary conditions based on Hough Mode Extensions (HMEs) obtained from Thermosphere Ionosphere Mesosphere Energetics and Dynamics (TIMED) TIMED Doppler Interferometer (TIDI) and Sounding of the Atmosphere using Broadband Emission Radiometry (SABER) observations [Forbes et al., 2009; Oberheide et al., 2009, 2011]. The HMEs used are based on observations from 2002-2008 and thus are considered to be representative of the tidal climatology at  $\sim 97$  km. Using the HMEs for the December simulation is thought to provide more realistic lower boundary forcing compared to using the GSWM for this time period. A mixture of nonmigrating tides is likely to create the longitude variations that are observed in December and this complicates any adjustment of the lower boundary forcing to match the observations as was done for the September simulations. We therefore do not make any effort to adjust the lower boundary forcing for the December simulation. Note that we could have also used the HMEs to force the lower boundary for the September simulation. However the *DE3* forcing, which primarily generates the longitude variability during September, would remain the same since we adjust the September *DE3* to achieve agreement between TEC below 800 km in the model and observations. We would, therefore, expect to obtain similar results in September if we used the

HMEs to force the lower boundary.

For comparison with the observations, the model results are used to calculate the TEC in the topside ionosphere/plasmasphere up to 20200 km. Since the model domain extends only to  $\sim 19000$  km at the magnetic equator, and less at higher latitudes, we extrapolate the electron densities up to 20200 km. The extrapolation is done by first transforming the electron densities along the flux tubes to a latitude, longitude, and altitude grid. The grid spacing is  $3^\circ$  in magnetic latitude,  $4^\circ$  in geographic longitude, and in the vertical ranges from 5 km at low altitudes to 500 km at high altitudes. The electron density at each gridpoint is calculated based on a distance weighted average of the electron densities at flux tubes points that are within the gridpoint domain (i.e., within  $\pm 1.5^\circ$  latitude,  $\pm 2^\circ$  longitude and variable height depending on the altitude). For each latitude and longitude the electron density is then extrapolated in the vertical direction up to 20200 km based on a constant scale height which is determined from the two highest grid points that are within the  $L=4$  outer boundary of the flux tubes. At higher latitudes, this can result in extrapolating over large altitude regions. The present study is, however, primarily focused on low latitudes where any errors associated with the height extrapolation of electron densities should be minimal.

### 3.2.4 Results

The longitudinal variations at 17 local time (LT) of the TEC at altitudes above and below 800 km that are observed by the COSMIC satellites and simulated by the GIP-TIEGCM are presented in Figures 3.3 and 3.4 for September equinox and December solstice, respectively. The results for 17 LT can be considered as generally representative of the longitude variations during the daytime and this fact will be shown in subsequent figures. As expected, around September equinox, the longitude variations in the F-region ionosphere (Figures 3.3a and 3.3c) exhibit a primarily wave-4 structure which is attributed to forcing by the  $DE3$  tide. A similar wave-4 feature in longitude is also apparent in both the observations and model results of the topside ionosphere/plasmasphere as shown in Figures 3.3b and 3.3d. In both of these altitude regions, the GIP-TIEGCM is generally

able to reproduce the COSMIC observations. In the F-region, the modeled longitude variations of the maxima in the EIA crest region match the regions of enhanced density observed by the COSMIC. This correspondence is to be expected since we have adjusted the amplitude and phase of the *DE3* forcing at the model lower boundary to obtain an agreement with the observations. Although the longitude variations are in good agreement, the GIP-TIEGCM results show a more distinct EIA compared to the observations. Depending on the geometry of the COSMIC-GPS raypath, there can be a difference of several degrees in latitude and longitude between the top and bottom of the COSMIC electron density profiles and this has the potential to smooth the EIA in the observations. The lack of distinct EIA in the observations may also be related to the assumption of spherical symmetry when determining the electron densities using GPS radio occultation. This assumption can introduce significant errors in the equatorial anomaly region [Yue et al., 2010]. In the topside ionosphere/plasmasphere TEC, although both the model and observations reveal a wave-4 structure in longitude, there is some discrepancy in the location of the maxima. Both the model and observations have maxima near  $100^\circ$  and  $200^\circ$  geographic longitude but the locations of the other two maxima are slightly different. It is also clear that while the model and observations reveal similar longitude variations in the topside ionosphere/plasmasphere, they differ considerably in absolute terms and the observations tend to be 2-3 TECu ( $1 \text{ TECu} = 10^{16} \text{ el/m}^2$ ) ( $\sim 20\%$  at the maxima in longitude) larger. This difference may stem from the electron temperature used in the model which will influence the topside ionospheric scale height. At present, the electron temperature in the GIP-TIEGCM is calculated based on the neutral temperature. We assume that  $T_e = kT_n$ , where  $T_e$  is the electron temperature,  $T_n$  is the neutral temperature, and  $k$  is an empirical factor based on altitude and solar zenith angle. Changing the value of  $k$  will thus change the topside ionospheric scale height and in-turn the absolute levels of TEC in the topside ionosphere/plasmasphere. The 2-3 TECu disagreement between the modeled and observed topside ionosphere/plasmasphere TEC is therefore thought to be partly related to the  $k$  values presently used in the model which may not be appropriate for the extreme solar minimum conditions present during 2008.

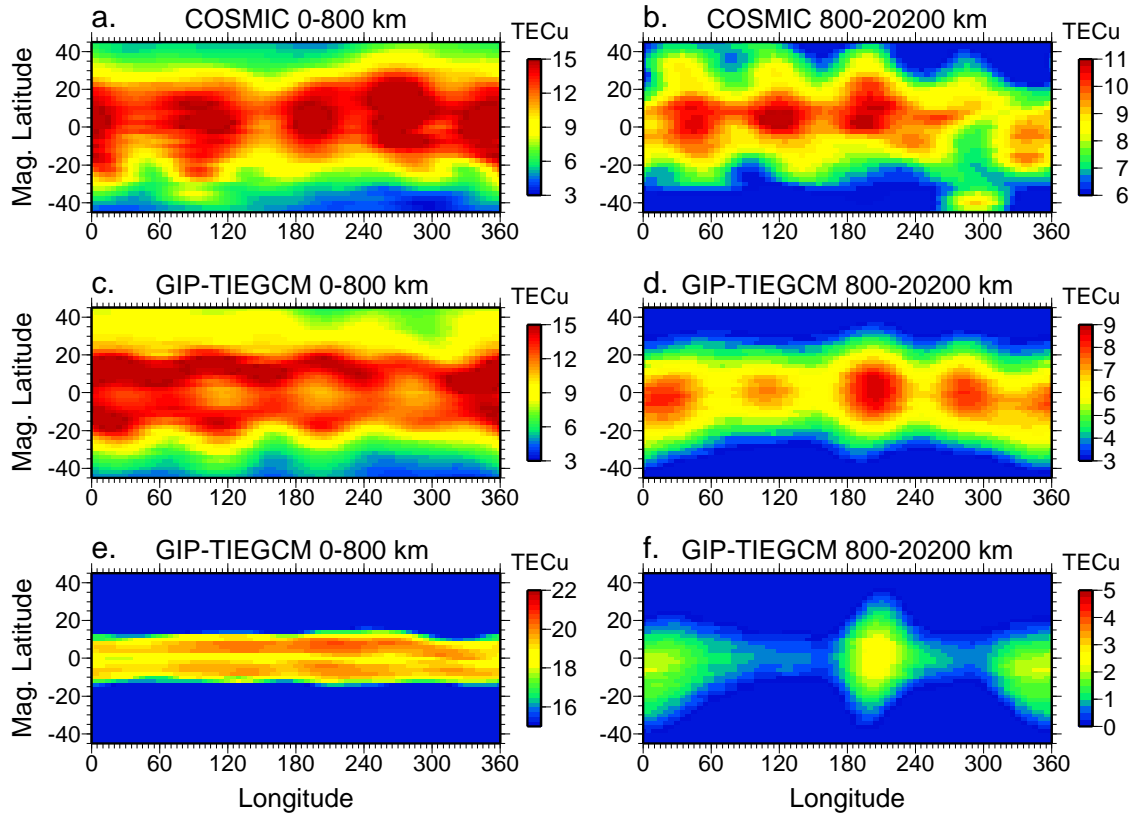


Figure 3.3: Geographic longitude and magnetic latitude variations of the TEC at 17 LT around September equinox for (a) COSMIC observations below 800 km, (b) COSMIC observations above 800 km, (c) GIP-TIEGCM simulation below 800 km without tidal forcing, (d) GIP-TIEGCM simulation above 800 km with tidal forcing, (e) GIP-TIEGCM simulation below 800 km without tidal forcing, and (f) GIP-TIEGCM simulation above 800 km without tidal forcing.

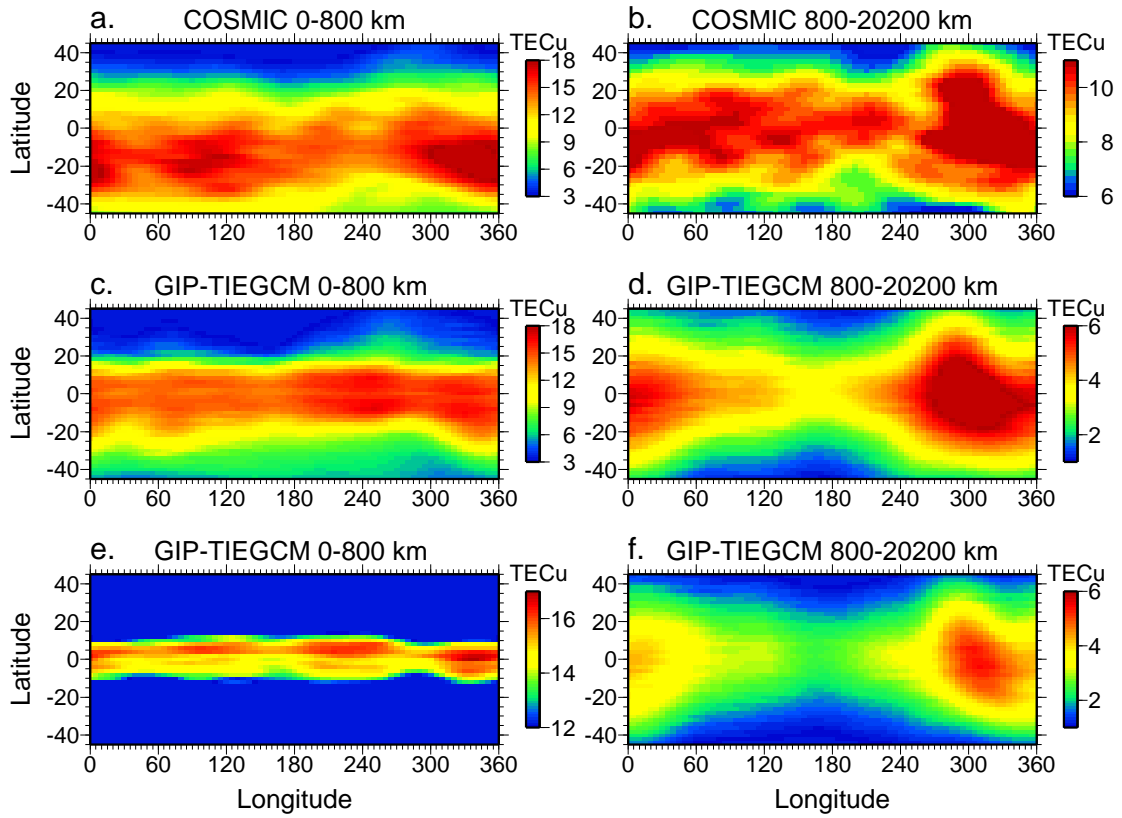


Figure 3.4: Same as Figure 3.3 except for December solstice conditions.

The model results without tidal forcing are shown in Figures 3.3e and 3.3f and longitude variations are apparent. Similar to Hagan et al. [2007], in the absence of nonmigrating tides, only small longitudinal variations occur in the F-region ionosphere. The situation in the topside ionosphere/plasmasphere TEC is different and even without tidal forcing significant longitude variations are present (Figure 3.3f). However, comparison of Figure 3.3c with 3.3e and 3.3d with 3.3f reveal that the longitude variations without tidal forcing are significantly different than those that occur in the presence of tidal forcing. This clearly demonstrates that including nonmigrating tidal forcing in the model is important for reproducing the observed longitude variations. The generation of longitude variations in the absence of tidal forcing will be discussed in detail later.

The observations and model results for December solstice (Figure 3.4) again reveal considerable longitude variations in the F-region ionosphere as well as the topside ionosphere/plasmasphere. These variations are, however, considerably different than those that occur around September equinox due to the dominance of different nonmigrating tides during this time period [Forbes et al., 2008]. The observations exhibit notable maxima in the F-region between roughly  $70\text{-}120^\circ$  and  $300\text{-}360^\circ$ . This longitude variation may be related to the tidal forcing being dominated by *DE2* and *SW4* during Northern Hemisphere winter [Forbes et al., 2008; Pedatella et al., 2008]. The model results in the F-region also exhibit enhancements around  $60\text{-}120^\circ$  and  $300\text{-}360^\circ$ ; however, a maximum is also observed around  $200\text{-}260^\circ$  geographic longitude. The difference in the observed and modeled longitude variation may be related to the climatological forcing that is used at the model lower boundary which may not be fully representative of the conditions during December 2008. The difference could also be related to inaccurate vertical propagation of the tides in the model during December solstice. In the topside ionosphere/plasmasphere, both the model and observations reveal a significant maximum in the TEC beginning around  $260^\circ$  longitude and this feature extends beyond  $0^\circ$  longitude. There are also smaller secondary maxima near  $120^\circ$  and  $200^\circ$  longitude in the observation results. While there is some indication of an enhancement around  $120^\circ$  geographic longitude in the model simulation with tidal forcing, the observed secondary maxima are largely absent from the model results. We again note that significant longitude variations exist

in the absence of tidal forcing as can be seen in Figures 3.4e and 3.4f. Contrary to the September simulation results, the GIP-TIEGCM simulations for December solstice reveal notable longitude variations in both the F-region and the topside ionosphere/plasmasphere and we will discuss these features later.

The evolution of the longitude variations with local time for September equinox and December solstice are presented in Figures 3.5 and 3.6, respectively. The results presented in Figures 3.5 and 3.6 correspond to the average TEC between 10-20°N latitude for the region below 800 km and between  $\pm 10^\circ$  latitude for the topside ionosphere/plasmasphere. These latitudes correspond to the regions where the longitude variations are most pronounced. During the daytime, Figures 3.5 and 3.6 reveal similar longitude variations as shown in Figures 3.3 and 3.4. In December, it is worth noting that both the observations (Figure 3.6a) and model results (Figure 3.6c) of the F-region show fairly similar longitude variations during the daytime. However, there is a slight shift in the local time of the longitude variations and this may account for some of the disagreement between the longitude variations shown in Figures 3.3a and 3.3c. There is a clear difference in the local time behavior of the longitude variations in the two altitude regions. In the F-region, a similar longitude structure tends to dominate at all local times. For example, around September equinox both the observations (Figure 3.5a) and GIP-TIEGCM simulation (Figure 3.5c) reveal a primarily wave-4 feature at all local times. Presuming that the *DE3* is the only tide responsible for generating the wave-4 feature in the F-region, a phase shift of  $90^\circ/24$  hr LT should occur. The dashed lines in Figures 3.5a and 3.5c indicate this phase shift. Although there is a phase shift in the observed and modeled wave-4 feature in the F-region, it is not exactly  $90^\circ/24$  hr LT. This indicates that other nonmigrating tides may be contributing to the wave-4 variation as suggested by Oberheide et al. [2011]. Alternatively, the slightly different phase shift may be related to zonal  $\mathbf{E} \times \mathbf{B}$  drifts which may increase the phase shift during the day and decrease the phase shift at night [Wan et al., 2008]. Unlike the F-region, in the topside ionosphere/plasmasphere significant differences are observed in the daytime and nighttime longitude variations. This is particularly apparent around September equinox where the wave-4 structure that is present during the daytime

is no longer apparent at night. At night, there tends to be two regions of enhanced TEC in the topside ionosphere/plasmasphere TEC. Although to a lesser extent, different longitude variations can also be observed in the daytime and nighttime topside ionosphere/plasmasphere TEC during December solstice.

The seasonal change of the longitude variations observed by the COSMIC satellites in the F-region and topside ionosphere/plasmasphere TEC are presented in Figures 3.7a and 3.7b, respectively. The results shown in Figure 3.7 are the average TEC between 12-18 local time for the same latitude ranges used in Figures 3.5 and 3.6. Figure 3.7a reveals the emergence of a wave-4 variation in longitude during Northern Hemisphere summer that extends into September-October. In Northern Hemisphere winter three maxima (or minima) are apparent. During this time period, minima can be observed near  $60^\circ$ ,  $170^\circ$ , and  $340^\circ$  geographic longitude. The presence to three maxima (or minima) in longitude during Northern Hemisphere winter is consistent with prior observations in the F-region [Scherliess et al., 2008; Pedatella et al., 2008]. In the topside ionosphere/plasmasphere TEC (Figure 3.7b), perhaps the most striking feature is the large seasonal variation that occurs between  $300\text{-}360^\circ$  geographic longitude. The topside ionosphere/plasmasphere TEC is significantly enhanced in this region during Northern Hemisphere winter and exhibits a large depletion during Northern Hemisphere summer. A similar feature and seasonal variation has been observed at dusk in the ion density at 840 km [Huang et al., 2010]. Other longitude variations are also present and, similar to the F-region, a wave-4 variation is observed around both March and September equinoxes.

### 3.2.5 Discussion

Figures 3.3-3.7 clearly demonstrate the presence of longitude variations in both the F-region ionosphere and topside ionosphere/plasmasphere TEC. There are also considerable seasonal and local time variations as previously mentioned. We now turn our attention to understanding the causes of the observed and modeled longitude variations in the topside ionosphere/plasmasphere as well as their similarities and differences with those in the F-region. By far the most dominant

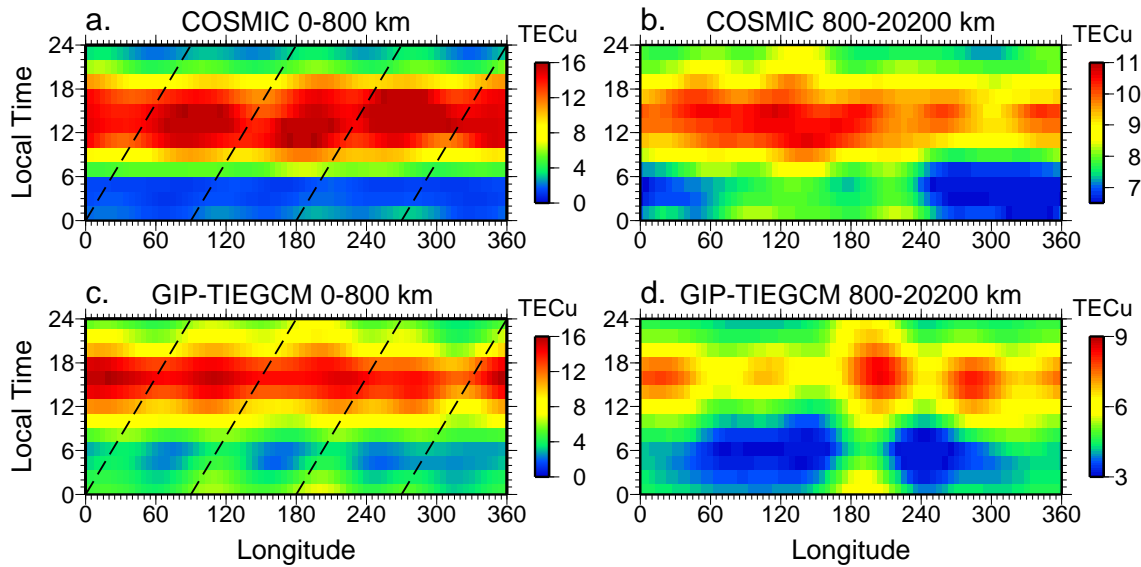


Figure 3.5: The local time and longitude variation of the TEC around September equinox for (a) COSMIC observations below 800 km, (b) COSMIC observations above 800 km, (c) GIP-TIEGCM simulation below 800 km, and (d) GIP-TIEGCM simulation above 800 km. The results for the TEC below 800 km are averages between 10-20°N magnetic latitude and the TEC above 800 km are averaged between  $\pm 10^\circ$  magnetic latitude. The dashed lines in (a) and (c) indicate a phase shift of  $90^\circ/24$  hr LT which is the expected phase speed of the *DE3* in a fixed local time frame.

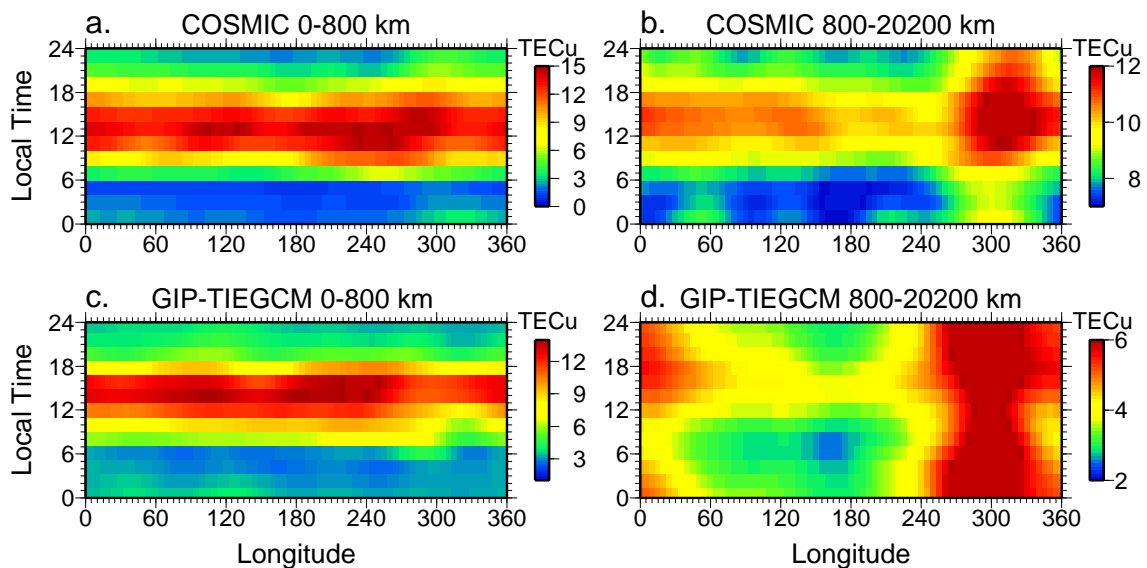


Figure 3.6: Same as Figure 3.5 except for December solstice conditions.

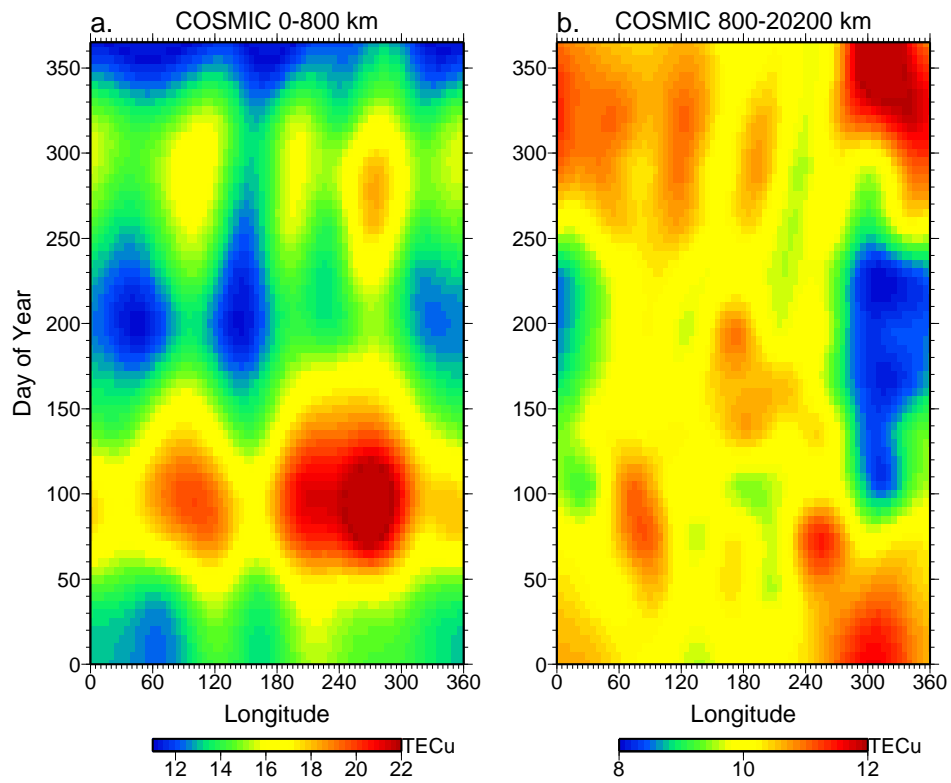


Figure 3.7: The seasonal variation of the longitude structures observed by COSMIC below 800 km (a) and above 800 km (b). The TEC is averaged between 12-18 local time and 10-20°N magnetic latitude for the observations below 800 km and  $\pm 10^\circ$  for above 800 km.

feature in the topside ionosphere/plasmasphere is the significant seasonal variation observed in the TEC between 300 and 360° geographic longitude. Furthermore, this feature is not apparent in the F-region indicating that the mechanism by which this feature is generated is altitude dependent. As previously mentioned, Huang et al. [2010] observed a similar feature and seasonal variation in the topside ionosphere ion densities at dusk near 840 km and they attributed this feature to the large declination of the geomagnetic field in this longitude sector. The combination of the geomagnetic field declination along with the seasonal variation in the neutral winds is thought to either enhance or reduce the field-aligned component of the neutral wind. This results in the large topside ionosphere ion densities (or TEC) during Northern Hemisphere winter and a depletion during Northern Hemisphere summer [Huang et al., 2010]. The field-aligned wind component can significantly influence densities in the topside ionosphere [e.g., Kil et al., 2006] and this effect is therefore most pronounced in the topside ionosphere/plasmasphere which explains its absence in the F-region. Hartman and Heelis [2007] observed a similar longitude and seasonal variation in the topside ionosphere vertical  $\mathbf{E} \times \mathbf{B}$  drifts at dawn. They attributed the longitudinal variations observed near the solstices to be due to the relative orientation of the terminator and magnetic meridian in regions of large declination. While this may explain the longitude variations at dawn, in regions of large declination, Figure 3.6 demonstrates that the enhancement in the topside ionosphere/plasmasphere TEC is observed at all local times. The fact that this feature is present at all local times tends to support the hypothesis that it is generated by enhanced field-aligned winds associated with the orientation of the geomagnetic field. The GIP-TIEGCM simulations without tidal forcing during December solstice (Figure 3.4f) support the fact that the enhanced topside ionosphere/plasmasphere TEC near 300-360° geographic longitude is driven by enhanced field-aligned winds. As this feature appears in the model simulations without tidal forcing it is not a signature of nonmigrating tides originating in the lower atmosphere. While we do not present model simulations for June solstice, we presume that the seasonal variations in the neutral winds would act in combination with the geomagnetic field and result in depleted topside ionosphere/plasmasphere TEC in this region as observed by the COSMIC satellites. Although most pronounced near solstice, the

effect of the geomagnetic field on the longitude variations in the topside ionosphere/plasmasphere is also significant during September equinox (Figure 3.3f).

The effect of the geomagnetic field alone appears to generally have a greater influence on producing longitude variations in the topside ionosphere/plasmasphere compared to the F-region. Nonetheless, the geomagnetic field does introduce some longitude variability in the F-region as can be observed in Figures 3.3e and 3.4e. The GIP-TIEGCM simulations reveal a considerable seasonal variation of the relative importance of nonmigrating tides and the geomagnetic field for producing the longitude variations. Comparison of Figures 3.3c and 3.3e demonstrate that, for September equinox, the inclusion of nonmigrating tides drastically changes the longitude variations at 17 LT in the F-region ionosphere. The situation in December is rather different, and there is some degree of similarity between the GIP-TIEGCM simulations with and without tidal forcing. These results indicate that during time periods around September equinox, when the amplitude of *DE3* is large, the ionospheric longitude variations are dominated by the nonmigrating tides while during Northern Hemisphere winter the role of nonmigrating tides may be of lesser (although not insignificant) importance. That is, during Northern Hemisphere winter, nonmigrating tides and the geomagnetic field orientation may be of roughly equal importance whereas around September equinox the role of nonmigrating tides appears to be of significantly more importance than the geomagnetic field.

While the geomagnetic field clearly plays a significant role in producing longitude variations in the topside ionosphere/plasmasphere, both the COSMIC observations and GIP-TIEGCM simulations reveal the presence of additional features which are not explained by the geomagnetic field alone. This fact is especially apparent around September equinox when a notable wave-4 feature is observed in the topside ionosphere/plasmasphere TEC (Figures 3.3 and 3.5). As seen in Figure 3.3f, the geomagnetic field alone may introduce a wave-2 structure in longitude but both the observations (Figure 3.3b) and GIP-TIEGCM simulations with complete tidal forcing (Figure 3.3d) indicate a wave-4 structure in longitude. Similar to the numerous prior studies on longitude variations in the F-region [e.g., Immel et al., 2006; Lin et al., 2007; Wan et al., 2008] we consider this longitude

structure in the topside ionosphere/plasmasphere TEC to be a signature of nonmigrating tidal influences. However, although modulation of vertical  $\mathbf{E} \times \mathbf{B}$  drifts and the EIA may explain the presence of these variations in the F-region this mechanism may not entirely explain the observed longitude variations in the topside ionosphere/plasmasphere TEC. If the longitude variations were purely driven by the  $\mathbf{E} \times \mathbf{B}$  drifts then similar variations should be present in the F-region and topside/ionosphere plasmasphere and this is not the case. We therefore expect other processes may be contributing. We consider two alternative means by which nonmigrating tides may introduce longitude variability into the topside ionosphere/plasmasphere. First, evidence now exists that nonmigrating tides can penetrate into the thermosphere and influence thermospheric neutral densities and winds, as well as exospheric temperatures [Forbes et al., 2009; Talaat and Lieberman, 2010]. The direct penetration of nonmigrating tides to these altitudes may play a critical role for introducing longitude variations into the topside ionosphere/plasmasphere TEC. The resultant tidal variations in temperatures will introduce longitude variations in the topside ionospheric scale height and thus influence the vertical distribution of plasma in the topside ionosphere/plasmasphere. In the equatorial region, longitude variations have been observed in the topside ionospheric scale height [Liu et al., 2008] indicating that variations in the scale height are a plausible mechanism for the introduction of longitude variations into the topside ionosphere/plasmasphere TEC. Although Liu et al. [2008] did not discuss the cause of the longitude variations in the scale height, they noted that they peak at the equator which is consistent with the tidal perturbations in exospheric temperature observed by Forbes et al. [2009] and the topside ionosphere/plasmasphere TEC observations presented herein. Thus, we believe that the nonmigrating tides may introduce longitude variations into the topside ionosphere/plasmasphere TEC by tidal perturbations in temperature which influence the topside ionospheric scale height.

Nonmigrating tides may also influence the topside ionosphere/plasmasphere due to modulation of F-region densities in combination with the diurnal exchange of plasma between the ionosphere and plasmasphere. In general, the flow between the ionosphere and plasmasphere is upward (flowing from the ionosphere to the plasmasphere) during the daytime and downward

(flowing from the plasmasphere to the ionosphere) at night. During the daytime, the vertical flow of plasma in longitude sectors of enhanced density in the F-region may result in larger topside ionosphere/plasmasphere densities at these longitudes as well. The significant difference in the longitude variations in the topside ionosphere/plasmasphere during the daytime and nighttime supports the fact that these variations may, in part, originate in the F-region. If the longitude variations in the topside ionosphere/plasmasphere partly result from the vertical flow of plasma from the F-region then it is logical that they would disappear at night when plasma flows downward from the plasmasphere into the ionosphere. In fact, this downward flow could potentially serve to maintain the longitude variations in the nighttime F-region.

We consider both of the aforementioned mechanisms for nonmigrating tides generating longitude variations in the topside ionosphere/plasmasphere TEC to be plausible. The most likely scenario is that both of these mechanisms contribute to some degree although it is difficult to specify the relative importance of direct tidal penetration compared to vertical flow from the F-region. The role of the geomagnetic field orientation is also important and the actual longitude variations that are present will be some combination of the effect of nonmigrating tides superimposed upon the variation due to the geomagnetic field.

### **3.2.6 Conclusions**

In the present study we have presented observations and model results of the seasonal and local time variability of longitude structures in the ionospheric TEC above and below 800 km altitude. This has revealed some of the similarities and differences of the longitude variations present in these two altitude regions. The COSMIC observations and GIP-TIEGCM simulations reveal the expected seasonal, local time, and latitude behavior of the longitude structures in the F-region ionosphere. The results presented do, however, provide new insight into the longitude variations present in the topside ionosphere/plasmasphere. The most dominant feature in the topside ionosphere/plasmasphere TEC is a pronounced longitude and seasonal variation observed near 300-360° geographic longitude. At all local times, this longitude region exhibits a distinct minimum during

Northern Hemisphere summer while a maximum is present during Northern Hemisphere winter. Results from a new coupled model indicate that this feature is not related to nonmigrating tides and it is thought to be due to the seasonal variation of the neutral winds in combination with the geomagnetic field orientation.

Both the COSMIC observations and GIP-TIEGCM results also reveal longitude variability in the topside ionosphere/plasmasphere TEC related to nonmigrating tides. This is most apparent in the distinct wave-4 variation in longitude that is present around equinoxes in the daytime topside ionosphere/plasmasphere TEC. The GIP-TIEGCM simulations are able to reproduce this feature when nonmigrating tides are included at the lower boundary and thus indicate that the source of the longitude variations in the topside ionosphere/plasmasphere is nonmigrating tides. We attribute the existence of nonmigrating tidal variations at altitudes in excess of 800 km to two potential mechanisms. First, these may be connected to variations in the scale height related to temperature perturbations. The nonmigrating tidal perturbations in the topside ionosphere/plasmasphere may further be related to the upward flow of plasma from regions of enhanced density in the F-region during the daytime. This second mechanism may explain the similarity between the F-region and topside ionosphere/plasmasphere longitude structures during the daytime and the notable difference in the longitude variations at night when the direction of plasma flow is reversed. Ultimately the longitude variations present in the topside ionosphere/plasmasphere TEC are likely a mixture of effects due to nonmigrating tides as well as those due to the neutral winds in combination with the geomagnetic field orientation.

Lastly, it is important to recognize the fact that the results in the present study are for a single year during solar minimum conditions when the vertical coupling between the lower atmosphere and the ionosphere and thermosphere is enhanced. COSMIC observations during 2009 reveal similar variations in the topside ionosphere/plasmasphere TEC indicating that these structures exhibit stability and are likely to always be present during solar minimum conditions. However, whether similar longitude variations are present during solar maximum remains largely unknown. Additional observations and modeling studies are required to fully understand how the enhanced tidal dissipa-

tion during solar maximum influences longitude variations in the topside ionosphere/plasmasphere.

### 3.3 Inter-annual variability in the longitudinal structure of the low-latitude ionosphere due to the El-Niño Southern Oscillation

#### 3.3.1 Introduction

*DE3* exhibits significant intra-annual variability and it achieves maximum amplitude in August-September and is minimum during December-January [Oberheide et al., 2006; Forbes et al., 2008]. Similar intra-annual variability has been observed in the wave-4 longitudinal structure of the low-latitude ionosphere [England et al., 2009; Liu and Watanabe, 2008; Wan et al., 2008]. These prior studies demonstrate that changes in the amplitude of *DE3* impact the formation and strength of the wave-4 longitudinal structure observed in the low-latitude ionosphere. However, they have only addressed the question of how the intra-annual variability in the wave-4 longitudinal structure is related to the intra-annual variability of the *DE3* amplitude in a climatological sense. Although *DE3* exhibits significant intra-annual variability, *DE3* and other nonmigrating tides can also experience day-to-day and inter-annual variability. Inter-annual variability in the strength of *DE3* was observed by Forbes et al. [2008]; however, the cause of this variability is unknown. Day-to-day variability in the amplitude of *DE3* is closely related with temporal variations in tropical rainfall [Miyoshi, 2006]. Due to the large-scale changes in precipitation and surface temperatures associated with the El Niño Southern Oscillation (ENSO) [Ropelewski and Halpert, 1987; Trenberth et al., 2002] it is not surprising that inter-annual variability in *DE3*, and other nonmigrating tides, is associated with the ENSO. [Gurubaran et al., 2005] observed a decrease in the amplitude of the diurnal tide at mesopause altitudes and attributed this to an increase in the strength of nonmigrating tides associated with the ENSO. During the 1997-1998 El-Niño event, Lieberman et al. [2007] observed large changes in tidal amplitudes due to latent heating in the equatorial region. They reported equatorial increases in *DE1* and *DW3* and a decrease in the equatorial amplitude of *DE3*. Given the connection between the amplitude of *DE3* and the ionospheric wave-4 longi-

tudinal structure along with the possible inter-annual variability in the amplitude of nonmigrating tides due to the ENSO, inter-annual variability might therefore be expected in the amplitude of the wave-4 longitudinal structure.

The primary aim of the present study is to explore inter-annual variability in the wave-4 longitudinal structure of the low-latitude ionosphere and its connection to changes in atmospheric and oceanic circulation resulting from the ENSO. Prior studies on longitudinal structures in the low-latitude ionosphere have relied upon either satellite based measurements [Immel et al., 2006; Lin et al., 2007; Liu and Watanabe, 2008; Pedatella et al., 2008; Scherliess et al., 2008] or GPS TEC observations [Wan et al., 2008]. The combination of limited local time sampling and the relatively short time series available from these observation methods make them ill-suited for studying the inter-annual variability of the wave-4 longitudinal structure. We thus use the ratio of monthly median foF2 values between two ionosonde stations from January 1960 to June 1993 as a proxy for the strength of the wave-4 longitudinal structure. Analysis of GPS TEC reveals that the ratio of ionospheric parameters between two locations is a suitable means for assessing the strength of the wave-4 longitudinal structure in the Northern Hemisphere. This is the first time that inter-annual variability of the wave-4 longitudinal structure has been addressed. Furthermore, we present evidence that the ENSO represents a source of ionospheric variability which has previously not been considered.

### **3.3.2 Data and Methods**

#### **3.3.2.1 Ionosonde Observations**

For the present study we use monthly median foF2 observations during local times of 15-16 hours at the ionosonde stations located at Maui (20.8° N, -156° E geographic; 21.2° N, -90.4° E geomagnetic) and Yamagawa (31.2° N, 130.6° E geographic; 20.6° N, -160.9° E geomagnetic). Local times of 15-16 hours are used in the present analysis since the EIA and wave-4 structure are well established during this time. Data from January 1960 to June 1993 for these two ionosonde

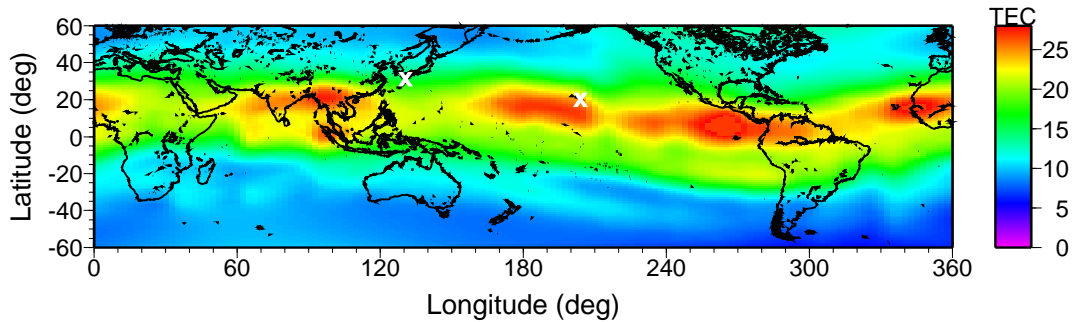


Figure 3.8: Median GPS TEC between 15-16 local time in August 2008 and the location of the ionosonde stations in Maui and Yamagawa (white x's).

stations are available through the National Geophysical Data Center Space Physics Interactive Data Resource (<http://spidr.ngdc.noaa.gov>). The location of these two ionosonde stations along with the monthly median GPS TEC between 15-16 hours local time during August 2008 is presented in Figure 3.8. The monthly median GPS TEC data presented in Figure 3.8 are based on the daily Global Ionosphere Maps (GIMs) during August 2008 produced by the IGS [Dow et al., 2005] (additional details on the GPS TEC processing are provided in Section 3.3.2.2). The global wave-4 longitudinal structure in the August 2008 monthly median GPS TEC can clearly be observed. Figure 3.8 also shows that the Maui ionosonde is located in a longitude sector of enhanced EIA strength while the Yamagawa ionosonde is located near a minimum in the strength of the EIA associated with the wave-4 structure. Due to the location of the ionosonde stations with respect to the longitude sectors of maximum and minimum EIA and wave-4 strength, the monthly median foF2 at Maui is divided by the corresponding value at Yamagawa to obtain a time series of foF2 ratio that is representative of the strength of the wave-4 longitudinal structure. The use of the foF2 ratio as a proxy for the wave-4 structure is validated using GPS TEC observations and further details on this relationship are presented in section 3.3.3.

As the present study is focused on inter-annual variability in the ionospheric wave-4 longitudinal structure we first remove the known variability from the foF2 ratio time series. The wave-4 longitudinal structure around a local time of noon exhibits a solar cycle dependence that is in-

versely related to solar activity [Liu and Watanabe, 2008]. To remove the solar cycle variability, a least squares regression analysis was performed on the the foF2 ratio time series. The regression included a constant term and periodic terms with periods of 10.28 years and 7.86 years. These periodicities correspond to the two dominant periodicities in both the foF2 ratio and the F10.7 cm solar radio flux during the time period of January 1960 to June 1993. It should be noted that the 10.28 year period is significantly stronger than the 7.86 year period; however, the inclusion of the two most dominant periods was necessary to adequately fit the data. The residuals from the regression analysis were then used for the subsequent analysis. Significant intra-annual variability also exists in the strength of the wave-4 longitudinal structure [England et al., 2009; Liu and Watanabe, 2008; Scherliess et al., 2008; Wan et al., 2008]. Using the residuals from the solar cycle fit the intra-annual foF2 ratio climatology is obtained by computing a mean value for each month. The climatological monthly mean values are then subtracted from the solar cycle fit residuals in order to obtain a time series of foF2 ratio monthly anomalies (hereafter referred to as foF2 RMAs). The greater than 40 years of foF2 RMAs provide the extended time series that is desired for the exploration of inter-annual variability in the wave-4 longitude structure.

### **3.3.2.2 Global Positioning System Total Electron Content**

GPS TEC is a column-integral measurement of the electron density from the surface of the Earth to  $\sim 20200$  km; however, it is primarily dominated by F-region electron densities [Klobuchar, 1996]. Therefore, GPS TEC observations can be considered to be proportional to foF2 and we analyze GPS TEC observations in order to validate the use of the foF2 ratio between the two ionosonde stations as a proxy for the wave-4 longitudinal structure. The GPS TEC measurements come from the IGS GIMs [Dow et al., 2005] and are based on slant TEC measurements from a global network of around 200 GPS receivers [Mannucci et al., 1998]. The GIMs have a spatial resolution of  $2.5^\circ$  in latitude and  $5^\circ$  in longitude and a temporal resolution of two hours. The daily GIMs are used to create monthly median GIMs from January 1999 to December 2008. The monthly median TEC observations between  $10^\circ$  N and  $20^\circ$  N magnetic latitude are first normalized by the

zonal mean TEC and then a least squares fit to wavenumbers 0 - 6 is performed to determine the amplitude and phase of each component. The amplitude of the wavenumber-4 component is then used in the subsequent analysis. Since the ionosondes are located in the Northern Hemisphere we have focused only on the longitudinal structure in the northern EIA region due to the possibility of hemispheric asymmetries [McDonald *et al.*, 2008]. The ratio of the monthly median TEC between 20° N, -155° E and 30° N, 130° E geographic is also computed. The solar cycle and intra-annual variability is removed from the time series of GPS TEC wave-4 amplitude and GPS TEC ratio to obtain a time series of monthly anomalies in the same manner as was done for the ionosonde observations. To illustrate the use of the foF2 ratio as a suitable proxy for the wave-4 amplitude, a comparison of the GPS TEC wave-4 amplitude and GPS TEC ratio monthly anomalies has been performed, the results of which are presented in section 3.3.3.

### 3.3.2.3 Oceanic Niño Index

In the present analysis the ENSO variability is represented by the Oceanic Niño Index (ONI). The ONI is a three-month running mean of the Version 3b extended reconstructed sea surface temperature (SST) anomalies [Xue *et al.*, 2003; Smith *et al.*, 2008] in the Niño 3.4 region (-5-5° N, 120-170° W). Values of ONI are available through the National Oceanic and Atmospheric Administration (NOAA) climate prediction center (<http://www.cpc.noaa.gov>). The ONI is used by NOAA for the identification of El-Niño and La-Niña events. El-Niño time periods are associated with an increase in SSTs in the tropical Pacific and thus positive values of the ONI. Likewise, negative values of the ONI occur during La-Niña time periods. El-Niño and La-Niña events influence the large scale atmospheric circulation in different ways and the ONI provides a useful index for tracking these changes.

### 3.3.3 Results and Discussion

Monthly anomalies from January 1999 to December 2008 for GPS TEC ratio and the GPS TEC based wave-4 amplitude are shown in Figure 3.9. The correlation coefficient between the two

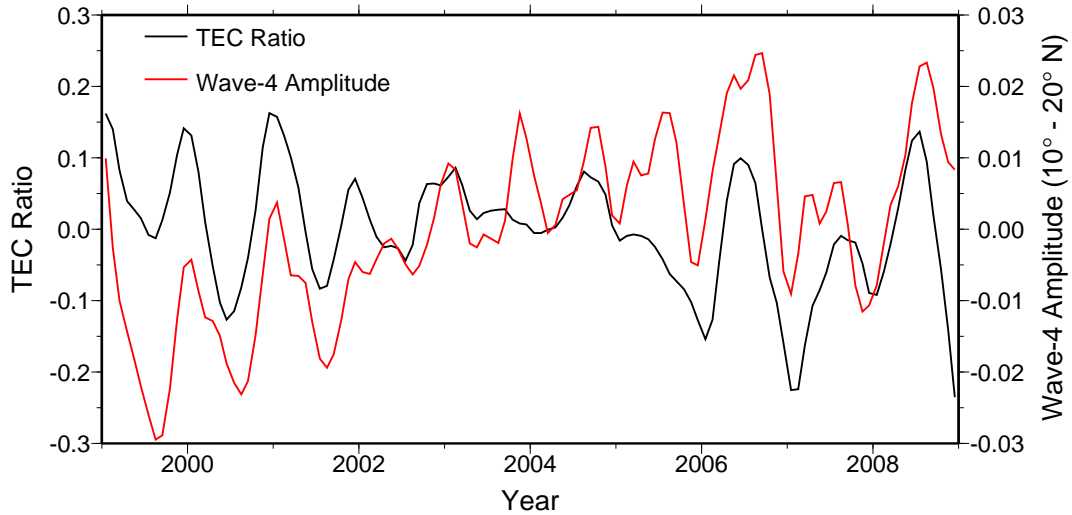


Figure 3.9: Monthly GPS TEC ratio anomalies (black) and the GPS TEC wave-4 amplitude between 10-20° N magnetic latitude (red).

time series is 0.63 indicating reasonably good agreement. Although there are some discrepancies, the general trends in the GPS TEC ratio and the wave-4 amplitude in the Northern Hemisphere are similar. For example, both show anomalously high values during December to February during the initial portion of the time interval and then during July to September in 2006 to 2008. The slight discrepancy between the GPS TEC ratio monthly anomalies and the wave-4 amplitude monthly anomalies may be due to any changes in the location of the longitudinal sectors where the wave-like structure attains maximum amplitude. Removing the climatological monthly mean values eliminates the error due to the ionosphere changing from a wave-4 structure during March to October/November to a wave-3 structure in November/December. However, if the longitudinal structure shifts eastward or westward for a short time period then the TEC ratio may not be in agreement with the wave-4 amplitude.

Given the general agreement between the GPS TEC ratio and the wave-4 amplitude monthly anomalies the ratio between the Maui and Yamagawa monthly median foF2 ratios are judged to represent a suitable proxy for the amplitude of the wave-4 longitudinal structure. Unfortunately, due to a lack of overlap between the two time series, it is not possible to directly compare the

foF2 RMAs with the wave-4 amplitude as derived from GPS TEC observations. The ratio of the monthly median foF2 values from January 1960 to June 1993 is shown in Figure 3.10 along with the solar cycle fit and the 81-day smoothed F10.7 cm solar radio flux. The solar cycle and intra-annual variability is clearly observed in the foF2 ratio values. It is interesting that the amplitude of the wave-4 structure is anti-correlated with solar activity which is consistent with previous observations [Liu and Watanabe, 2008]. This dependence on solar activity is due, at least in part, to the way that molecular dissipation affects the vertical propagation of  $DE3$ , through the temperature dependence of molecular viscosity and conductivity, and the dependence of wave vertical structure on the ratio between wave vertical wavelength and the density scale height [Forbes and Garrett, 1979; Lindzen, 1970; Oberheide et al., 2009; Yanowitch, 1967].

The foF2 RMAs resulting from the removal of the solar cycle and intra-annual variability are presented in Figure 3.11a. The significant amount of remaining variability indicates that these terms do not fully account for the changing amplitude of the wave-4 longitudinal structure. The ONI values also shown in Figure 3.11a appear to correspond loosely with the values of the foF2 RMAs. Although the agreement between the two is far from perfect, similar trends are observed in both. As the ONI values are representative of the ENSO, this indicates that changing atmospheric and oceanic circulations associated with the ENSO may be responsible for part of the variability in the wave-4 amplitude that is not associated with either solar cycle or intra-annual variability.

To further explore the connection between the foF2 RMAs and the ONI we have considered the yearly extreme values. The yearly extreme value (maximum or minimum with the sign maintained) of the ONI and the extreme value of the foF2 RMA in the subsequent five months are shown in Figure 3.11b. Changes in global surface temperature, precipitation and outgoing long wave radiation can all lag behind changes in SSTs [Trenberth et al., 2002] and it is necessary to consider any delay between SSTs and the ionospheric effect. We use the extreme value of the foF2 RMA in the five months after the yearly extreme ONI value to account for any time delay and also any variation in the time delay. The results in Figure 3.11b demonstrate that significant increases or decreases in the ONI are related to similar increases or decreases in the foF2 RMAs. The corre-

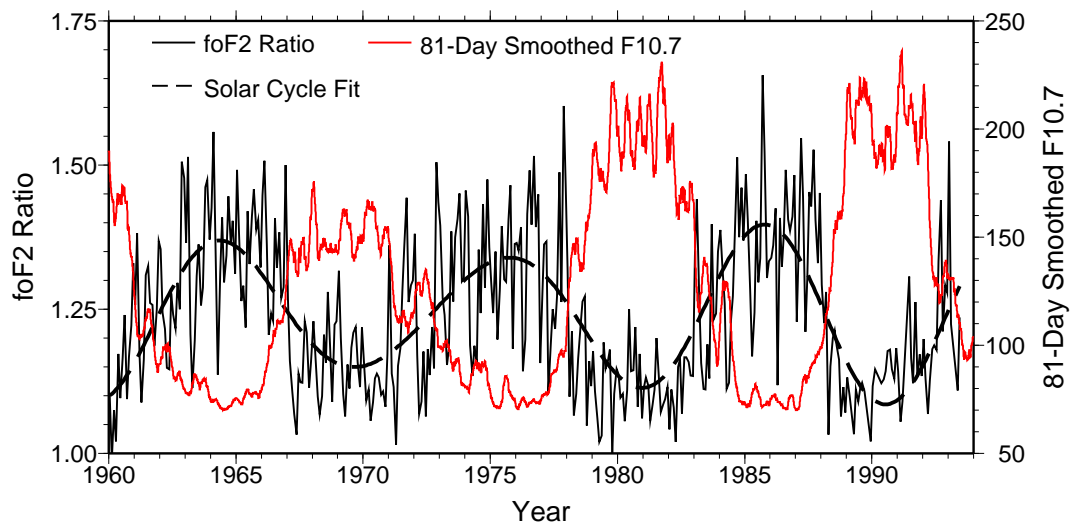


Figure 3.10: Ratio of the monthly median foF2 value between the ionosonde stations in Maui and Yamagawa between local times of 15-16 hrs (solid black) from January 1960 to June 1993. The 81-day smoothed F10.7 cm solar radio flux (red) and the solar cycle fit (dashed black) are also shown.

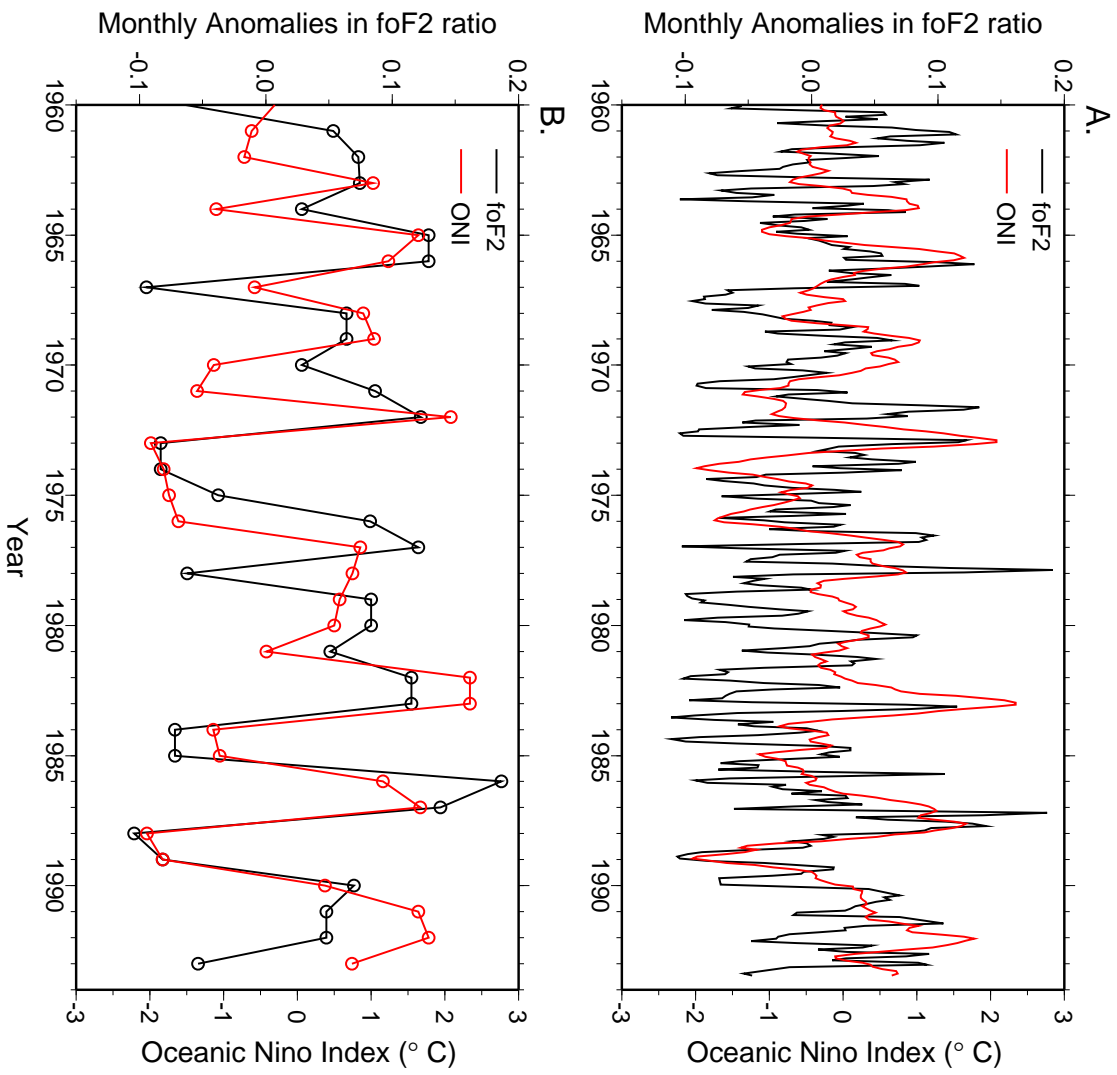


Figure 3.11: (A) Monthly foF2 ratio anomalies (black) and ONI values (red) from January 1960 to June 1993. (B) Yearly extreme value of ONI (red) and the extreme value of foF2 ratio anomalies in the subsequent five months (black).

lation coefficient between the yearly extreme values in ONI and foF2 RMAs in the subsequent five months is 0.70 indicating good agreement between the two time series. This is a fascinating result and strongly suggests that changing SSTs associated with the ENSO are capable of influencing electron densities in the F-region ionosphere. This surprising connection between the ENSO and the F-region ionosphere reveals a new source of inter-annual ionospheric variability. As the foF2 RMAs are thought to be representative of the wave-4 longitudinal structure, it is thought that the inter-annual variability in SSTs associated with the ENSO represents a source of inter-annual variability in the amplitude of the wave-4 longitudinal structure.

The ENSO and associated atmospheric phenomenon occur quasi-periodically [Trenberth, 1976; Gu and Philander, 1994] and a wavelet analysis was performed to reveal if similar periodicities and occurrence times are present in the ONI values and the foF2 RMAs. The wavelet power spectra computed using the Morlet waveform of the ONI and the foF2 RMAs are shown in Figures 3.12a and 3.12b, respectively. To more clearly illustrate the relationship between the two wavelet power spectra the ONI wavelet power spectra contours are overlaid onto the foF2 RMA power spectra in Figure 3.12b. As can be seen in Figure 3.12, the ONI and foF2 RMAs have similar periodicities and occurrence times. This provides further evidence for the possible connection between changing SSTs and the ionosphere wave-4 longitudinal structure.

The results presented in Figures 3.11 and 3.12 demonstrate that the amplitude of the wave-4 longitudinal structure exhibits significant inter-annual variability and that this variability may be attributed in part to changing atmospheric and oceanic circulations associated with the ENSO. We now turn our attention to understanding how changing SSTs associated with the ENSO may introduce variability in the amplitude of the wave-4 longitudinal structure. Several prior studies have revealed changes in tidal amplitudes in the lower atmosphere due to the ENSO. Gurubaran et al. [2005] hypothesized that an observed decrease in the amplitude of the diurnal tide in the mesosphere was due to an increase in the excitation of nonmigrating tides. Furthermore, a significant change in the latent heat forcing of nonmigrating tides over the equatorial region was observed during the 1997-1998 El-Niño event [Lieberman et al., 2007]. The complete spectrum of tidal amplitudes was

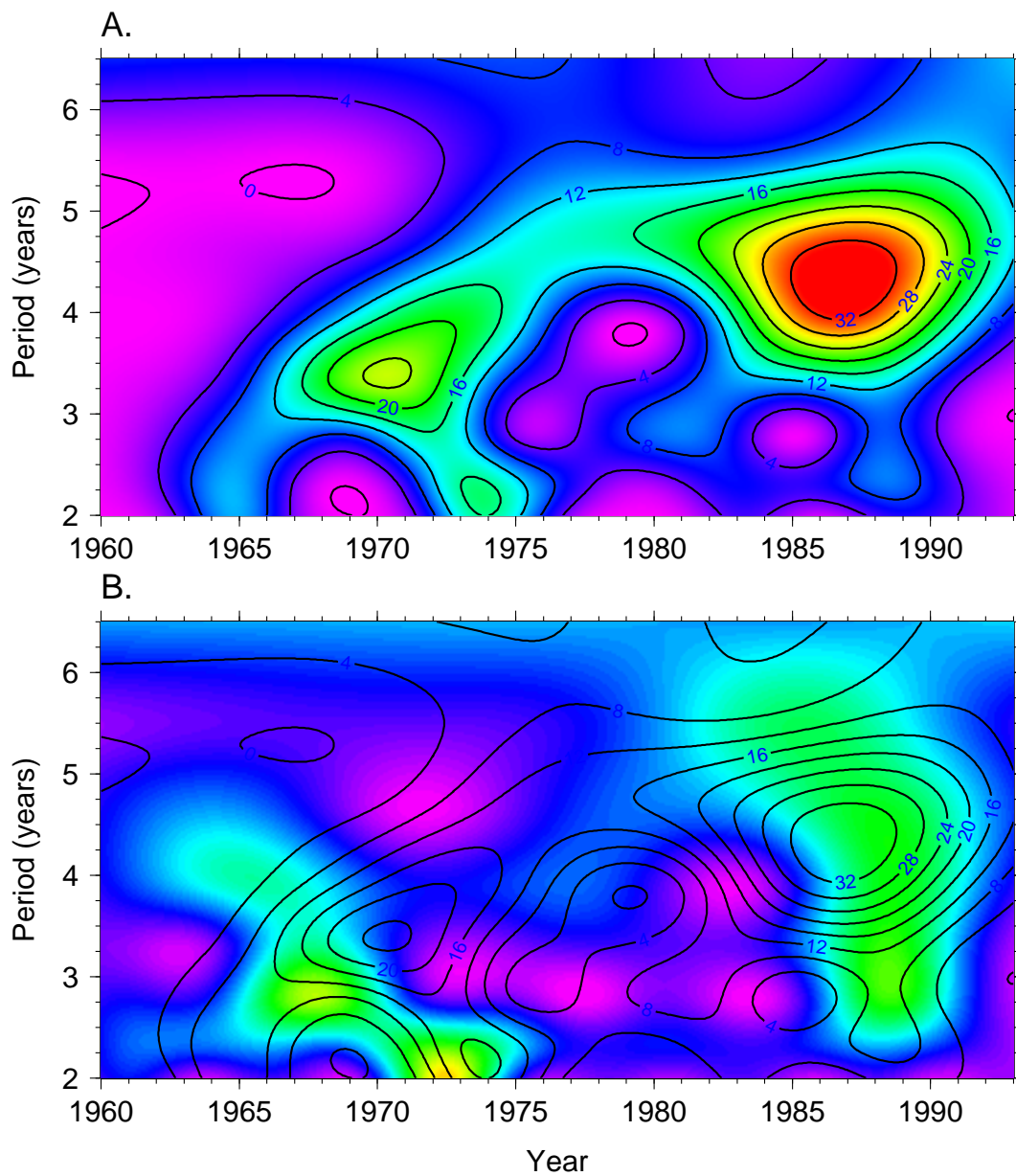


Figure 3.12: (A) Wavelet power spectra of the time series of ONI from January 1960 to June 1993. (B) Wavelet power spectra of the time series of monthly foF2 ratio anomalies. The overlaid contours correspond to the ONI wavelet power spectra.

observed to change with the largest changes being a decrease in the amplitude of *DE3* and an increase in the amplitudes of *DE1*, *DE2*, *DW3*, and *DW4*. As *DE3* is primarily responsible for generating the wave-4 longitudinal structure [Hagan et al., 2007] a decrease in the amplitude of *DE3* should reduce the strength of the wave-4 longitudinal structure. However, in the present analysis we observe an increase in the foF2 RMAAs (and presumably the wave-4 amplitude) in connection with periods of increased SSTs due to the ENSO. This discrepancy is most likely attributable to the fact that the latent heating wave decompositions and inter-annual variabilities presented by Lieberman et al. [2007] were for a single latitude, namely 2.5°S. As the first symmetric mode (Kelvin wave) of *DE3* is of primary importance for modulating the E-region dynamo fields [Forbes et al., 2008], variations in *DE3* heating at a single latitude do not unambiguously reveal how the amplitude of longitudinal structures in the ionosphere may change due to the ENSO. For instance, a decrease in *DE3* heating amplitude at a single latitude could just as plausibly be produced by a latitudinal shift in structure as a uniform decrease in the amplitude of that structure. Thus, the most that we can conclude is that the forcing of nonmigrating tides is likely to be significantly affected by the ENSO, and that this is consistent with our hypothesis concerning the origins of wave-4 variability.

Although the results in Figures 3.11 and 3.12 indicate a connection between the wave-4 longitudinal structure and changing SSTs there are some time periods where the relationship is not so apparent. There are several potential reasons for these discrepancies and future studies are necessitated to further explore how the ENSO influences longitudinal structures in the ionosphere. First, it remains unclear how the ENSO affects the generation of nonmigrating tides. In particular, the extent to which the ENSO influences the amplitude of symmetric mode of *DE3* is not known. Future studies are required in order to understand both the significance of the changes in *DE3* due to the ENSO and also the duration of these effects. Developing a comprehensive understanding of how the symmetric (Kelvin) mode of *DE3* is influenced by the ENSO is fundamental to understanding the observed inter-annual variability in the wave-4 longitudinal structure. Another possible cause of the occasional disagreement between the wave-4 longitudinal structure and the ONI is the use of the foF2 ratio as a proxy for the wave-4 amplitude. The foF2 ratio may not perfectly reflect the

wave-4 amplitude due to either shifting locations of the maxima and minima of the wave-4 structure or changes in the dominant longitudinal structure to wave-2 or wave-3. In the future, as the time series of global ionospheric measurements (such as GPS TEC and satellite measurements) lengthen, it will be possible to explore the inter-annual variability in the wave-4 longitudinal structure directly based on global observations.

### 3.3.4 Conclusions

While previous studies have demonstrated the intra-annual variability in the longitudinal structure of the ionosphere [e.g., Liu and Watanabe, 2008; Pedatella et al., 2008; Scherliess et al., 2008; Wan et al., 2008], the present study has demonstrated that significant inter-annual variability is also present. Using the ratio of foF2 between the ionosondes at Maui and Yamagawa as a proxy for the amplitude of the wave-4 longitudinal structure we have demonstrated that the inter-annual variability is connected with changing SSTs associated with the ENSO. It is thought that the ENSO induces an inter-annual variability in the amplitude of nonmigrating tides which produces a similar inter-annual variability in the wave-4 longitudinal structure.

The fact that changes in SSTs affect the ionosphere several hundred kilometers above the Earth's surface is a surprising new discovery and demonstrates the complex nature of the ocean-atmosphere-ionosphere system. Additional studies are necessary in order to develop a complete understanding of how changing SSTs influence longitudinal structures in the ionosphere. Of primary importance is how the generation of nonmigrating tides is influenced by the ENSO. Given the hypothesis that the inter-annual variability in the wave-4 longitudinal structure is due to inter-annual variability in the amplitude of *DE3*, one may further expect to observe significant day-to-day variability in the strength of the wave-4 longitudinal structure. Immel et al. [2009] demonstrated that significant day-to-day variability is present in the wave-4 longitudinal structure that is associated with day-to-day variability in *DE3*. Although the connection between changing tidal amplitudes in the lower atmosphere and longitudinal structures in the ionosphere is now well established, future studies are necessitated in order to reveal both the causes of variability in the tidal amplitude and

how these changes may influence longitudinal structures in the ionosphere.

### 3.4 Seasonal and longitudinal variations of the solar quiet ( $Sq$ ) current system during solar minimum determined by CHAMP satellite magnetic field observations

#### 3.4.1 Introduction

A common feature of geomagnetic field measurements is the regular daily variation that is clearly observed during geomagnetic quiet time periods. The observed regular daily variations are often referred to as the geomagnetic daily variation or the solar quiet ( $Sq$ ) variation. Given its prominence, the geomagnetic daily variation has attracted significant attention and been extensively studied. Schuster [1889] performed the first detailed study of the geomagnetic daily variation and determined that the current system responsible for producing the geomagnetic daily variation was primarily of external origin, that is, the currents flow above the Earth in the atmosphere. The current system associated with the geomagnetic daily variation is typically termed the solar quiet ( $Sq$ ) current system. There are a number of current systems during geomagnetically quiet time periods and these are all part of the  $Sq$  current system. Such currents include the equatorial electrojet, field-aligned currents and low- and mid-latitude currents that flow in the ionospheric E-region. The present study is concerned with the low- and mid-latitude current system that primarily flows in the E-region and throughout the following when we refer to  $Sq$  current system this is the current system to which we are referring. Following Schuster's [1889] initial determination of the  $Sq$  current system numerous theoretical, observational, and modeling studies have elucidated the primary source mechanisms for formation of the  $Sq$  current system as well as its salient features.

The  $Sq$  current system arises due to the ionospheric wind dynamo. This process has been described in detail in many previous works [e.g., Chapman and Bartels, 1940; Matsushita, 1967; Tarpley, 1970; Richmond, 1989] and therefore is only briefly summarized herein. The ionospheric wind dynamo results from the motion of particles, driven by atmospheric winds, across the Earth's magnetic field, producing an electromotive force and establishing currents and electric fields. The

dynamo generated currents peak at heights between 100 and 170 km owing to the large Pedersen and Hall conductivities at these altitudes. This altitude range is often termed the dynamo region. The dominant factors controlling the structure and strength of the  $Sq$  current system are therefore the neutral tidal winds and the conductivities in the dynamo region.

The importance of tidal winds for the generation of the  $Sq$  current system has been established through various numerical modeling studies. In an effort to determine the tidal winds which primarily generate the  $Sq$  current system, Tarpley [1970] studied the relative importance of different diurnal and semidiurnal tides. It was found that the diurnal tidal winds can largely reproduce the observed current system and that the semidiurnal tide was of significantly less importance. Similar results concerning the relative importance of diurnal and semidiurnal tides were obtained by Stening [1969]. Using more realistic winds in the dynamo region, Forbes and Lindzen [1976] and Richmond et al. [1976] subsequently confirmed the importance of the diurnal winds; however, the semidiurnal tides were found to contribute up to 20% and thus can not be considered insignificant. The importance of semidiurnal winds was further confirmed by Richmond and Roble [1987] who found that the inclusion of realistic semidiurnal tides influenced both the shape and strength of the  $Sq$  current system.

The influence of ionospheric conductivities on the wind dynamo has also been well studied using numerical models. Through modeling the  $Sq$  current system at solar maximum and minimum, Takeda et al. [1986] found that the associated changes in ionospheric conductivity result in variations in the total  $Sq$  current intensity that are greater than a factor of three. The ionospheric conductivity variation between solar maximum and minimum is related to changing solar flux. Related to variable insolation, the ionospheric conductivity also exhibits a seasonal variation with larger conductivities generally occurring in the summer hemisphere. (It is worth noting that greater F-region electron densities associated with the ionospheric winter anomaly can result in larger F-region conductivities in the winter hemisphere [Stening, 1977], but the F-region contributes relatively little to the total  $Sq$  current, which is dominated by E-region currents). This seasonal variation in conductivity leads to a hemispheric asymmetry in the  $Sq$  current system with greater current intensities observed

in the summer hemisphere. For a more detailed discussion on ionospheric conductivity and its variabilities, the interested reader is referred to the work of Richmond [1995a].

In addition to the aforementioned numerical modeling studies which have elucidated the mechanisms primarily responsible for generating the  $Sq$  current system, many observational studies have revealed its primary characteristics as well as variabilities. A comprehensive review of early studies of the  $Sq$  current system is provided by Chapman and Bartels [1940]. The dominant characteristics of the  $Sq$  current system are its seasonal and solar cycle variations. Owing to differences in conductivity and winds, the  $Sq$  current system is not hemispherically symmetric and this feature exhibits a marked seasonal variation with the current intensity in the summer hemisphere being greater than the current intensity in the winter hemisphere. The maximum total currents do, however, typically occur around equinox [Matsushita, 1967; Matsushita and Maeda, 1965; Takeda, 2002]. The overall strength of the  $Sq$  current system also exhibits significant solar cycle variability due to the proportional relationship between ionospheric conductance and solar flux. Observations have revealed that the current strength can be as much as three times greater for solar maximum compared to solar minimum [e.g., Campbell and Matsushita, 1982; Takeda, 2002]. In addition to long-term seasonal and solar cycle variability, significant day-to-day variability in the  $Sq$  current system exists [Hasegawa, 1960]. Such day-to-day variations may be related to changes in the tidal winds due to planetary wave activity [Pancheva et al., 2006]. Lastly, significant longitudinal variability in the  $Sq$  current system has been observed [Matsushita and Maeda, 1965; Matsushita, 1967] and modeled [Stening, 1971; Le Sager and Huang, 2002]. The longitudinal variation of the geomagnetic field was found to largely account for the observed longitudinal variability in the  $Sq$  current system [Stening, 1971].

Although there have been prior studies on the longitude variation of the  $Sq$  current system, limitations to these studies mean that the exact nature and cause of the longitudinal variability remain open questions. While modeling studies have clearly illustrated that the geomagnetic field is an important contributor to generating longitudinal variations in the  $Sq$  currents [Stening, 1971; Le Sager and Huang, 2002], a full spectrum of migrating and nonmigrating tidal winds was not included

in these simulations. It is therefore unclear to what extent the longitudinal variations in tidal winds that are introduced by nonmigrating tides influence the  $Sq$  current system. Furthermore, our present understanding of the longitudinal variation of the  $Sq$  current system is considered incomplete due to the inability to observe the  $Sq$  current system at all longitudes using ground based geomagnetic observations. In recent years, the use of global satellite observations has led to vast improvements in the understanding of spatial variability in the equatorial electrojet and low-latitude ionosphere [e.g., Jadhav et al., 2002; Lühr et al., 2004; Doumouya and Cohen, 2004; England et al., 2006; Immel et al., 2006; Alken and Maus, 2007; Lühr et al., 2008]. Similarly, the use of satellite observations to study the spatial variability of the  $Sq$  current system is desirable in that it offers the opportunity to examine longitudinal variations without the inherent restrictions imposed by ground based observations. In the present study we use observations from the CHAMP satellite magnetometer in order to develop a comprehensive understanding of the longitudinal and seasonal variability of the  $Sq$  current system during the recent solar minimum.

### **3.4.2 Data and Methods**

#### **3.4.2.1 CHAMP Satellite Magnetometer Observations**

##### **Data Selection and Binning**

For the present study, we make use of the vector magnetometer observations from CHAMP during 2006-2008 which are made available through the Information Systems and Data Center operated by Geo Forschungs Zentrum (GFZ) Potsdam (<http://isdc.gfz-potsdam.de>). As a result of atmospheric drag, the orbital altitude of the CHAMP satellite has decayed over the lifetime of the satellite and during 2006-2008 the orbital altitude ranged from roughly 320 to 360 km. The chosen time period can be considered as representative of solar minimum conditions and was selected due to the low levels of geomagnetic and solar activity. During this time period, the F10.7cm solar flux was low and relatively constant which is advantageous in that it allows us to neglect variations in the  $Sq$  current system associated with changing conductivities due to solar flux variations. Solar

minimum conditions are also preferable for the study of vertical coupling between the ionosphere and the underlying atmosphere due to the enhanced vertical propagation of tides [e.g., Forbes and Garrett, 1979]. The enhanced vertical coupling afforded by solar minimum conditions enables a more distinct view of how nonmigrating tidal structures may contribute to longitude variations in the  $Sq$  current system.

The CHAMP vector magnetometer observations contain contributions from a number of sources, such as the main geomagnetic field, ring current,  $Sq$  currents and the equatorial electrojet. To remove the contributions that are not of interest for the present study (i.e., those not associated with the  $Sq$  current system), we first calculate residuals from the POMME6.1 geomagnetic field model [Maus et al., 2011, <http://geomag.org/models/pomme6.html>]. The POMME6.1 model accounts for the main geomagnetic field and its secular variation and acceleration. Fields of magnetospheric origin, and their solar cycle and geomagnetic activity variation, are also removed by the POMME6.1 model. The CHAMP vector magnetometer observations are in a geographic north, east, and vertical coordinate frame and all of the analysis is performed using the magnetic perturbations oriented with respect to the geographic coordinate frame. The residuals for geomagnetically quiet time periods ( $K_p < 3$ ) are binned in magnetic latitude, geographic longitude and universal time. The magnetic latitude is based on the quasi-dipole coordinates [Richmond, 1995b] and, to prevent contamination from auroral currents, only observations within  $\pm 60^\circ$  magnetic latitude are considered. The bin sizes are  $1^\circ$  in magnetic latitude and 1 hr in universal time. We use overlapping longitude bins that are spaced  $15^\circ$  in geographic longitude and are  $20^\circ$  wide. In determining the  $Sq$  current system, it is necessary to account for the satellite altitude and we assume a fixed height of 340 km for all of the observations. The binning is done every ten days (i.e. days 0, 10, 20, ... 350, 360) using a window of  $\pm 40$  days. In the binning procedure the residuals from the years 2006-2008 are combined and any residuals outside of  $\pm 3\sigma$  are removed to eliminate outliers. The  $\pm 40$ -day window is necessitated by the satellite sampling and allows for complete local time coverage when observations from the three years are combined.

### **Determination of Field-Aligned Currents**

Field-aligned and radial currents can contribute significantly to magnetic field observations at satellite altitudes and the perturbations associated with these currents are on the same order of magnitude as those associated with the  $Sq$  current system [Olsen, 1997]. At mid- and high-latitudes, field-aligned currents are approximately in the radial direction and under this assumption Olsen [1997] demonstrated that field-aligned currents introduce perturbations on the order of  $\pm 10$ - $20$  nT to the horizontal magnetic field at satellite altitudes. Lühr and Maus [2006] studied the low-latitude radial currents using CHAMP vector magnetometer observations. They found that, near solar maximum, a meridional current system associated with the equatorial electrojet introduces perturbations to the magnetic field of roughly  $\pm 5$  nT. The present analysis is for solar minimum conditions and the magnetic perturbations associated with radial currents will be less than observed in the aforementioned studies. Nonetheless, given the significant influence that radial currents have been shown to have on satellite magnetic field observations, it is necessary to remove this contribution to the CHAMP vector magnetometer observations. Under the simplification that the field-aligned currents are in the radial direction, the method of Olsen [1997] is used to estimate the field-aligned currents and is briefly described herein. The horizontal residual field can be decomposed into a toroidal ( $\delta \mathbf{B}_{tor}$ ) and poloidal ( $\delta \mathbf{B}_{pol,horz}$ ) part, such that

$$\begin{aligned} \begin{pmatrix} \frac{r}{R} \delta B_\theta \\ \frac{r}{R} \delta B_\lambda \end{pmatrix} &= \delta \mathbf{B}_{tor} + \delta \mathbf{B}_{pol,horz} \\ &= \sum_{n,m} \phi_n^m \begin{pmatrix} \frac{im}{\sin \nu} P_n^m(\nu) e^{im\lambda} \\ -\frac{d}{d\nu} P_n^m(\nu) e^{im\lambda} \end{pmatrix} + \sum_{n,m} \psi_n^m \begin{pmatrix} \frac{d}{d\nu} P_n^m(\nu) e^{im\lambda} \\ \frac{im}{\sin \nu} P_n^m(\nu) e^{im\lambda} \end{pmatrix} \end{aligned} \quad (3.2)$$

where  $r$  is the distance of the satellite to the Earth's center,  $R$  is the radius of the Earth,  $\delta B_\theta$  and  $\delta B_\lambda$  are the magnetic field residuals in the north-south and east-west directions, respectively,  $P_n^m(\nu) = P_n^m(\cos \theta)$  is the Schmidt normalized Legendre function,  $\theta$  is magnetic colatitude,  $\lambda$  is longitude and  $\phi_n^m$  and  $\psi_n^m$  are the spherical harmonic coefficients to be estimated. The first term on the right hand side of Eq. (3.2) represents the toroidal magnetic field perturbation,  $\delta \mathbf{B}_{tor}$ , and is related to radial currents. Similarly, the second term on the right hand side of Eq. (3.2) represents

the horizontal component of the poloidal magnetic field,  $\delta\mathbf{B}_{pol,horz}$  which is caused by toroidal currents. Note that we make the distinction that Eq. (3.2) includes the horizontal component of the poloidal magnetic field because the poloidal magnetic field also has a radial component; however, a similar distinction is not made for the toroidal magnetic field because it does not have a radial component.

For each day and universal time bin, least-squares analysis is performed to estimate the  $\phi_n^m$  and  $\psi_n^m$  coefficients in Eq. (3.2). We estimate the  $\phi_n^m$  and  $\psi_n^m$  coefficients for  $m=0, 1, \dots, 6$  and a maximum degree of  $n=60$ . In estimating the coefficients, a regularization scheme is employed in order to dampen the higher degree harmonics [Olsen, 1997; Marquardt, 1970]. Again following Olsen [1997], we add  $\alpha^2(n) = \alpha_0^2 n^6$  to the diagonal elements of the normal equations and choose  $\alpha_0^2 = 10^{-5}$ . In estimating the  $\phi_n^m$  and  $\psi_n^m$  coefficients, the various parameters in Eq. (3.2) are with respect to two separate coordinate systems. We use magnetic latitude and geographic longitude and the magnetic perturbations are aligned with respect to the geographic frame. This lack of consistency is likely to have some influence on the results, although it is thought that any impact will be relatively minor.

Following the estimation of the  $\phi_n^m$  and  $\psi_n^m$  coefficients for each day and universal time bin, in each magnetic latitude and geographic longitude bin, the north-south and east-west magnetic field perturbations associated with radial currents are removed. That is, we remove the contribution to the residual magnetic field observations that are due to  $\delta\mathbf{B}_{tor}$ . The resulting residuals only contain the poloidal field contributions which are due to toroidal currents and it is then possible to proceed with the estimation of the toroidal  $Sq$  current system as detailed in the following section. Note that, alternatively, the subsequent analysis of the toroidal  $Sq$  current system could be performed using the  $\psi_n^m$  coefficients. Since the least-squares procedure is linear, the results obtained by estimating and removing  $\delta\mathbf{B}_{tor}$  and then estimating the toroidal  $Sq$  current system will be nearly identical (a slight difference may result due to the regularization scheme) to those obtained by estimating these simultaneously.

### **Determination of $Sq$ Current System**

The residuals after removal of the main field model and the contribution from the radial currents should primarily contain contributions from the toroidal  $Sq$  current system. The resultant residuals are thus suitable for determination of the toroidal  $Sq$  currents and we employ the method of spherical harmonic analysis in order to obtain the toroidal  $Sq$  current system. Details concerning the calculation of the toroidal  $Sq$  current system using spherical harmonic analysis can be found in many previous studies [e.g., Chapman and Bartels, 1940; Matsushita, 1967; Winch, 1981] and are not repeated herein. However, the analysis using satellite magnetometer observations is slightly different than that used for ground based observations as outlined in the aforementioned studies. In addition to accounting for the influence of radial currents on the magnetometer observations as previously discussed, it is necessary to take into consideration the altitude of the observations when estimating the equivalent current system. This is important to take into consideration since the CHAMP observations are above the dynamo region where the toroidal  $Sq$  currents primarily flow. Assuming the toroidal  $Sq$  currents flow on a spherical shell at an altitude  $h$ , here taken to be 110 km, the potential function at altitudes  $r > R + h$  can be written as

$$\begin{aligned}
V &= V_{int,ind} + V_{int,Sq} + V_{ext} \\
&= R \sum_{n,m} \left(\frac{R}{r}\right)^{n+1} (a_n^m \cos m\lambda + b_n^m \sin m\lambda) P_n^m(\nu) \\
&\quad + R \sum_{n,m} \left(\frac{n}{n+1}\right) \left(\frac{R+h}{R}\right)^{2n+1} \left(\frac{R}{r}\right)^{n+1} (c_n^m \cos m\lambda + d_n^m \sin m\lambda) P_n^m(\nu) \\
&\quad + R \sum_{n,m} \left(\frac{r}{R}\right)^n (q_n^m \cos m\lambda + s_n^m \sin m\lambda) P_n^m(\nu) \tag{3.3}
\end{aligned}$$

$$\begin{aligned}
&= R \sum_{n,m} \left( Q_n + \left(\frac{n}{n+1}\right) \left(\frac{R+h}{R}\right)^{2n+1} \right) \left(\frac{R}{r}\right)^{n+1} (c_n^m \cos m\lambda + d_n^m \sin m\lambda) P_n^m(\nu) \\
&\quad + R \sum_{n,m} \left(\frac{r}{R}\right)^n (q_n^m \cos m\lambda + s_n^m \sin m\lambda) P_n^m(\nu) \tag{3.4}
\end{aligned}$$

where  $V_{int,ind}$  is the potential due to induced currents internal to the Earth,  $V_{int,Sq}$  is the potential due to the  $Sq$  current system and  $V_{ext}$  is the external potential and is related to currents flowing in the magnetosphere. The corresponding spherical harmonic coefficients are  $a_n^m$  and  $b_n^m$  for  $V_{int,ind}$ ,

$c_n^m$  and  $d_n^m$  for  $V_{int,Sq}$  and  $q_n^m$  and  $s_n^m$  for  $V_{ext}$ . Because both  $V_{int,ind}$  and  $V_{int,Sq}$  are related to currents flowing below the satellite altitude it is not possible to separately estimate these terms from satellite data alone. In going from Eq. (3.3) to Eq. (3.4) we have thus introduced the assumption that Earth induced currents are directly proportional to the  $Sq$  currents. That is, we take that  $a_n^m = Q_n c_n^m$  and  $b_n^m = Q_n d_n^m$ . We further assume a simple conductivity model that consists of an infinite conductor internal to the Earth such that  $Q_n = -\left(\frac{n}{n+1}\right)\left(\frac{c}{R}\right)^{2n+1}$ , where  $c$  is the radius of the conducting shell and we take  $c = R - 600km$  [e.g., Olsen et al., 2005; Chapman and Bartels, 1940]. Such a simple conductivity model is limited in that it does not account for any phase lag between the  $Sq$  and induced currents. Spatial variations in the conductance can also have a considerable influence on the induced currents [Kuvshinov et al., 2007]. In Eq. (3.3) and Eq. (3.4),  $c_n^m$  and  $d_n^m$  are defined as the external coefficients at the Earth's surface associated with the toroidal  $Sq$  current. The  $\left(\frac{n}{n+1}\right)\left(\frac{R+h}{R}\right)^{2n+1}$  term arises from how we define  $c_n^m$  and  $d_n^m$  and the condition that the gradient of the potential in the radial direction is continuous at an altitude of  $r = R + h$  [Langel et al., 1996].

Utilizing the fact that  $\mathbf{B} = -\nabla V$ , the residual magnetic perturbations can be used to estimate the spherical harmonic coefficients in Eq. (3.4). This is done in a manner similar to ground based observations where the perturbation in the vertical direction is used to separate the contribution from internal and external currents. For the present study, a least-squares fitting procedure is used to estimate the spherical harmonic coefficients and the magnetic residuals in the north-south and east-west directions are fit simultaneously to estimate the spherical harmonic coefficients in Eq. (3.4). Separately fitting either the north-south or east-west perturbations generally yields similar results. However, these are not identical and can occasionally be rather different, indicating that our assumption that the magnetic perturbations can be wholly represented by a potential function is invalid. In the present study, the spherical harmonic analysis is performed for order  $m=0, 1, \dots, 6$  and for a maximum degree of  $n_{max}=m+9$ . Performing the analysis using higher degree harmonics did not significantly influence the resultant  $Sq$  current systems and the results presented using the chosen  $n_{max}$  represent all of the salient features. As the present study is concerned with longitudinal

variations, the spherical harmonic coefficients are estimated separately for each longitude bin under the assumption that longitude and local time are equivalent in the spherical harmonic analysis. That is, in Eq. (3.4) we replace  $\lambda$  with  $t_{LT}$ , where  $t_{LT}$  is the local time. Longitude and local time are not necessarily equivalent in Eq. (3.4); however, separate estimation of the  $Sq$  currents at fixed universal times yields similar results indicating that our assumption of longitude and local time equivalence in the analysis is valid. Following the estimation of the spherical harmonic coefficients, the  $c_n^m$  and  $d_n^m$  terms can be used to determine the equivalent current function using standard techniques [e.g., Chapman and Bartels, 1940; Matsushita, 1967]. In calculating the equivalent current function we again assume that the currents flow at an altitude of 110 km.

### 3.4.2.2 Ground Magnetometer Observations

Ground based magnetometers are utilized to provide a means for validating the  $Sq$  currents that are calculated from the CHAMP vector magnetometer observations. The  $Sq$  current system is determined based on a chain of magnetometers in the African/European longitude sector. The magnetometer data is provided by the National Geophysical Data Center (NGDC) Space Physics Interactive Data Resource (<http://spidr.ngdc.noaa.gov/>) and a listing of the observatories used is provided in Table 3.2. It is worth noting that the geomagnetic observatory Addis Ababa (AAE) is located under the equatorial electrojet. Since the electrojet is a relatively strong and latitudinally narrow feature, inclusion of AAE in the analysis has the potential to introduce considerable error due to the inability of the ground magnetometer chain to fully resolve the equatorial electrojet. Analysis was also performed without AAE and yielded similar results indicating that the inclusion of a single station under the equatorial electrojet does not significantly influence the results presented herein.

For consistency, we obtain the  $Sq$  current function from the ground based magnetometer observations in the same manner as used for the CHAMP satellite vector magnetometer observations. We thus similarly combine the data from 2006-2008 and estimate the current function every ten days using  $\pm 40$  days of observations. Contribution from fields of magnetospheric origin are

Table 3.2: Geographic locations of the ground based magnetic observatories used in the calculation of the equivalent external  $Sq$  current system from 2006-2008.

Station Location	Station Name	Geographic Latitude (°)	Geographic Longitude (°)
Nurmijarvi, Finland	NUR	60.50	24.65
Borok, Russia	BOX	58.03	38.07
Hel, Poland	HLP	54.61	18.82
Kiev, Ukraine	KIV	50.72	30.30
Grocka, Serbia	GCK	44.63	20.77
San Fernando, Spain	SFS	36.46	353.79
Guimar, Spain	GUI	28.48	343.74
Tamanrasset, Algeria	TAM	22.79	5.53
M'Bou, Senegal	MBO	14.39	343.04
Addis Ababa, Ethiopia	AAE	9.03	38.77
Ascension Island	ASC	-7.90	345.60
Tsumeb, Namibia	TSU	22.79	17.70
Hartebeesthoek, South Africa	HBK	-25.88	27.71
Hermanus, South Africa	HER	-34.43	19.22
Port Alfred, Crozet Islands	CZT	-46.43	51.87

also removed from the ground-based observations using the POMME6.1 model. The effect of field aligned currents on the equivalent external current function is relatively small [e.g., Richmond and Roble, 1987] and we thus neglect their contribution to the ground based magnetic perturbations. We again perform the spherical harmonic analysis for order  $m=0, 1, \dots, 6$  and for a maximum degree of  $n_{max}=m+9$ . The typical methods for spherical harmonic analysis of ground based observations as well as the separation into internal and external parts are applied and details on these computations can be found in previous works [e.g., Chapman and Bartels, 1940; Matsushita, 1967; Winch, 1981]. For ground based observations, the toroidal  $Sq$  current system contributes to the external potential. In the subsequent section we thus present equivalent external current functions for the ground based observations and again assume that the currents flow at a height of 110 km. Similar to the analysis of the CHAMP observations, the ground based analysis is carried out using magnetic perturbations oriented in a geographic frame and the north-south and east-west perturbations are simultaneously fit in the spherical harmonic analysis.

### 3.4.3 Results and Discussion

#### 3.4.3.1 Comparison between CHAMP and ground magnetometer observations: seasonal variation

To confirm the viability of using the CHAMP vector magnetometer observations for determining the  $Sq$  current system, we first present the seasonal variation of the  $Sq$  current function based on CHAMP observations along with the current function derived from ground based magnetometers. Figure 3.13 presents  $Sq$  current functions based on zonal mean CHAMP observations and those based on ground magnetometers during June (Figures 3.13a and 3.13b) and December (Figures 3.13c and 3.13d) solstices. Note that throughout the following discussions, it is important to remember that the results are based on  $\pm 40$  days of observations and therefore the results for any time period (e.g., solstice or equinox) are reflective of conditions in the surrounding  $\pm 40$  days. In general, the agreement between the current functions obtained using the different observations

is good. The peak in the current functions during daytime are fairly similar and the latitude of the foci are also in agreement. There are, however, some differences that are worthy of discussion. First, we note that there are some slight differences in the absolute values of the current functions. This discrepancy is thought to be related to the fact that the CHAMP  $Sq$  currents presented in Figure 3.13 are zonal means and, as will be discussed later, there are significant longitudinal variations. It is not too surprising then that the zonal mean currents do not match those that are restricted to a specific longitude sector. This difference may also stem from the simple conductivity model used to account for the induced currents in the CHAMP observations. We also note that there is a slight phase difference between the two observations with the maximum in the daytime current function occurring earlier in ground based data. This difference may again be related to the comparison of zonal mean observations with those from a restricted longitude zone. Although, in the present discussion we have elected to show the zonal mean CHAMP  $Sq$  current functions, results for the longitude sector that is similar to the longitude of the ground magnetic observatories will be presented in section 3.4.3.2, affording a more accurate comparison.

The seasonal variation of the daytime  $Sq$  current system is presented in Figure 3.14, where values of the current function at 12 local time (LT) are shown as a function of latitude and day of year. We note that in the Southern Hemisphere the daytime current function is typically negative and an enhancement in the current will correspond to a decrease in the current function (i.e. it becomes more negative). Because minima in the Southern Hemisphere current function are related to enhanced currents, we will refer to Southern Hemisphere minima as maxima throughout the remainder of the text. In Figure 3.14, we note that generally similar variations are observed in both the CHAMP and ground magnetometer current functions at 12 LT. The slight differences may again be related to the fact that the CHAMP results are representative of the zonal mean while the ground based magnetometers are restricted to the African/European longitude sector. A seasonal variation can clearly be observed in the values of the current function at 12 LT presented in Figure 3.14. A predominantly annual variation is observed in the Northern Hemisphere with the peak value occurring near the June solstice. The seasonal variation in the Southern Hemisphere

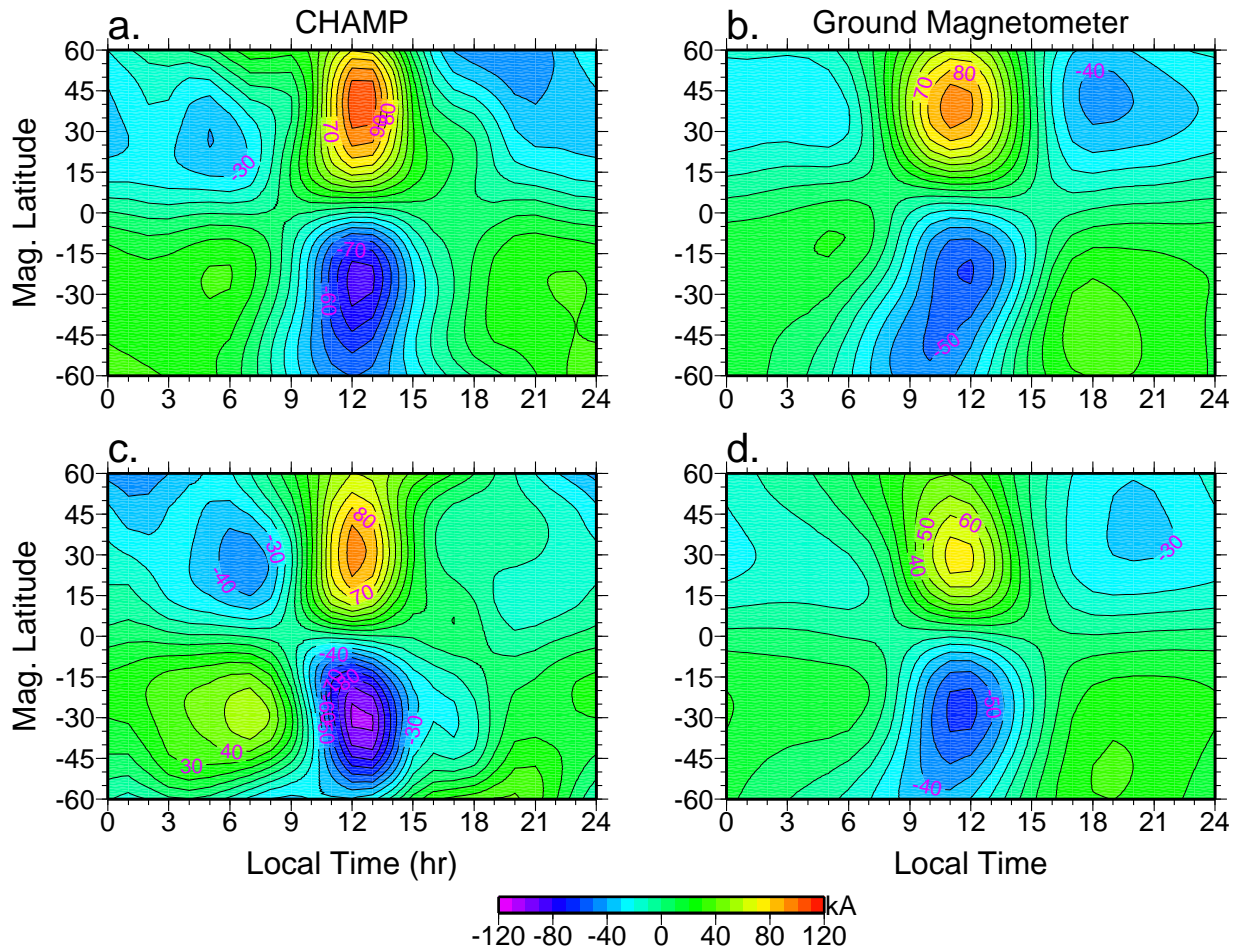


Figure 3.13:  $Sq$  current functions during June solstice for (a) CHAMP zonal mean and (b) ground based magnetometers. (c) and (d) are the same as (a) and (b) except for December solstice.

is different and exhibits a primarily semiannual oscillation with maxima near the equinoxes. The seasonal variations observed in Figure 3.14 are generally consistent with prior studies. Campbell and Matsushita [1982] presented results for the seasonal variation in the Northern Hemisphere for solar maximum and solar minimum. They observed a primarily annual variation during solar minimum conditions and a semiannual variation during solar maximum. Takeda [2002] similarly observed a dominant semiannual variation during solar maximum. However, during solar minimum, Takeda [2002] observed an annual variation in the Northern Hemisphere and a semiannual variation in the Southern Hemisphere. This is consistent with our results which are representative of solar minimum conditions and provides further validation that the CHAMP vector magnetometer observations can reliably determine the global  $Sq$  current system.

The results presented in Figure 3.14 also reveal the expected hemispheric asymmetry in the current function at 12 LT. The hemispheric asymmetry is most apparent during Northern Hemisphere summer when considerably stronger currents are observed in the Northern Hemisphere. The latitude of the Northern Hemisphere focus also moves poleward during this time period. The observed hemispheric asymmetry during Northern Hemisphere summer is as expected based on theoretical considerations. Owing to increased insolation, the conductivities in the dynamo region are greater in the summer hemisphere and this results in the observed greater equivalent current functions in the summer hemisphere. Tidal winds can also contribute to the asymmetry in the  $Sq$  current function around solstice, specifically with regards to shifting of the focal latitude [Stening, 1969]. Around December solstice, the hemispheric asymmetry is small and is significantly less pronounced relative to the asymmetry that is observed around June solstice. This difference may be related to the semiannual variation in the Southern Hemisphere that was previously discussed. The semiannual variation in the Southern Hemisphere results in a hemispheric asymmetry near the equinoxes with greater peak daytime current function values in the Southern Hemisphere at these times. Lastly, we note that the observed hemispheric asymmetry is considerably less than the asymmetry observed in previous studies [e.g., Chapman and Bartels, 1940; Matsushita and Maeda, 1965; Takeda, 2002]. This discrepancy is thought to stem from the use of a  $\pm 40$  day data window.

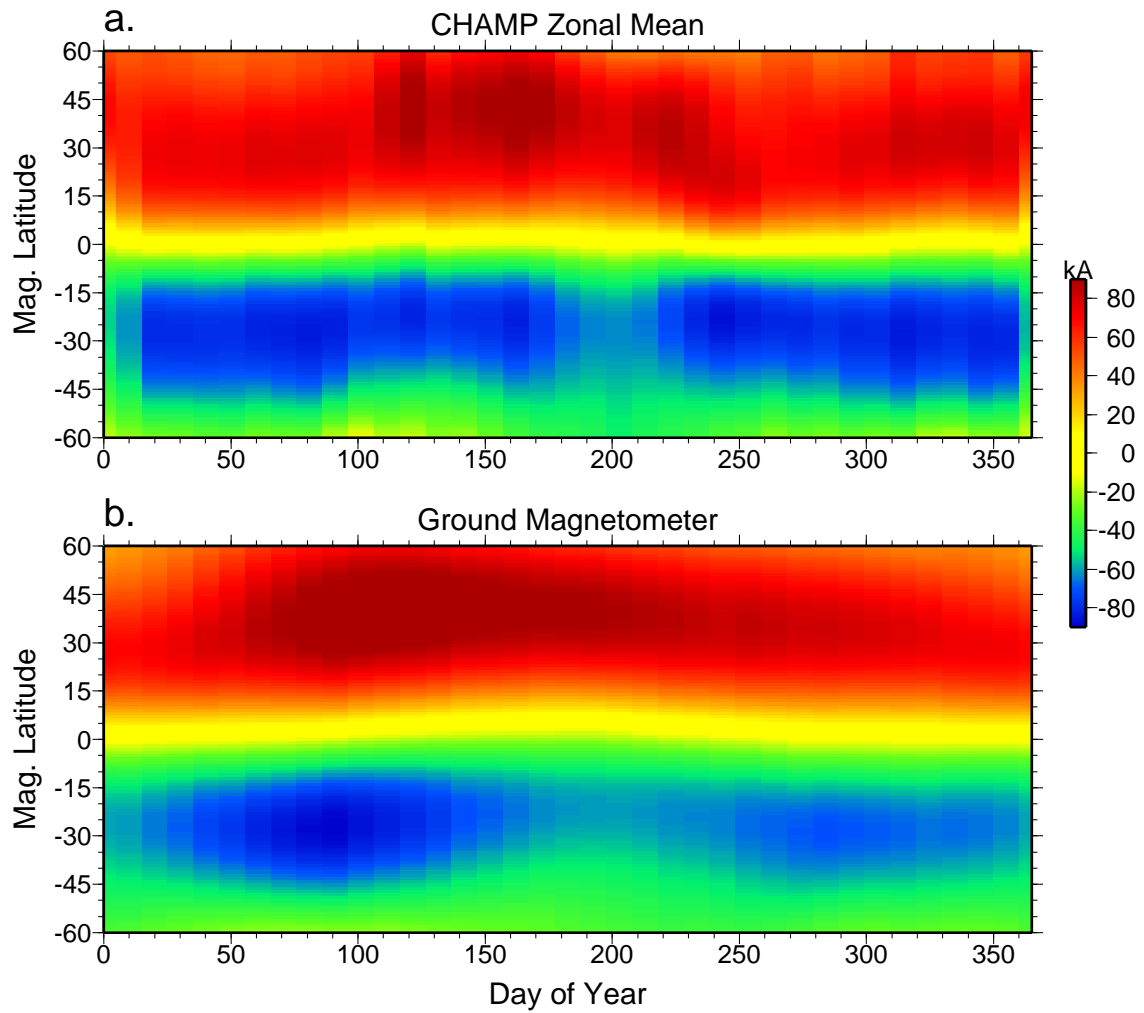


Figure 3.14: Seasonal variation of the current function at 12 local time as a function of magnetic latitude for (a) CHAMP zonal mean and (b) ground based magnetometer observations.

Such a large data window is necessary due to the local time sampling of the CHAMP satellite; however, it has the potential to result in smoothing of the seasonal variations making them less pronounced.

### 3.4.3.2 Longitudinal Variations

We now turn our attention to the variations in longitude of the  $Sq$  current system based on the CHAMP vector magnetometer observations. Figure 3.15 presents the  $Sq$  current function for each season (March equinox, June solstice, September equinox, and December solstice) and for the longitude bins centered at  $37.5^\circ$  and  $232.5^\circ$  geographic longitude. Prior to discussing the longitudinal differences it is worth noting that the  $Sq$  current functions at  $37.5^\circ$  longitude during the solstices (Figures 3.15c and 3.15g) agree well with the ground based magnetometer observations that are shown in Figures 3.13b and 3.13d. We note that the agreement between the two is slightly better when only considering the CHAMP observations at roughly the same longitude as the ground magnetometer observations. Thus, as discussed previously, some of the disagreement between the CHAMP and ground based observations in Figures 3.13 and 3.14 is likely the result of using the zonal mean CHAMP observations. In Figure 3.15, it is readily apparent that there are significant differences between the  $Sq$  current functions at the two longitudes that are shown. Around March equinox and June solstice, the peak in the current function at  $37.5^\circ$  longitude is notably greater than the current function maximum at  $232.5^\circ$  longitude. Interestingly, the opposite is true during December solstice and the maxima in the current functions are fairly similar during September equinox. Matushita and Maeda [1965] previously studied the longitudinal inequalities in the  $Sq$  current system. However, a comprehensive comparison between our results and those of Matushita and Maeda [1965] is complicated by the fact that their results are based on ground magnetometer observations in three different longitude zones and are for solar maximum conditions. Nonetheless, it is possible to make a rough comparison, and there are several similarities between the present results and those presented by Matushita and Maeda [1965]. During June solstice, Matushita and Maeda [1965] similarly observed greater peak values in the current function in the region around

37.5° geographic longitude compared to those around 232.5° longitude. Likewise, during December solstice they observed larger current function values in the Southern Hemisphere around 232.5° geographic longitude compared to 37.5° longitude; however, in the Northern Hemisphere, the peak in the current function was slightly greater near 37.5° longitude. Longitudinal variations resembling the observational results of Matushita and Maeda [1965] have also been successfully modeled by Stening [1971] and the source of the longitudinal inequalities was attributed to longitudinal variations in the Earth's geomagnetic main field.

To gain a more comprehensive understanding of the longitudinal variations, Figure 3.16 presents values of the current function at 12 LT as a function of latitude and longitude for each season. As previously mentioned, since a minimum in the Southern Hemisphere in Figure 3.16 is related to enhanced  $Sq$  currents we will refer to these as maximum. Significant longitudinal variations can clearly be observed in Figure 3.16 and they vary with season. With the exception of December solstice, a pronounced minimum in the current function at 12 LT occurs between ~180-250° geographic longitude. In December, the minimum in the current function at 12 LT is shifted and is located around 320-360° geographic longitude. It should be noted that the observed minima and maxima in longitude are not related to movement of the maximum in the current function away from 12 LT. Similar longitude variations are observed at other local times indicating that the longitude variations at 12 LT are due to regions of enhanced or decreased current intensity. The observed seasonal variation of the longitude variations are roughly consistent with prior observations and modeling [e.g., Matushita and Maeda, 1965; Stening, 1971]. The present observations do, however, reveal the longitudinal variations with an unprecedented clarity and are able to provide a more complete understanding of the longitudinal variations and their seasonal dependence. In particular, we note that although there tends to be a pronounced region of minimum in the current function, there are also several maxima in longitude. For example, around September equinox three maxima can clearly be identified near 0°, 120° and 300° in both the Northern and Southern Hemispheres.

Several prior studies have investigated the longitudinal dependence of various ionospheric

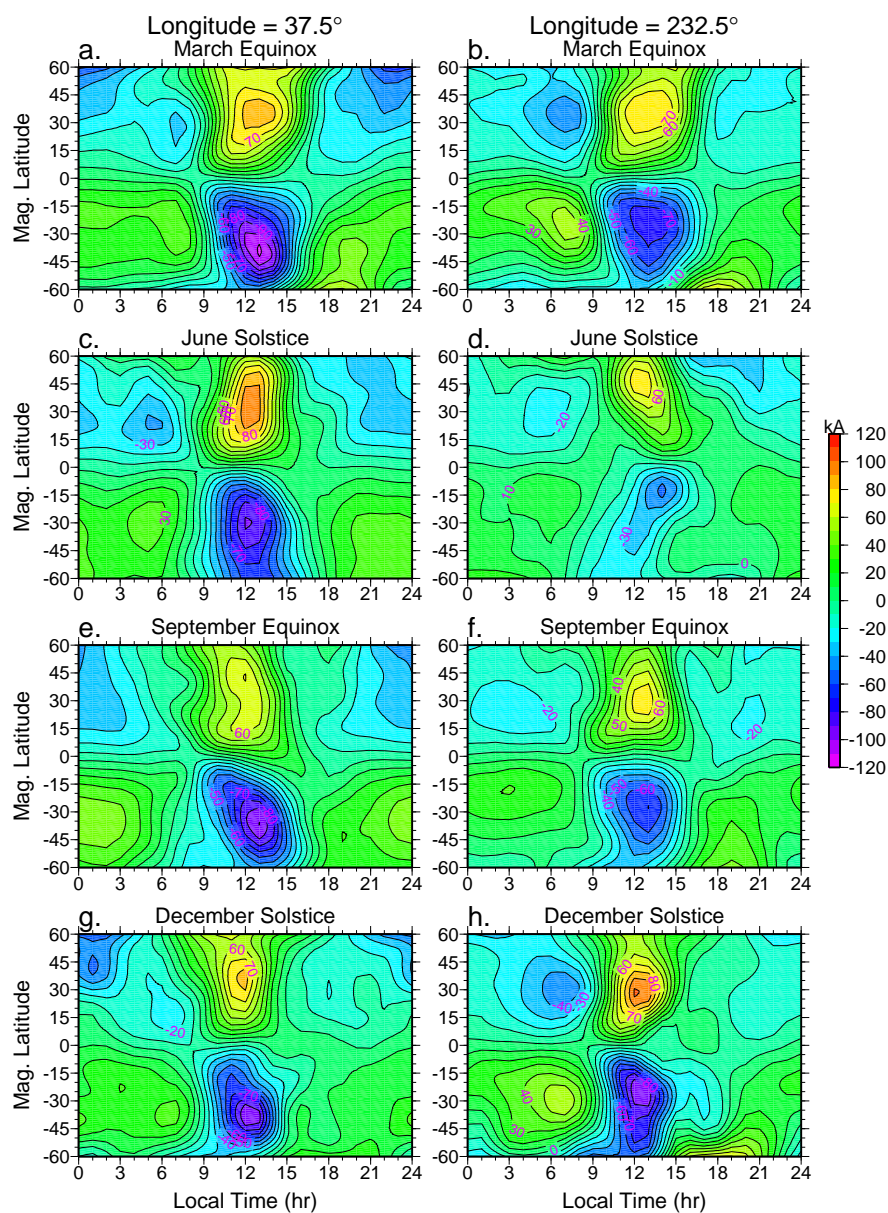


Figure 3.15: *Sq* current functions derived from CHAMP magnetometer observations for geographic longitudes of  $37.5^\circ$  (a, c, e, and g) and  $232.5^\circ$  (b, d, f, and h) for the seasons indicated on each panel.

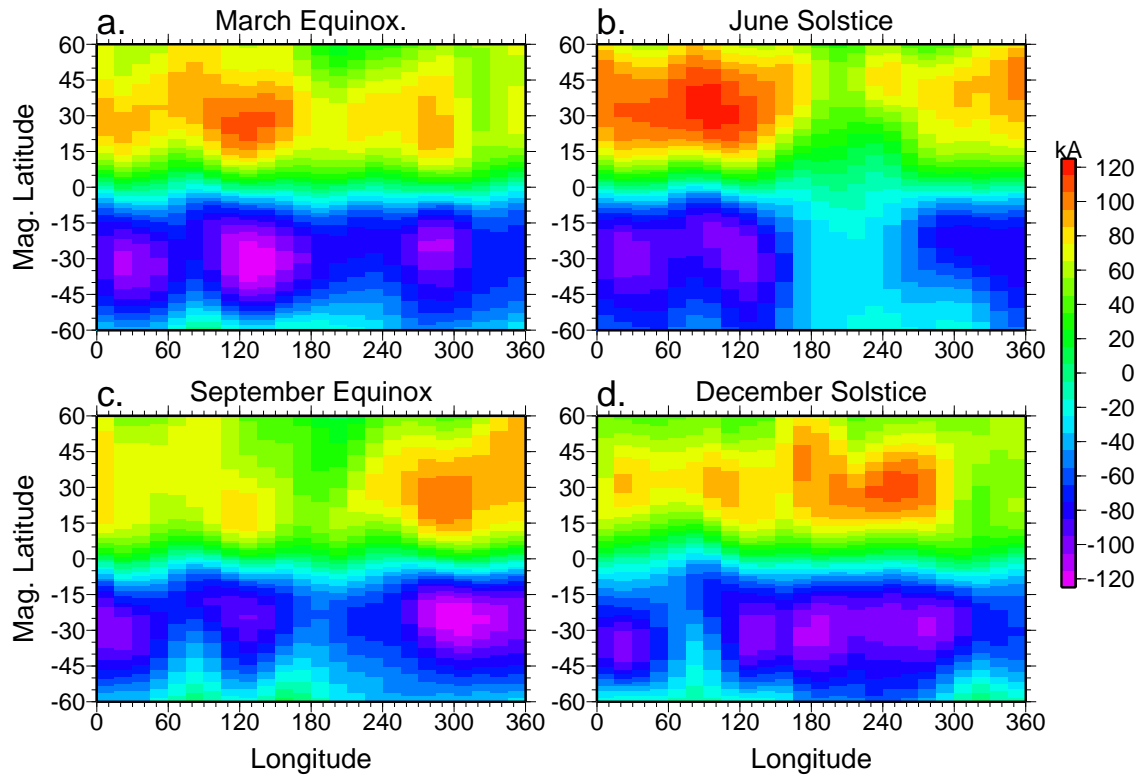


Figure 3.16: Longitudinal variation of current function at 12 local time as a function of magnetic latitude for (a) March equinox, (b) June solstice, (c) September equinox, and (d) December solstice.

parameters such as the equatorial electrojet, vertical drifts and low-latitude ionospheric densities [e.g., Jadhav et al., 2002; Lühr et al., 2004; Alken and Maus, 2007; Kil et al., 2007; Doumouya and Cohen, 2004; Fejer et al., 2008; Lühr et al., 2008]. It is thus useful to briefly discuss our results of longitude variations in the  $Sq$  current function in the context of previous studies. Both Kil et al. [2008] and Fejer et al. [2008] presented the seasonal, longitudinal, and local time variation of ROCSAT-1 low-latitude vertical  $\mathbf{E} \times \mathbf{B}$  drifts. A number of studies have also focused on the seasonal and longitude variation of the equatorial electrojet [Jadhav et al., 2002; Alken and Maus, 2007; Doumouya and Cohen, 2004; Lühr et al., 2008]. Although there are some minor differences in the location of the maxima in longitude, all of these studies have demonstrated that the equatorial electrojet exhibits generally similar seasonal and longitude variations as the low-latitude vertical  $\mathbf{E} \times \mathbf{B}$  drifts. This correspondence is expected since the eastward electric field that drives the F-region vertical drift and E-region electrojet current is similar at both heights. Both the daytime vertical  $\mathbf{E} \times \mathbf{B}$  drifts and equatorial electrojet exhibit a somewhat similar longitude and seasonal variability as the  $Sq$  current function at 12 LT. In particular, at equinox the daytime vertical  $\mathbf{E} \times \mathbf{B}$  drifts, equatorial electrojet, and  $Sq$  current function all exhibit maxima around  $\sim 0^\circ$ ,  $\sim 120^\circ$ , and  $\sim 280^\circ$  geographic longitude. However, the vertical drifts and equatorial electrojet also have a maximum near  $180^\circ$  geographic longitude that is not apparent in our results. The reason for this difference is not presently known. This difference may be related to the relative importance of different nonmigrating tides on introducing longitude variations in the low-latitude electric fields (which drive the vertical  $\mathbf{E} \times \mathbf{B}$  drift and equatorial electrojet) and the  $Sq$  current function. That is, a nonmigrating tide that introduces longitude variability in the low-latitude electric fields may have less influence on the  $Sq$  currents. Additionally, the influence of the geomagnetic main field for producing longitude variations in the  $Sq$  current function and low-latitude electric field may be different. Controlled numerical modeling experiments are necessary in order to fully understand the causes of these observed differences.

In order to further understanding of the seasonal and longitudinal variations, the amplitudes and phases of different longitudinal wavenumbers are presented as a function of day of year in

Figure 3.17. The phase is defined as the longitude of maximum (or one of multiple maxima when  $s > 1$ ) in the range of  $-60^\circ$  to  $300^\circ/s$ , where  $s$  is the longitudinal wavenumber. The longitudinal wavenumbers are calculated based on the average of the current function at 12 LT between  $15-45^\circ$  magnetic latitude in each hemisphere. Results for the Northern and Southern Hemisphere amplitudes are shown in Figures 3.17a and 3.17b, respectively, and Southern Hemisphere phases are presented in Figure 3.17c (Northern Hemisphere phases are similar and not shown). Note that due to our definition of maximum in the Southern Hemisphere, and how the phase is defined, the Southern Hemisphere phases presented in Figure 3.17c are actually the longitude of the minimum in the current function. Similar features are observed in both hemispheres and the predominant feature is the wave-1 longitude variation that is observed in both hemispheres throughout Northern Hemisphere summer. This feature is associated with the reduction in the current function between  $\sim 180-250^\circ$  geographic longitude that was previously discussed. The phase of the wave-1 structure also exhibits a pronounced seasonal variation and the phase shifts by  $\sim 240^\circ$  throughout the year. During the remainder of the year, there is not a clearly dominant longitudinal structure and a mixture of longitudinal wavenumbers is observed. However, we note that there is a slight preference towards a wavenumber-3 structure in longitude and this is most apparent during Northern Hemisphere winter. There is also a relatively large amplitude wavenumber-2 that occurs around the equinoxes in the Southern Hemisphere. A significant seasonal variation is also observed in the wavenumber-4 amplitude, particularly in the Northern Hemisphere. We further note that the phases of these features exhibit similar seasonal variations and are smoothly varying, indicating that these are not random features but are associated with a physical process. Aside from the wave-1 feature, the lack of a clearly dominant longitudinal wavenumber is thought to be related to the spacing between maxima. As noted previously, three distinct maxima are clearly observed in both hemispheres during September equinox (Figure 3.16c). However, the maxima are not separated by  $120^\circ$  in longitude and are thus not a purely wavenumber-3 structure in longitude. The lack of clearly dominant wave structures is thought to be related to the effect of nonmigrating tides generating various longitude structures combined with longitudinal structures that may be

introduced by the geomagnetic field and will be discussed in more detail later.

As demonstrated in Figures 3.15-3.17, there is considerable longitudinal variability in the  $Sq$  current function and we now turn our attention to discussion of the possible mechanisms for producing the observed variations. The structure and strength of the the  $Sq$  current system is primarily controlled by the ionospheric conductivity and tidal winds. We may therefore surmise that the longitudinal differences are, in some manner, related to variations in conductivity or tidal winds or some combination of the two. Matsushita [1967] proposed that since the conductivity is dependent upon the geomagnetic main field strength longitudinal variations in the geomagnetic main field strength may introduce longitudinal differences in the  $Sq$  current function. Modeling results have further confirmed that variable conductivities associated with geomagnetic field variations can induce longitudinal variations in field aligned currents that are related to longitudinal differences in the hemispheric asymmetry of the  $Sq$  current system [Stening, 1977]. We note that the observed minima around  $\sim 180^\circ$  geographic longitude in the  $Sq$  current function at 12 LT corresponds roughly with the region of enhanced geomagnetic field strength. The reduction of the peak in the daytime current function in this region may be related to the reduced conductivities associated with the enhanced geomagnetic field. However, the influence of reduced conductivities related to enhanced geomagnetic field strength should be minimal due to the fact that the dynamo generated currents are proportional to  $\mathbf{u} \times \mathbf{B}$ , where  $\mathbf{u}$  is the neutral wind and  $\mathbf{B}$  is the geomagnetic field [e.g., Richmond, 1989]. Thus, we may expect the reduction in conductivities due to enhanced geomagnetic field strength to be largely offset by the  $\mathbf{u} \times \mathbf{B}$  term in the equation for dynamo generation of currents. The geomagnetic field strength is therefore not thought to introduce significant longitudinal variability in the  $Sq$  current function. A second source of longitudinal variability associated with the geomagnetic field is the fact that the tidal wind system that drives the ionospheric wind dynamo is arranged in geographic coordinates while the ionospheric electric fields and currents are organized with respect to magnetic coordinates. As a result of this difference, the offset between the geographic and geomagnetic equators can introduce longitudinal variation in the  $Sq$  currents. Since the geomagnetic main field exhibits a primarily wave-1 variation in longitude, we consider

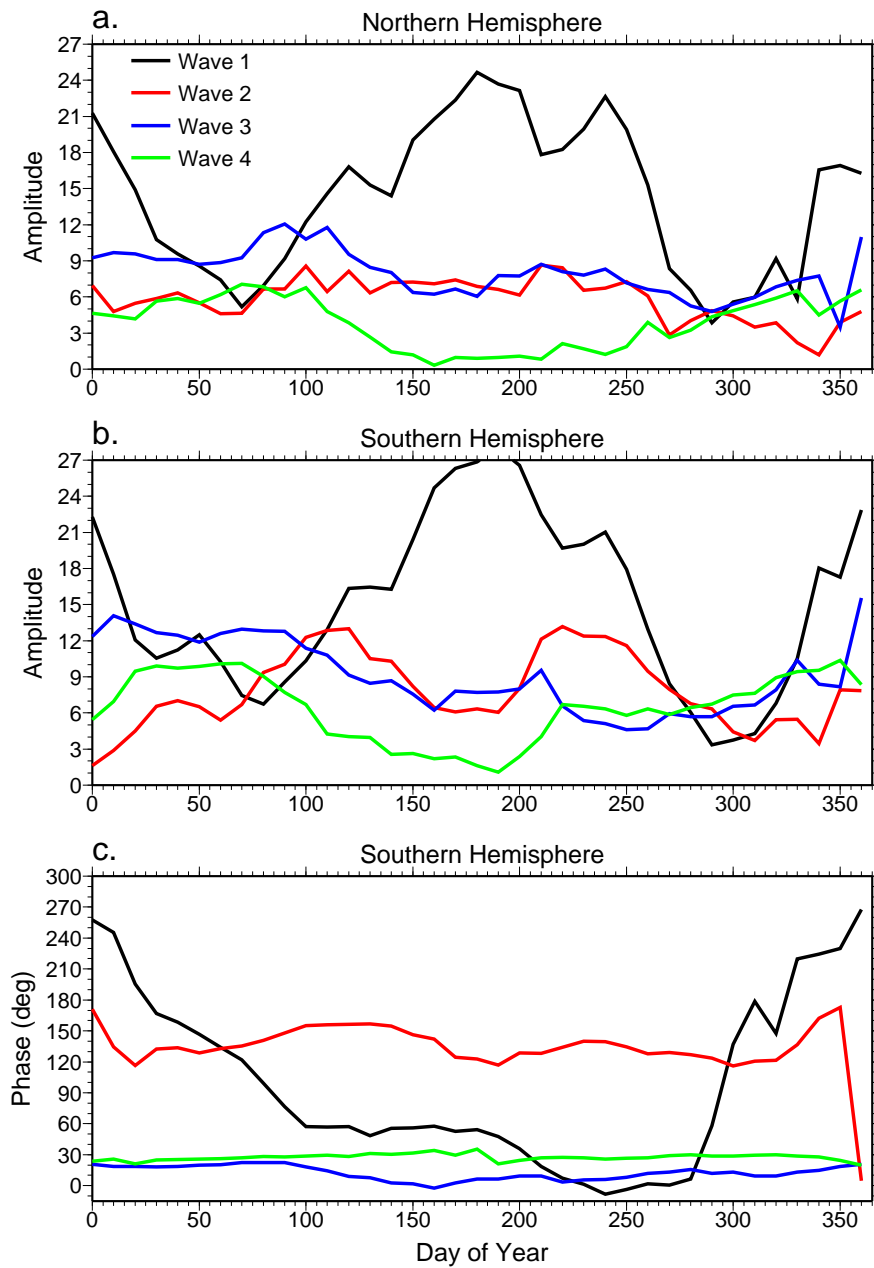


Figure 3.17: Seasonal variation for different longitudinal wavenumber amplitudes in the (a) Northern and (b) Southern Hemispheres. (c) Phases of the longitudinal wavenumbers in the Southern Hemisphere. The phase is defined as the longitude of maximum (or one of multiple maxima when  $s > 1$ ) in the range  $-60^\circ$  to  $300^\circ/s$ , where  $s$  is the longitudinal wavenumber. The wavenumbers are based on the average of the current function at 12 local time between  $15^\circ$  and  $45^\circ$  magnetic latitude in each hemisphere.

the observed wave-1 longitudinal structure in the  $Sq$  current function to be partly driven by the geomagnetic main field. The seasonal variation of the wave-1 longitude structure may be related to the seasonal variation of the tidal winds and the offset between the geomagnetic and geographic equators. However, this seasonal variation could also be related to the influence of nonmigrating tides as discussed below.

In addition to the influence of the geomagnetic field, tidal winds in the dynamo region will impact the generation  $Sq$  currents. In particular, the effect of nonmigrating tides, which at a fixed local time exhibit variations in longitude, should be considered as a mechanism for producing the observed longitudinal variations in the  $Sq$  current function. Observational and modeling studies have clearly demonstrated the influence that nonmigrating tides have on producing longitudinal variations in equatorial electric fields, ionospheric densities and thermospheric winds [e.g., England et al., 2006; Lin et al., 2007; Hagan et al., 2007; Häusler et al., 2010]. It is, therefore, reasonable to presume that nonmigrating tides may play a significant role in producing longitudinal differences in the  $Sq$  current function. The wave-1 longitudinal structure in the  $Sq$  current function at 12 LT that maximizes during Northern Hemisphere summer may be related to the diurnal tide with zonal wavenumber-0 ( $D0$ ). We consider  $D0$  as a potential source of the wave-1 feature owing to the fact that it achieves large amplitudes in Northern Hemisphere summer [Forbes et al., 2003; Oberheide et al., 2006] and also since it appears as a wave-1 structure in longitude when viewed at a fixed local time. However,  $D0$  is not symmetric about the equator [e.g., Forbes et al., 2008] and modeling studies have demonstrated that symmetric tidal modes primarily establish the  $Sq$  current systems [Stening, 1969; Richmond et al., 1976]. Despite the dominance of symmetric modes, antisymmetric tidal winds still may play a role in modulating the global  $Sq$  current system [Stening, 1989]. This is particularly true during solstice conditions when, as a result of the seasonal variation of insolation, the conductivities are hemispherically asymmetric. Given that the seasonal variations of  $D0$  match those of the wave-1 longitude variation in the  $Sq$  current function, we believe this to be a plausible mechanism for producing the observed wave-1 feature and its seasonal variation.

In addition to the predominant wave-1 longitudinal structure, other longitudinal structures

are observed in Figures 3.16 and 3.17 and may be related to the influence of nonmigrating tidal winds and/or the geomagnetic main field. Based only on our limited observations, it is difficult to clearly specify which nonmigrating tides may be responsible for introducing much of the longitudinal variability in the  $Sq$  current function. This is largely due to the fact that there is not a clearly dominant longitudinal structure aside from the wave-1 feature. It is likely that nonmigrating tides that produce different longitudinal variations along with the variations due to the geomagnetic main field combine in a manner such that a single longitude structure is not discernible. It is, however, clearly apparent from Figure 3.16 that significant longitudinal variability is present in the  $Sq$  current function and additional studies are necessitated to elucidate the role of various nonmigrating tides as well as the geomagnetic main field on producing these variations.

#### 3.4.4 Conclusions

A detailed description of the longitudinal and seasonal variation of the global  $Sq$  current system during solar minimum conditions is laid forth in the present section. This has only been made possible by the use of satellite magnetic field observations to determine the  $Sq$  current function which affords unprecedented spatial coverage. A primarily wave-1 feature in longitude in the  $Sq$  current function at 12 LT is observed and exhibits large amplitudes during Northern Hemisphere summer. This longitudinal variation is attributed to the  $D0$  nonmigrating tide and also the geomagnetic main field. The main geomagnetic field can introduce longitudinal variability due to conductivity differences and also due to the offset between the geographic and geomagnetic equators. Other longitudinal variations are also apparent; however, they do not exhibit a discernible longitudinal wavenumber. The lack of a dominant longitudinal structure may be related to the combined effect of longitudinal variations associated with various nonmigrating tides and those related to the geomagnetic main field.

The exact cause of the longitudinal variations in the  $Sq$  current system remains an open question. Our results and prior modeling studies clearly demonstrate that the geomagnetic field plays a key role in generating longitudinal inequalities in the  $Sq$  current system. However, our

results suggest additional longitudinal variability that may not be related to the geomagnetic field and these variations are thought to be related to the influence of nonmigrating tides. Controlled numerical modeling experiments are necessary in order to understand the role that various non-migrating tides and the geomagnetic main field play in generating these longitudinal variations. Lastly, it is important to recognize the fact that the results presented herein are representative of solar minimum conditions and different longitudinal and seasonal variations may be present at solar maximum.

## Chapter 4

### Influence of planetary waves on the low-latitude ionosphere

The present chapter is concerned with the influence of planetary wave activity on the ionosphere. In particular, the focus is on temporal variations in the low-latitude ionosphere during periods of enhanced middle-atmosphere planetary wave activity. A discussion of planetary waves and their influence on the ionosphere was presented in Section 1.2, and is not repeated herein. Despite the previously discussed works concerning planetary waves and their ionospheric impact, this remains a relatively unexplored area of research, and thus has many open questions. Due to a historical sparseness of observations, past studies of the ionospheric impact of planetary waves have been limited in scope to either a single location, or only a handful of observing sites [e.g., Chen, 1992; Forbes and Leveroni, 1992; Yi and Chen, 1993; Pancheva et al., 2006; Vineeth et al., 2007].

Although these past studies have elucidated features of the ionospheric response to planetary wave activity, they lack a global context. The recent increases in satellite observations combined with the recent development of an extensive network of ground based GPS observations present the opportunity to now study temporal variations in the ionosphere due to planetary wave activity in a global sense. Developing an understanding of the impact of planetary waves on the global ionosphere is the objective of the present chapter. This is done through two observational studies. First, in section 4.1 the global response of the ionosphere to the quasi-16 day planetary wave is investigated. Recent observations [e.g., Goncharenko and Zhang, 2008; Chau et al., 2009] have also demonstrated a connection between sudden stratospheric warmings and the low-latitude ionosphere. This connection is further explored in section 4.2, where the perturbations to the low-

latitude ionosphere during sudden stratospheric warmings are presented in the context of nonlinear interaction between tides and planetary waves. Each of the following sections first provides a brief introduction and discussion of the present problem. An overview of the data analysis is then provided followed by presentation of the results and a discussion. Lastly, each section concludes by summarizing the results.

## **4.1 Modulation of the Equatorial F-Region by the Quasi-16-day Planetary Wave**

### **4.1.1 Introduction**

Oscillations at planetary wave periods in the EIA have been linked to changes in E-region winds which, through the dynamo mechanism, create oscillations in the strength of the equatorial electric field [Chen, 1992; Forbes and Leveroni, 1992]. The effect of planetary waves on the low-latitude F-region ionosphere has typically been studied using either a single ground-based location or a chain of stations at a fixed longitude [Chen, 1992; Forbes and Leveroni, 1992; Yi and Chen, 1993]. The latitudinal and longitudinal extent to which planetary waves influence the low-latitude ionosphere is therefore less well studied. At mid-latitudes, the quasi-16-day oscillation is typically a global scale phenomena, while shorter period planetary waves are more limited in longitude [Altadill and Apostolov, 2003; Lastovicka et al., 2006]. Using TEC observations at mid-latitudes, Borries et al. [2007] found planetary wave periodicities to be most dominant in the zonal mean. However, these periodicities were attributed to periodic geomagnetic disturbances as opposed to vertically-propagating waves. Vineeth et al. [2007] recently demonstrated that the occurrence of quasi-16-day oscillations in mesospheric winds during December 2005 - March 2006 were linked to similar periodicities in the equatorial electrojet (EEJ). Due to the close relationship between EEJ electric fields and those driving the EIA, one might expect that quasi-16-day variations also occurred in the F-region ionosphere during this period. The question is, what are the magnitude and global extent of these F-region effects?

The objective of the present study is thus to examine the extent to which the quasi-16-day planetary wave influences the low-latitude F-region. We use in situ electron density measurements from the CHAMP satellite and ground based GPS TEC to demonstrate that the quasi-16-day oscillation during the time period of December 2005 to March 2006 influenced the zonal mean F-region ionosphere. (It was presumed by Vineeth et al. [2007] that the quasi-16-day oscillation penetrated into the 100-170 km dynamo region in order to modulate the EEJ electric field). We also utilize TIMED/SABER temperature data to verify that a quasi-16-day periodicity existed within the dynamo region during this period. Additionally, the local time dependence of the planetary wave effect is explored.

#### 4.1.2 Data and Methods

In order to observe the effect of planetary wave activity in the dynamo region we analyze SABER temperature data. The SABER temperature data consists of residuals from the tidal fits that are presented in Forbes et al. [2008]. These residuals are spectrally analyzed with respect to time and longitude, and average amplitudes calculated within the 12-18 day period range are used to provide a measure of the strength for the quasi-16-day wave for longitudinal wavenumbers  $s = 0, 1, 2$  and  $3$ .

The Planar Langmuir Probe onboard CHAMP provides in situ electron density measurements at 15-second intervals ( $\sim 120$  km. in-track distance). The electron density measurements are at a near constant height and thus are sensitive to changes in the F-layer peak height. During late 2005 and early 2006 the equatorial height of CHAMP was around 345 km.. There is also an approximately 10 km. change in altitude between  $-30^\circ$  and  $+30^\circ$  latitude which may introduce a slight hemispheric asymmetry. Despite these challenges, CHAMP measurements of electron density are advantageous due to its near-polar, Sun-synchronous orbit that precesses in local time at the rate of  $\sim 5.44$  minutes per day. This means that CHAMP samples 15-16 different longitudes per day giving a global view of the ionosphere. The changing local time of the measurements introduces a trend in the data when an extended time period is considered. To eliminate this trend a cubic

polynomial is fit to daily zonal mean electron densities and we analyze the residuals to determine the effect of planetary wave activity.

To complement the CHAMP in situ electron density observations, TEC measurements at a fixed local time are also analyzed. The TEC measurements come from the International GNSS Service (IGS) global ionosphere maps (GIMs) [Dow et al., 2005]. The GIMs are obtained from a global network of GPS receivers and have a temporal resolution of 2 hours and spatial resolution of  $5^\circ$  in longitude and  $2.5^\circ$  in latitude. The TEC observations at a fixed local time are analyzed in an identical manner to the CHAMP electron densities.

### 4.1.3 Results and Discussion

Average SABER temperature amplitudes at 110 km for 12-18 day periods and zonal wavenumbers  $s = 0$  and  $s = 1$ , from 1 December 2005 to 31 March 2006, are shown in Figure 4.1. The SABER temperature amplitudes exhibit a general intensification of activity during January and February 2006, similar to the interval of time identified by Vineeth et al. [2007]. The enhancements are much more prominent in the  $s = 0$  component as opposed to  $s = 1$ , and are not seen in  $s = 2$  and  $s = 3$  (not shown). This demonstrates that in the dynamo region all longitudes appear to be equally influenced by the planetary wave oscillation.

Connections between temperature perturbations in the E-region and electron densities in the F-region have previously been hypothesized through changes in the strength of the dynamo-generated electric fields thought to be generated by the accompanying wind fields [England et al., 2006; Immel et al., 2006]. Given the quasi-16-day oscillations in SABER zonal mean temperatures at 110 km, we expect similar periodicities to be present in the low-latitude F-region ionosphere. Lomb-Scargle periodogram [Lomb, 1976; Scargle, 1982] analyses presented in Figure 4.2 indeed reveals quasi-16-day periodicities in CHAMP electron densities and TEC. Significant differences are apparent in the strength of the quasi-16-day periodicity between the magnetic equator and  $15^\circ$  magnetic latitude and between daytime and nighttime which will be discussed later. Figures 4.2a and 4.2b also reveal elevated power within the 12-18 day period band in  $K_p$  and SOHO 0.1-

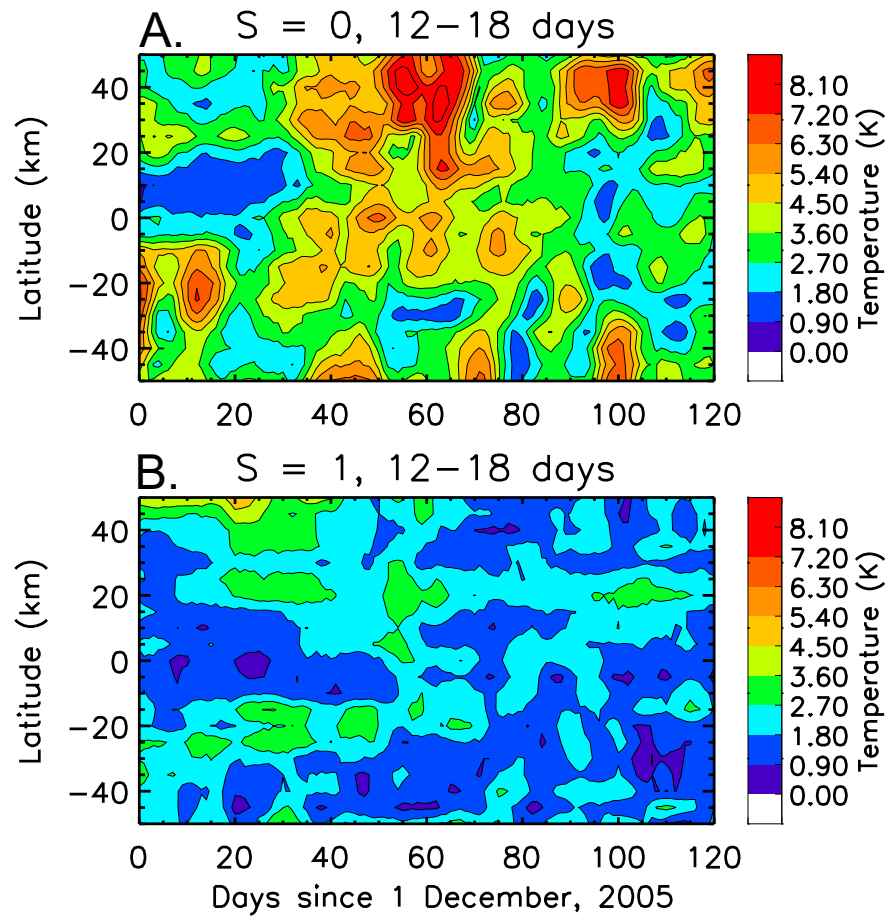


Figure 4.1: (a)  $s = 0$  and (b)  $s = 1$  SABER temperature average amplitudes with 12–18 day periods at 110 km.

50 nm EUV flux, respectively. A larger peak in  $K_p$  is observed at 9-days which is attributed to periodic forcing due to solar wind high-speed streams during late 2005 and early 2006 [Thayer et al., 2008]. The 9-day period in  $K_p$  is stronger than the peak near 16-days, while the opposite is true in electron densities and TEC. Energy near quasi-16-day periods is also observed in SOHO EUV measurements. We have compared the 27-day oscillations in SOHO EUV and daytime CHAMP electron densities and established a linear relationship between the two. Applying this relationship to the quasi-16-day oscillation, the EUV flux variability is not able to account for the corresponding variability in electron density. We therefore conclude that the quasi-16-day oscillations observed in the ionosphere are due to coupling with the lower atmosphere and not recurrent geomagnetic activity or solar flux variability.

We now turn our attention to the temporal and local time response of the low-latitude ionosphere. Raw and residual CHAMP electron densities for the descending portion of the orbit are given in Figures 4.3a and 4.3b, respectively. To emphasize the quasi-16-day periodicity, a bandpass filter centered at 15 days with half-power points at 12 and 18 days is applied. The bandpass-filtered residuals are shown in Figures 4.3c and 4.3d for the descending (daytime) and ascending (nighttime) portions of the orbit. Enhancements in the EIA crests that are greater than 45% of the cubic polynomial removed from the data are observed in the daytime around days 31-33, 46-48, and 60-62. These enhancements are associated with 15-20% decreases in the equatorial electron density. During these same time periods, 15-20% decreases are also observed in the nighttime electron densities between  $-15^\circ$  and  $+15^\circ$  magnetic latitude. The timing of these enhancements is similar to the enhancements observed in the SABER planetary-wave-period temperature amplitudes with the exception of the peak in electron density at days 31-33 which may be due to differences in local time between the measurements. This does, however, demonstrate that the enhancements in temperature observed in the dynamo region are likely connected with changes in the strength of the electric field which creates the changes in the strength of the EIA observed by the CHAMP satellite.

The CHAMP observations are at a near constant height and the oscillations in the EIA could

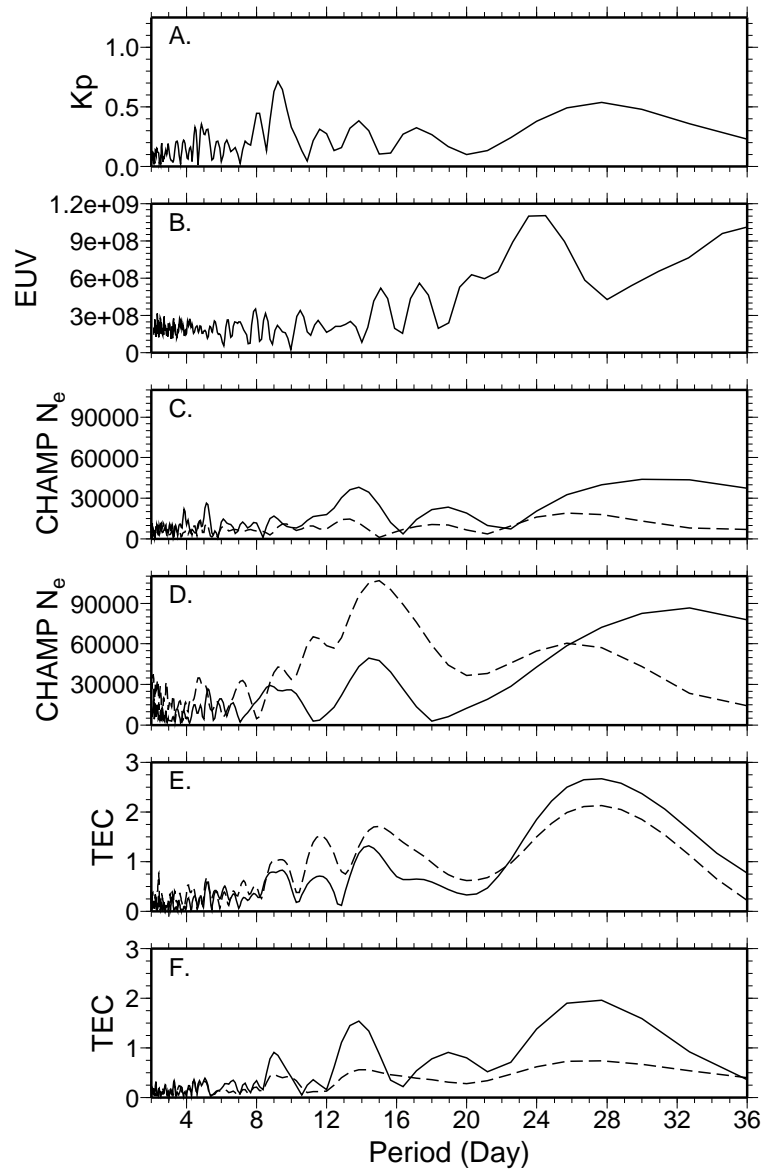


Figure 4.2: Lomb-Scargle periodograms during the time period of 1 Dec. 2005 - 1 Mar. 2006. (a) Kp (b) SOHO EUV flux in 0.1-50nm (c) CHAMP in situ electron density for ascending portion of the orbit at the magnetic equator (solid) and  $15^\circ$  magnetic latitude (dashed) (d) same as (c) except for the descending portion of the orbit (e) TEC at 10 LT at the magnetic equator (solid) and  $15^\circ$  magnetic latitude (dashed) (f) same as (e) except for 22 LT

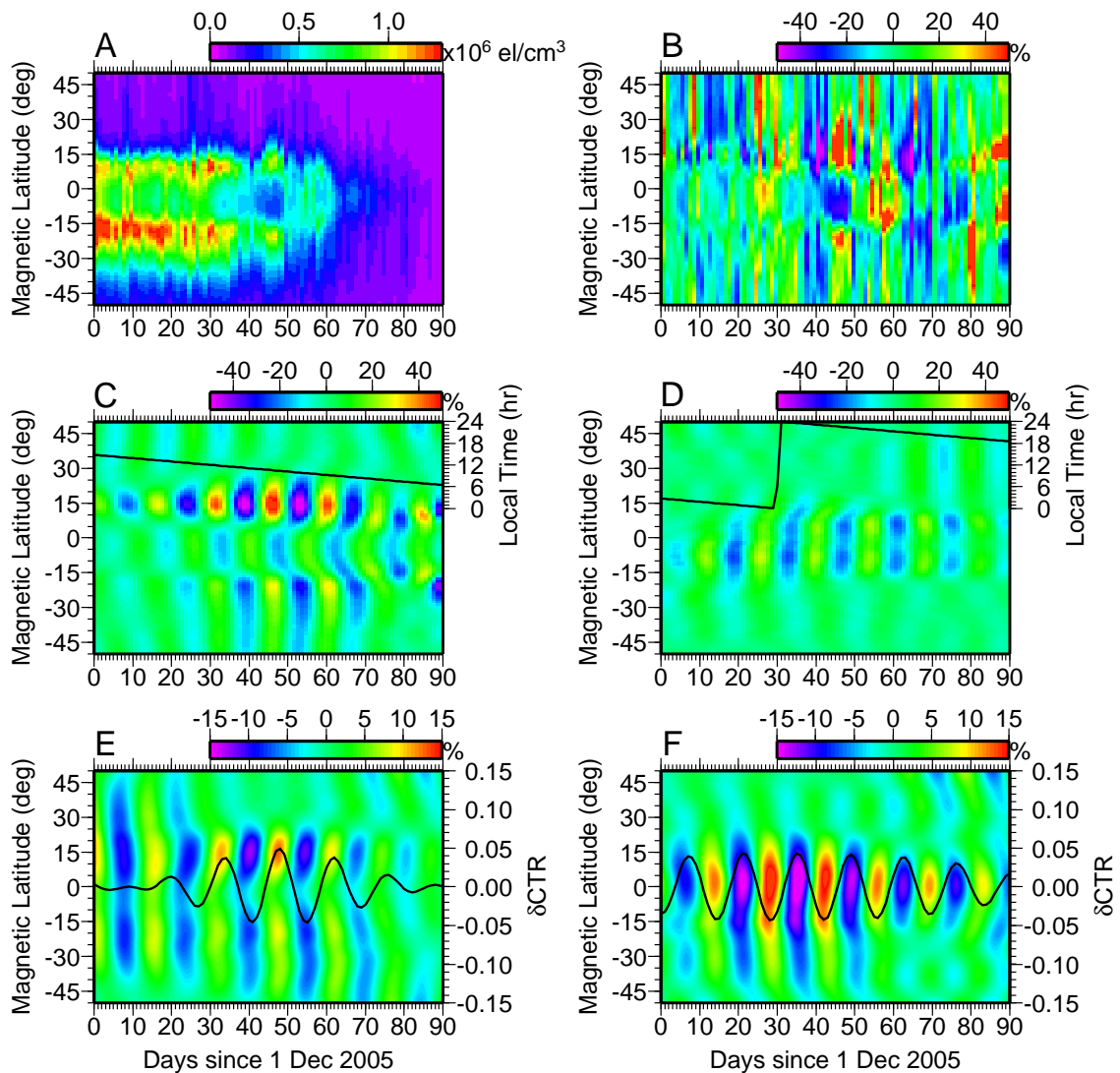


Figure 4.3: (a) Zonal-mean CHAMP in situ electron densities for the descending portion of the orbit prior to the removal of a cubic polynomial. (b) Electron density residuals for the descending portion of the orbit expressed as a percentage of the trend. (c) Bandpass-filtered electron density residuals for the descending portion of the orbit expressed as a percentage of the trend. The LT of equatorial crossing is overlaid. (d) Same as (c) except for the ascending portion of the orbit. (e) Bandpass filtered TEC and CTR at 10 LT. Filtered TEC is expressed as a percentage of the cubic polynomial that was removed. (f) Same as (e) except for at 22 LT.

be the result of only changes in the F-layer peak height. We have analyzed GPS TEC measurements in order to demonstrate how the planetary wave activity influences the ionosphere in an integrated sense and to examine the response at fixed local times. Bandpass-filtered TEC at 10 LT and 22 LT are shown in Figures 4.3e and 4.3f, respectively. We have also overlaid the bandpass-filtered crest-to-trough ratio (CTR) which provides a means of assessing the strength of the EIA [Mendillo et al., 2000]. The bandpass filtered CTR shows that changes in the strength of the EIA at quasi-16-day periods occurs during the time period when similar periodicities were observed in SABER zonal mean temperatures and CHAMP electron densities. The enhancements observed in TEC during this time period are only 15% of the background level, which is significantly smaller than in electron density at a near-constant height. In the anomaly crest regions at  $\pm 10\text{-}20^\circ$  magnetic latitude, a significant local time effect is observed. At these latitudes, daytime TEC increases are nearly inphase with nighttime decreases in TEC. We have looked at other local time pairs and observed similar anti-correlation between daytime and nighttime TEC oscillations.

Given the similarity between the quasi-16-day period and the  $\sim 14$ -day period of the lunar semidiurnal tide, it is possible that the lunar tide influences our results. This is true especially since the lunar tide in the ionosphere maximizes during Northern Hemisphere winter [e.g., Rastogi et al., 1985; Stening and Fejer, 2001]. However, we do not believe that significant aliasing is present for several reasons. First, the observation reveal only a short term enhancement at a period near 16-days which is consistent with the short-lived nature of the quasi-16-day planetary wave. Further, the expected enhancement in the GPS TEC due to the lunar semidiurnal tide is  $\sim 5\%$  [Pedatella and Forbes, 2010], which is significantly less than the enhancements that we have observed in connection with the quasi-16-day planetary wave.

One feature that is particularly interesting is the larger oscillations in nighttime TEC compared to daytime TEC. This is opposite to what is observed in CHAMP electron densities, where the daytime enhancements were significantly greater than those at night. Vineeth et al. [2007] observed quasi-16-day enhancements in the strength of the counter electrojet (CEJ) during this time period and this may be related to the difference between TEC and CHAMP observations.

The days with enhanced CEJ will produce greater downward  $\mathbf{E} \times \mathbf{B}$  drift during the evening hours. Downward drifts will increase the loss rate, generating the periodic decreases that are observed in TEC. The difference between the strength of the daytime and nighttime TEC oscillations may be due to the relative strength of the EEJ/CEJ as well as the smaller background TEC levels at night. The increased downward drifts associated with the CEJ will also suppress the height of the F-layer. This will alter the height of the electron density observations with respect to the F-region peak and is thought to be responsible for producing the smaller nighttime modulations in CHAMP electron densities compared to the daytime.

#### 4.1.4 Conclusions

The results presented provide insight into the extent to which planetary waves may influence the low-latitude ionosphere. Whereas previous analyses have focused on a single longitude [e.g., Chen, 1992; Forbes and Leveroni, 1992; Vineeth et al., 2007], we have demonstrated that at low-latitudes the quasi-16-day planetary wave appears to be a global phenomena that influences the ionosphere at all longitudes in a similar manner. This is consistent with the longitudinal extent of the quasi-16-day planetary wave influence on F-region electron densities at mid-latitudes [Altadill and Apostolov, 2003; Lastovicka et al., 2006]. Quasi-16-day enhancements in zonal mean temperature in the dynamo region are connected with similar oscillations in the strength of the EIA, further demonstrating the strong coupling between the lower-atmosphere and the ionosphere. At a constant height, these oscillations are significant and reach 45% of the background electron density. There is also a significant local time effect with the planetary wave activity producing daytime enhancements and nighttime decreases in the EIA crest region.

In the present analysis we have explored the effect of quasi-16-day oscillations during the time period of 1 December 2005 to 1 March 2006. As we have only studied a single event, it is unclear whether the features we have observed are a consistent feature of how planetary waves influence the low-latitude ionosphere. Moreover, we have only examined the effect of the quasi-16-day wave and whether or not planetary waves of other periodicities exhibit similar characteristics is

unclear. Shorter period planetary waves may influence the low-latitude ionosphere on a less global scale [Altadill and Apostolov, 2003; Lastovicka et al., 2006]. A detailed analysis of the longitudinal extent that planetary waves of different periods influence the low-latitude F-region ionosphere is necessary in order to improve our understanding of how vertically propagating waves influence the low-latitude ionosphere.

## **4.2 Evidence for Stratosphere Sudden Warming-Ionosphere Coupling due to Vertically Propagating Tides**

### **4.2.1 Introduction**

Sudden stratospheric warmings (SSWs) are associated with rapid alterations of temperature, wind, and circulation in the polar winter middle atmosphere. The atmospheric effects of SSWs have been extensively studied [see reviews by Schoeberl, 1978; Holton, 1980, and references therein] and the mechanism for their generation is understood to be the interaction between the zonal mean flow and the growth of vertically propagating planetary waves [Matsuno, 1971]. Although the most dramatic effects are observed in the stratosphere, SSWs also influence higher altitudes. Observations and theoretical modeling demonstrate mesosphere cooling as well as warming in the lower thermosphere during SSWs [e.g., Cho et al., 2004; Liu and Roble, 2002].

It is well known that vertically propagating waves from the lower-atmosphere can induce significant day-to-day and week-to-week variability in the ionosphere [Forbes et al., 2000; Lastovicka, 2006]. Recent observations also demonstrate a strong connection between SSWs and pronounced changes in the mid and low-latitude ionosphere [Goncharenko and Zhang, 2008; Chau et al., 2009; Sridharan et al., 2009]. While the mechanisms by which atmospheric tides and planetary waves influence the ionosphere are generally well understood, the processes responsible for generating ionospheric variability in connection with SSWs remain unclear. Both Goncharenko and Zhang [2008] and Chau et al. [2009] observed a primarily semidiurnal modulation of the ionosphere during the 2008 SSW and suggested that enhanced planetary wave activity associated with SSWs have

a significant role in generating the ionospheric perturbations. Conversely, Fejer et al. [2010] suggested that semidiurnal perturbations in the equatorial electrojet (EEJ) during SSWs are related to enhanced lunar tides. It was recently proposed that the observed semidiurnal perturbations in the ionosphere are due to the nonlinear interaction between migrating tides and planetary waves [Sridharan et al., 2009; Liu et al., 2010]. Modeling results by Liu et al. [2010] demonstrate that although the planetary wave activity associated with SSWs is concentrated at high-latitudes, the nonlinear interaction between tides and the quasi-stationary planetary wave enhances migrating and nonmigrating tides globally. Furthermore, significant changes in the tidal winds were found to occur in the low-latitude E-region where electric fields are generated by the dynamo mechanism, resulting in modulation of the vertical drift velocity and electron densities in the ionosphere. During the 2002 Southern Hemisphere SSW this nonlinear interaction mechanism produced a large nonmigrating westward propagating semidiurnal tide with zonal wavenumber-1 in the MLT region as revealed in both numerical modeling and observations [Chang et al., 2009]. Enhanced nonmigrating tides associated with the nonlinear interaction between planetary waves and migrating tides were also observed in stratosphere and lower mesosphere temperatures during the 2003/2004 SSW [Pancheva et al., 2009].

Although it has been suggested that the nonlinear interaction between tides and planetary waves couples SSWs to ionospheric variability, there is a lack of observational evidence that clearly demonstrates the modulation of migrating *and* nonmigrating tides in the ionosphere during SSWs. In the present study we use ground based GPS TEC observations to present the first observational evidence of changes in ionospheric migrating *and* nonmigrating semidiurnal tides in the low-latitude ionosphere during the 2009 SSW. The 2009 SSW presents unique conditions in that it was particularly strong and long-lasting. It also occurred during a prolonged solar minimum period, providing ideal conditions for studying vertical coupling between different atmospheric regions and we have thus focused on this event.

### 4.2.2 Data and Methods

The GPS TEC observations are from the IGS GIMs (<http://igsceb.jpl.nasa.gov>). The GIMs analyzed have a temporal resolution of 2 h and a spatial resolution of  $2.5^\circ$  in latitude and  $5^\circ$  in longitude. In certain regions, the distribution of GPS receivers used to produce the GIMs is sparse and a certain amount of smoothing is entailed in order to obtain a global map. The procedure used to generate the GIMs aims to minimize the effect of limited GPS observations and they are in reasonably good agreement with independent measurements over the ocean where GPS observations are scarce [e.g., Mannucci et al., 1998]. Although the GIMs are not a raw observation and are influenced by the receiver distribution, we believe that the GIMs generally represent the spatial and temporal variations in the ionosphere during periods of quiet geomagnetic activity and the global distribution that they afford makes them well-suited for the present study.

To elucidate the effect of the 2009 SSW on the ionosphere the GPS TEC are analyzed in terms of their various migrating and nonmigrating tidal components. Analogous to the study of solar atmospheric tides, [e.g., Zhang et al., 2006] the observations are least-squares fit to an equation of the form

$$A_{n,s} \cos(n\Omega t_{LT} + (s - n)\lambda - \phi_{n,s}) \quad (4.1)$$

where  $n$  denotes a subharmonic of a solar day,  $\Omega$  the rotation rate of the Earth ( $2\pi \text{ day}^{-1}$ ),  $t_{LT}$  the local time,  $s$  the zonal wavenumber (positive for westward propagation),  $\lambda$  the longitude, and  $A_{n,s}$  and  $\phi_{n,s}$  are the amplitude and phase, respectively, of the different tidal components. The  $n=1, 2, 3$  components are referred to as diurnal, semidiurnal, and terdiurnal tides, respectively. The fit is performed for  $n = 0, 1, \dots, 4$  and  $s = -5, -4, \dots, 4, 5$  within  $2.5^\circ$  magnetic latitude bins and we thus obtain a full spectrum of migrating ( $n = s$ ) and nonmigrating ( $n \neq s$ ) tidal components for a range of latitudes.

### 4.2.3 Results and Discussion

The GPS TEC observations for the  $n=0$   $s=0$ ,  $n=2$   $s=1$  (westward propagating semidiurnal tide with zonal wavenumber 1, *SW1*), and  $n=2$   $s=2$  (migrating semidiurnal tide, *SW2*) tidal components are presented in Figure 4.4 along with the geomagnetic activity index,  $K_p$ , and the NCEP reanalysis (<http://www.esrl.noaa.gov/psd/>) temperature at  $90^\circ\text{N}$  and 10hPa and the zonal mean zonal wind at  $60^\circ\text{N}$  and 10hPa. The NCEP temperature peaks around day 24 and at this same time the zonal mean zonal wind reverses direction indicating that the 2009 SSW was a major warming event. During this same time period, there is also significant variability in the GPS TEC semidiurnal tides. As can be seen in Figure 4.4a, early 2009 was generally quiet in terms of geomagnetic activity. However, there is still moderate variability in  $K_p$  which will perturb the GPS TEC. It is important to consider the possibility that some of the observed perturbations in the ionosphere are the result of geomagnetic variations and not solely related to the SSW. From Figure 4.4 it is apparent that the perturbations in  $n=0$   $s=0$  (Figure 4.4a) are closely related to the variations in  $K_p$  while the semidiurnal tidal components (Figures 4.4b and 4.4c) do not exhibit any clear correlation with geomagnetic activity. We thus conclude that the large semidiurnal variations are related to the SSW which is consistent with semidiurnal ionospheric perturbations observed during the 2008 SSW [Chau et al., 2009; Goncharenko and Zhang, 2008]. Additionally, the variations in GPS TEC are concentrated in the EIA crest region, indicating that these perturbations are associated with changes in dynamo-generated electric fields and the EEJ strength during the SSW [Chau et al., 2009; Fejer et al., 2010]. A decrease in the  $n=0$   $s=0$  component also occurs around the peak of the SSW. In addition to the effect of decreased geomagnetic activity during this time period, this decrease may, in part, be related to planetary wave activity preceding the SSW, as described below.

Having demonstrated that the semidiurnal tides in the low-latitude ionosphere are significantly perturbed during the 2009 SSW, we now turn our attention to the coupling between the SSW and the ionospheric variations. It has previously been suggested [e.g., Sridharan et al., 2009; Liu et

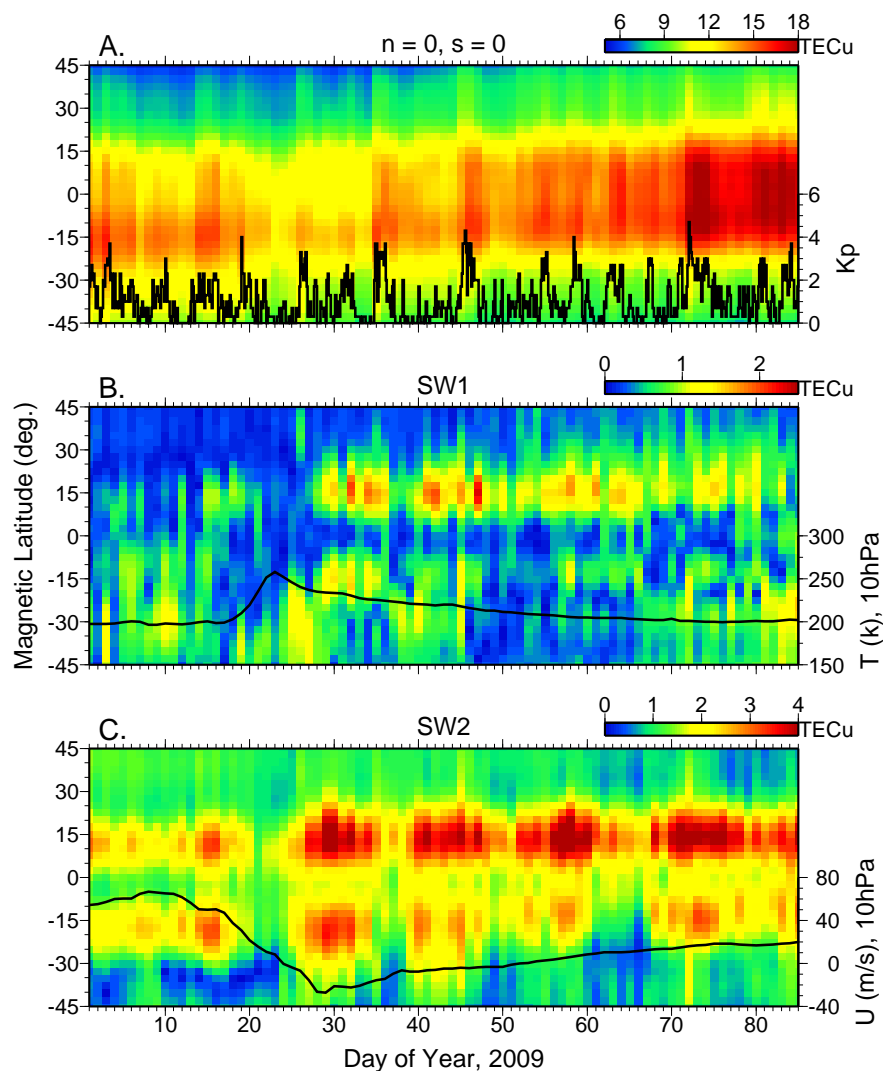


Figure 4.4: GPS TEC observations during the 2009 SSW for tidal components  $n=0$   $s=0$  (A), the westward propagating nonmigrating semidiurnal tide with zonal wavenumber 1,  $SW1$  (B) and the migrating semidiurnal tide,  $SW2$  (C). The  $K_p$  index is overlaid in A. NCEP reanalysis temperature at  $90^\circ\text{N}$  and zonal mean zonal wind at  $60^\circ\text{N}$  are overlaid in B and C, respectively.

al., 2010] that this connection results from the nonlinear interaction between atmospheric tides and planetary waves. Modeling results by Liu et al. [2010] strongly support this mechanism and they demonstrate that planetary wave-1 (PW1) activity at Northern Hemisphere high-latitudes perturbs atmospheric tides globally. In particular, Liu et al. [2010] present an intensification of *SW1* and *SW2* in the low-latitude E-region neutral winds where they may modulate the EEJ strength. Enhancements in *SW1* and *SW2* are also observed in GPS TEC during the 2009 SSW (Figures 4.4b and 4.4c). To further demonstrate the connection between the SSW and changes in *SW1* in the ionosphere, Figure 4.5a shows the PW1 amplitude of geopotential height at 60°N and 10hPa and *SW1* at 15°N geomagnetic latitude from the GPS TEC. The GPS TEC observations are shifted by 5 days to account for time delay and aid in the comparison. Between days 25 and 55, both the PW1 amplitude and *SW1* amplitude display similar variations and oscillate with a period of 12-16 days, further suggesting a physical connection. The ~5 day delay between the PW1 activity at 10hPa and the ionospheric signature is attributed to a combination of propagation time and also the time required for the global tide to adjust to changes in the forcing [Vial et al., 1991]. Although the physical connection between PW1 and *SW1* may not be immediately apparent, Angelats i Coll and Forbes [2002] demonstrate that the nonlinear interaction between PW1 and *SW2* generates *SW1* and *SW3* (westward propagating semidiurnal tide with zonal wavenumber 3). The similarity in the oscillations in PW1 and *SW1* provides strong observational evidence that the nonlinear interaction between tides and planetary waves occurs during SSWs, and furthermore, that global tidal modulation due to planetary waves is the driving mechanism for ionospheric perturbations during SSWs. Although this nonlinear interaction may also enhance *SW3*, this is not observed during the 2009 SSW. Similar oscillations to those in *SW1* are also observed in *SW2* (Figure 4.4c) and are thought to be related to changes in the mean flow conditions associated with the planetary wave forcing. The enhancement in *SW2* does, however, remain large up to and beyond day 85 and this will be discussed in more detail later.

The PW1 activity that occurred during the 2009 SSW was relatively weak at stratospheric altitudes and was preceded by large planetary wave-2 (PW2) amplitudes in the high-latitude North-

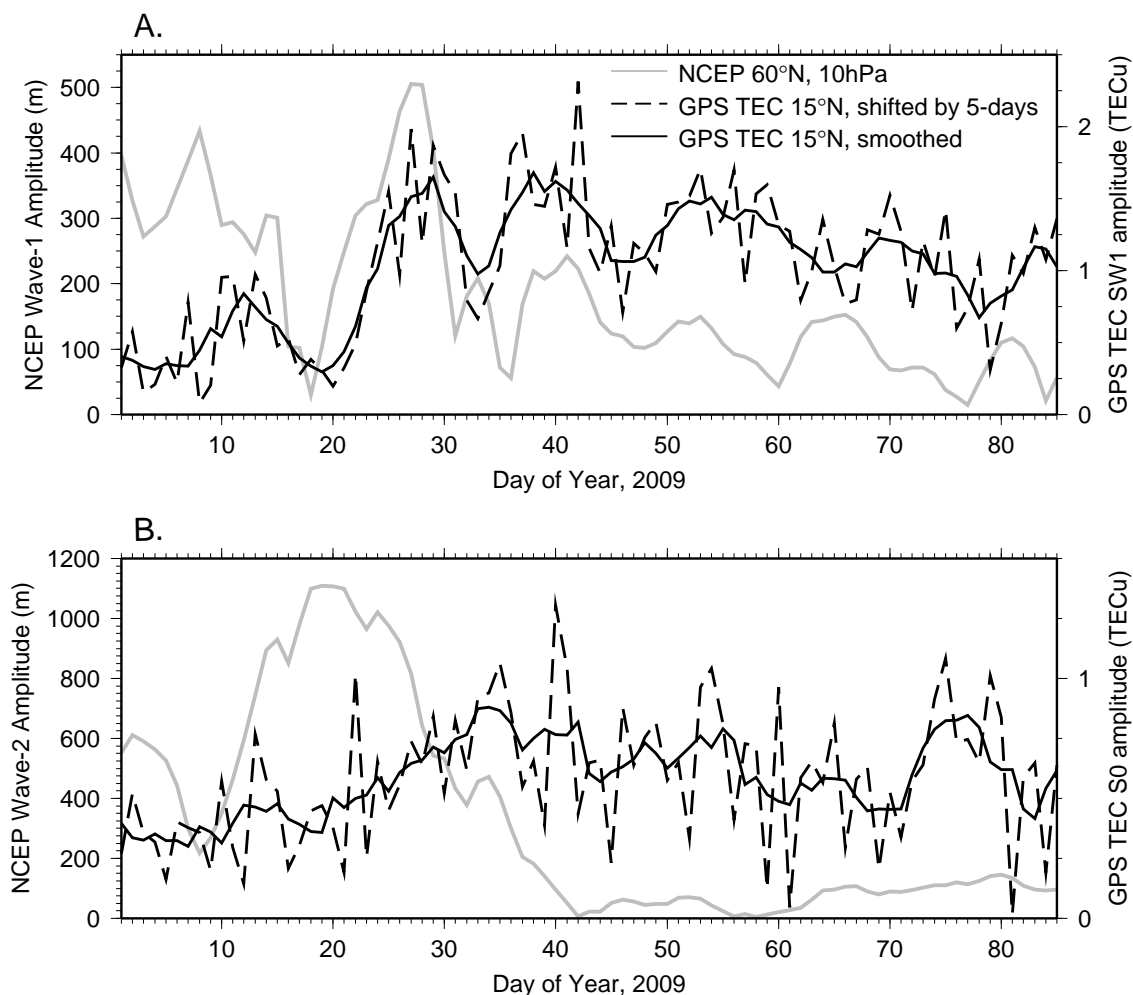


Figure 4.5: (A) NCEP planetary wave-1 amplitude of geopotential height at  $60^\circ\text{N}$  and 10hPa. The SW1 (westward propagating nonmigrating semidiurnal tide with zonal wavenumber 1) component of GPS TEC at  $15^\circ\text{N}$  geomagnetic latitude is also shown and is shifted by 5-days. (B) Same as (A) except for planetary wave-2 and S0 (nonmigrating semidiurnal tide with zonal wavenumber 0).

ern Hemisphere stratosphere. Similar to PW1, PW2 may interact nonlinearly with the migrating semidiurnal tide, generating the nonmigrating semidiurnal tides with zonal wavenumber 0 ( $S0$ ) and westward propagating with zonal wavenumber 4 ( $SW4$ ). Supposing the above mechanism of planetary wave-tide interaction is responsible for perturbing the ionosphere during SSWs, we may therefore expect to observe similar enhancements in PW2 and  $S0$  and/or  $SW4$ . Figure 4.5b presents PW2 activity in geopotential height at  $60^\circ\text{N}$  and 10hPa and  $S0$  from the GPS TEC at  $15^\circ$  geomagnetic latitude (no significant perturbation is observed in  $SW4$ ). The PW2 activity peaks around day 20 and then slowly decays.  $S0$  begins to slowly grow beginning around day 20, peaks near day 35 and, similar to  $SW2$  and  $SW1$ , remains elevated for an extended time period.

If the nonlinear interaction between planetary waves and tides is the primary mechanism which couples SSWs to variability in the ionosphere, the question remains as to why such strong stratospheric PW2 activity prior to the SSW does not produce a clear ionospheric signature while a weaker PW1 appears to perturb the tides globally and in-turn impact the low-latitude ionosphere. In terms of introducing semidiurnal perturbations to the ionosphere, we consider the mean wind conditions and planetary wave amplitude in the MLT region (ca 70-100 km, where the semidiurnal tide achieves large amplitude) to be of greater importance than those in the stratosphere. SABER temperature observations (not shown) reveal that although  $PW1$  was relatively weak in the stratosphere, it was still of significant amplitude above  $\sim 50$  km during the 2009 SSW. It is, therefore, not surprising that it is able to globally modulate the semidiurnal tides. Additionally, the mean wind conditions in the MLT can significantly impact tidal propagation and thus impact viability of the planetary wave-tide interaction mechanism to influence the ionosphere. The zonal mean zonal wind reversal from eastward to westward in the stratosphere that occurred on day 24 (Figure 4.4) was preceded by strong westward winds in the MLT region for several days [Manney et al., 2009]. The MLT winds subsequently became eastward. The strong westward winds in the MLT occurred during the peak of PW2 activity and will inhibit the growth of westward propagating tides (since semidiurnal westward phase speeds are very slow at high latitudes) and may explain why significant perturbations are not observed prior to the SSW despite strong PW2 forcing. The strong westward

winds during this time period may also be responsible for the decrease in strength of *SW2* (Figure 4.4c) that occurs immediately prior to the SSW. If Doppler-shifting effects are playing a significant role, this may also account for the absence of any significant *SW3* and *SW4*. Conversely, following the onset of the SSW, the strong eastward winds in the MLT are favorable for the propagation of westward waves. The winds in the MLT following the SSW onset will, therefore, facilitate the global perturbation of westward propagating tides, such as those that result from the nonlinear interaction between *PW1* and *PW2* and the migrating semidiurnal tide. During this time period the 12-16 day oscillations in the strength of *PW1* globally modulate the tides at a similar periodicity and the eastward winds in the MLT serve to enhance the tidal perturbation and better enable its ability to reach the dynamo region. The changing wind conditions may also explain why the perturbation in *S0* due to the nonlinear interaction between the migrating tide and *PW2* is not observed until the SSW onset. The strong eastward winds in the MLT persisted following the SSW [Manney et al., 2009] and we believe that this may be responsible for the persistence of the semidiurnal tidal perturbations for an extended time period following the SSW. However, it is also possible that this is associated to some degree with a seasonal change in mean winds and tides. Based on the above, we surmise that changes in the mean winds associated with SSWs may have an important role in the global perturbation of the migrating and nonmigrating semidiurnal tides, which modulate the dynamo electric fields and in-turn perturb the low-latitude ionosphere. The occurrence of SSWs is therefore considered to be of importance to the coupling between planetary waves at high-latitudes and the low-latitude ionosphere. However, the degree to which changes in the background circulation associated with SSWs influences this coupling is presently unknown and additional studies are necessary to fully understand this relationship. For instance, Doppler-shifting effects are not the sole influence on tidal propagation; the significant latitudinal and vertical zonal mean wind gradients that occur during SSW also exert strong influences on the propagation efficiency of tides.

#### 4.2.4 Conclusions

In the present study we analyze the ionospheric response to the 2009 SSW to gain insight into the mechanisms which couple SSWs to ionospheric variability. The observations reveal significantly perturbed migrating and nonmigrating semidiurnal tides in the GPS TEC in the EIA crest region during the SSW. We further demonstrate close correspondence between the PW1 activity in the high-latitude Northern Hemisphere and the *SW1* nonmigrating tide in the low-latitude ionosphere. These results present the first observational evidence that the coupling between SSWs and the ionosphere is related to the nonmigrating tides generated by the nonlinear interaction between planetary waves and the migrating semidiurnal tide. Furthermore, the changes in the mean wind conditions in the MLT region during SSWs appear to play an important role in facilitating the coupling between planetary waves concentrated at high-latitudes and variability in the low-latitude ionosphere.

## Chapter 5

### Periodic variations in the ionosphere and plasmasphere due to recurrent geomagnetic activity

Discussion of periodic temporal variations in the ionosphere is continued in the present chapter. However, while the preceding chapter dealt with periodic temporal variations in the ionosphere of lower atmospheric origin, the present discussion focuses on variability of solar origin. Specifically, the influence of recurrent geomagnetic activity on the ionosphere and plasmasphere is studied. An overview of the influence of recurrent geomagnetic activity on near-Earth geospace was previously provided in section 1.1.

This chapter investigates two aspects of the near-Earth geospace response to recurrent geomagnetic activity. First, in Section 5.1, the latitude and local time dependence of the ionospheric response is presented and discussed in the context of previously studied periodic perturbations in thermospheric neutral density [Lei et al., 2008a] and composition [Crowley et al., 2008]. Second, a method is developed to determine the position of the plasmopause from COSMIC topside ionosphere/plasmasphere TEC observations, and is applied to illustrate the occurrence of periodic oscillations in the plasmopause during 2008. Similar to the preceding chapters, each section begins with a brief introduction followed by discussion of the data analysis procedures. This is followed by presentation and discussion of the pertinent results. Each section concludes by briefly summarizing the results and identifying any unanswered questions.

## 5.1 Ionosphere response to recurrent geomagnetic activity: local time dependency

### 5.1.1 Introduction

Recently, oscillations at periods of 7- and 9-days during 2005 and 2006 in global mean GPS TEC were correlated with recurrent solar wind high-speed streams, related to coronal hole distributions on the sun [Lei et al., 2008b]. Similar oscillations were also observed in thermosphere neutral density and composition during this time period [Crowley et al., 2008; Lei et al., 2008a; Thayer et al., 2008]. Although the ionospheric response to recurrent geomagnetic activity has previously been demonstrated [Lei et al., 2008b] the degree to which periodic oscillations in thermospheric neutral composition, density, and winds influence the ionosphere at different latitudes and local times has yet to be demonstrated.

Thermosphere neutral composition, density, temperature, and winds may be changed globally resulting from the periodic energy injection at high-latitudes associated with recurrent geomagnetic activity due to solar wind high-speed streams. These global changes in the thermosphere modify the plasma-neutral interactions resulting in changes in ionospheric electron densities and TEC. Owing to the different mechanisms present during the daytime (production and loss) versus the nighttime (loss only) the ionosphere will respond differently to these thermospheric changes depending on the local time. During the daytime, at F-region altitudes electron production is primarily due to photoionization of  $O$  and loss is primarily due to charge exchange of  $O^+$  with  $N_2$  and  $O_2$  and subsequent dissociative recombination of  $NO^+$  and  $O_2^+$  [Prölss, 1995]. Daytime F-region electron densities and TEC are thus expected to respond to the changes in  $O/N_2$  ratio that occur due to recurrent geomagnetic activity [Crowley et al., 2008]. However, enhanced equatorward neutral winds associated with the recurrent geomagnetic activity are also present and will elevate the F-region ionosphere, resulting in enhanced electron densities [Fuller-Rowell et al., 1994]. The daytime ionospheric response to recurrent geomagnetic activity is thus expected to be influenced by the combination of changes in thermospheric neutral composition and enhanced equatorward winds.

The absence of photoionization at night means that the nighttime ionospheric response to recurrent geomagnetic activity will be different than the daytime response. The dominant process driving changes in the nighttime ionosphere is loss through recombination. Changing concentrations of  $N_2$  and  $O_2$  due to atmospheric upwelling will modify chemical loss rates and in-turn electron densities and TEC. The effect of enhanced equatorward winds is less at night since an increase in the F-layer peak height will not significantly influence the F-layer peak density or TEC. However, the thermospheric neutral wind circulation pattern controls the horizontal transport of  $N_2$  and  $O_2$  so changes in thermospheric neutral winds still influence the response of the nighttime ionosphere.

From the above discussion, it is clear that many factors potentially influence the ionospheric response to recurrent geomagnetic activity associated with solar wind high-speed streams and it is the aim of this section to investigate the latitude and local time dependency of the response. The ionospheric response is illustrated using observations of GPS TEC and in-situ electron densities from the CHAMP satellite during the time period of days 25 - 100 (25 January - 10 April) 2005. This combination of observations provides different perspectives on the daytime and nighttime ionospheric response to changes in thermospheric neutral composition, density, and winds associated with recurrent geomagnetic activity.

### **5.1.2 Data and Methods**

#### **5.1.2.1 Total Electron Content**

Observations of vertical TEC are obtained using Jet Propulsion Laboratory GIMs made available through the Crustal Dynamics Data Information System (<http://cddis.gsfc.nasa.gov>). The GIMs are generated by fitting observations of slant TEC from around 200 GPS receivers to a set of basis functions [*Mannucci et al.*, 1998]. The distribution of the receivers is not uniform and thus a significant amount of smoothing results from the fitting procedure. For example, between 40-50°N latitude 43 GPS receivers are present, whereas, between 40-50°S latitude only 4 receivers are used in the fitting procedure. As we are concerned with multi-day oscillations on a global scale, the

sparseness of the receiver distribution and the significant smoothing that this entails, particularly in parts of the Southern Hemisphere, will not influence the present analysis. The GIMs have a temporal resolution of 2 hours and a spatial resolution of  $5^\circ$  in longitude and  $2.5^\circ$  in latitude. The GIMs are used to generate a time series of vertical TEC in  $2.5^\circ$  magnetic latitude bins at a constant local time. At a fixed local time, wave-like longitudinal structures are observed in low-latitude TEC due to the influence of nonmigrating tides on E-region dynamo electric fields [Scherliess et al., 2008; Wan et al., 2008]. Since a fixed local time is used, the longitude of the vertical TEC observation changes every 2 hours which introduces short-period (sub-daily) oscillations in the TEC time series. The present study is focused on longer-period oscillations and the short-period oscillations are not thought to impact the results.

#### 5.1.2.2 CHAMP In Situ Electron Density

CHAMP in-situ electron density measurements at 15 second intervals ( $\sim 120$  km in-track distance) available through the Information Systems and Data Center operated by Geo Forschungszentrum (GFZ) Potsdam (<http://isdc.gfz-potsdam.de>) are used. It is important to recognize that the electron densities are at a near-constant height and are sensitive to changes in the F-layer peak height. Furthermore, the height of the CHAMP satellite changes over the course of an orbit. During early 2005, the altitude of the CHAMP satellite was approximately 370 km, 365 km, 350 km, at latitudes of  $-75^\circ$ ,  $0^\circ$ , and  $+75^\circ$ , respectively, and the altitude of the satellite decreased by a few kilometers during the study period due to orbital decay. Despite the variability introduced by the changing measurement location with respect to the F-region peak height, the electron densities from the CHAMP satellite are advantageous due to their global coverage. CHAMP also observes electron densities at two local times that are separated by 12 hours, offering the opportunity to explore local time dependencies. Owing to the near-constant sampling in local time, longitudinal structures are also observed in CHAMP electron densities [Lühr et al., 2007; Pedatella et al., 2008], generating short-period oscillations in the time series. These are eliminated from the CHAMP data by calculating daily zonal mean electron densities in  $1^\circ$  magnetic latitude bins.

### 5.1.3 Results

TEC from days 25 - 100, 2005 is given as a function of latitude and universal time at local times of 12 and 4 in Figures 5.1b and 5.1d, respectively. This pair of local times is considered to be representative of the daytime and nighttime ionosphere. The time period is the same time period that significant 9-day oscillations were observed in thermospheric neutral density [Lei et al., 2008a] and composition [Crowley et al., 2008]. The sub-daily oscillations present in the time series are due to the changing longitude of the TEC observations and the enhanced TEC over certain longitude sectors. At mid-latitudes in the Northern Hemisphere, a  $\sim 27$ -day variation due to solar rotation can be observed at 12 local time (LT). As can be seen in Figure 5.1d, the high-latitude nighttime ionosphere also exhibits multi-day oscillations at periods less than the solar rotation period. To illustrate the periodicities of the oscillations that are present in the TEC time series, Lomb-Scargle (LS) periodograms [Lomb, 1976; Scargle, 1982] were calculated using TEC observations at  $45^\circ$  magnetic latitude. The LS periodograms are shown in Figures 5.1a and 5.1c for local times of 12 and 4, respectively. Although some latitudinal variation exists, the LS periodograms at  $45^\circ$  magnetic latitude are representative of the dominant periodicities seen at all latitudes. The LS periodogram of  $K_p$  during this time period is also shown. Consistent with prior studies [Lei et al., 2008b] there is a peak in both TEC and  $K_p$  at a period of 9-days, illustrating the presence of 9-day oscillations in the ionosphere during early 2005. An 11-day peak in  $K_p$  is also present and is above the 95% significance level. A peak in the daytime TEC is also seen at a period of 11-days, however, in both cases the amplitude at a period of 9-days is significantly greater than that at 11-days and we thus focus our attention on the 9-day periodicity.

Observations of in-situ electron densities from the CHAMP satellite from days 32 - 100, 2005 are shown in Figures 5.2b and 5.2e for the descending (daytime) and ascending (nighttime) portions of the orbit. The local time of the equatorial crossing is overlaid and precesses due to the satellite orbit. At high-latitudes the local time sampling deviates from the equatorial crossing local time and we have only presented CHAMP data between  $\pm 65^\circ$  magnetic latitude where the local time remains

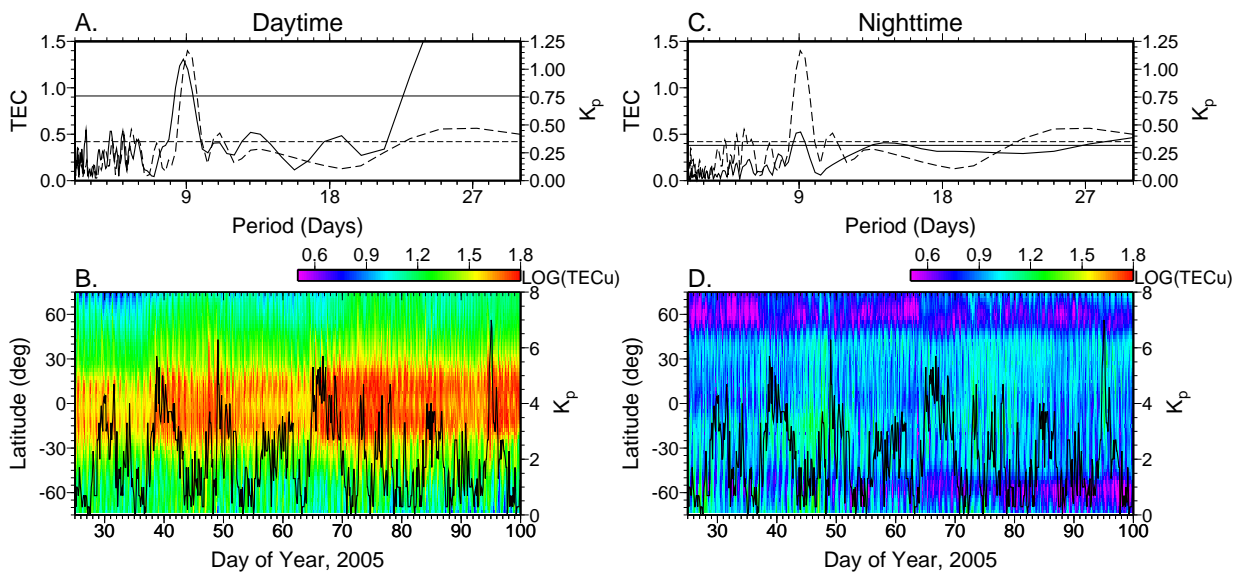


Figure 5.1: (A) Lomb-Scargle periodograms of GPS TEC at  $45^\circ$  magnetic latitude and 12 LT (solid) and  $K_p$  (dashed). The horizontal lines indicate the 95% significance level. (B) Raw GPS TEC observations at 12 LT as a function of magnetic latitude and time for days 25-100, 2005. Solid black line is the  $K_p$  index during this time period. (C-D) Same as (A-B) except for at 4 LT. The units of the GPS TEC observations are TECu where  $1 \text{ TECu} = 10^{16} \text{ electrons/m}^2$ .

nearly constant. The several-hour change in local time that occurs over the time series produces the long term trend that can be seen in Figures 5.2b and 5.2e. Similar to the TEC observations, the nighttime CHAMP in-situ electron density observations reveal multi-day oscillations at high-latitudes in the Northern Hemisphere. LS periodograms of CHAMP electron densities at 45°N magnetic latitude in Figures 5.2a and 5.2d reveal dominant periodicities of 9-days. Periodicities of  $\sim 5.5$ -days and  $\sim 11.5$ -days during the daytime and near 17-days at night are also present. The origin of these periodicities is unknown, however, the  $\sim 5.5$ - and  $\sim 17$ -day periodicities may be due to planetary wave activity [Lastovicka, 2006] and the peak near 11.5-days may be the result of the 11-day peak observed in  $K_p$ .

Having established that 9-day periodicities are present in both daytime and nighttime observations in both data sets, we now turn our attention to illustrating the latitudinal and local time dependencies. In order to elucidate the 9-day oscillations that are present, we compute residuals from an 11-day running mean and subsequently apply a bandpass filter to the residuals. This is the same approach that Lei et al. [2008a] applied to thermosphere density and we similarly use a bandpass filter centered at 9-days with half power points at six and 12 days. Bandpass filtered CHAMP residuals, expressed as a percentage of the running mean, are presented in Figures 5.2c and 5.2f along with the bandpass filtered  $K_p$ . Bandpass filtered TEC residuals at different local times are shown in Figure 5.3. Our initial focus is on the GPS TEC results in Figure 5.3 and will discuss the bandpass filtered CHAMP observations subsequently. As can be observed in Figure 5.3, there are clear differences in the magnitude and latitude structure between the nighttime and daytime responses. At night, the largest enhancements are  $\pm 35$  percent of background levels and are observed at high-latitudes. Northern latitudes and low-mid southern latitudes experience TEC depletions a few days following the peak of the bandpass filtered  $K_p$ . Additionally, the nighttime TEC enhancements poleward of around  $-50^\circ$  N magnetic latitude generally occur 1-2 days prior to the enhancements that are observed at other latitudes. The daytime TEC response (Figure 5.3, left panels) is significantly different, with the magnitude of the response being  $\sim 10$ -15 percent smaller and concentrated at mid-latitudes in the Northern Hemisphere. The low-mid latitude ionosphere is

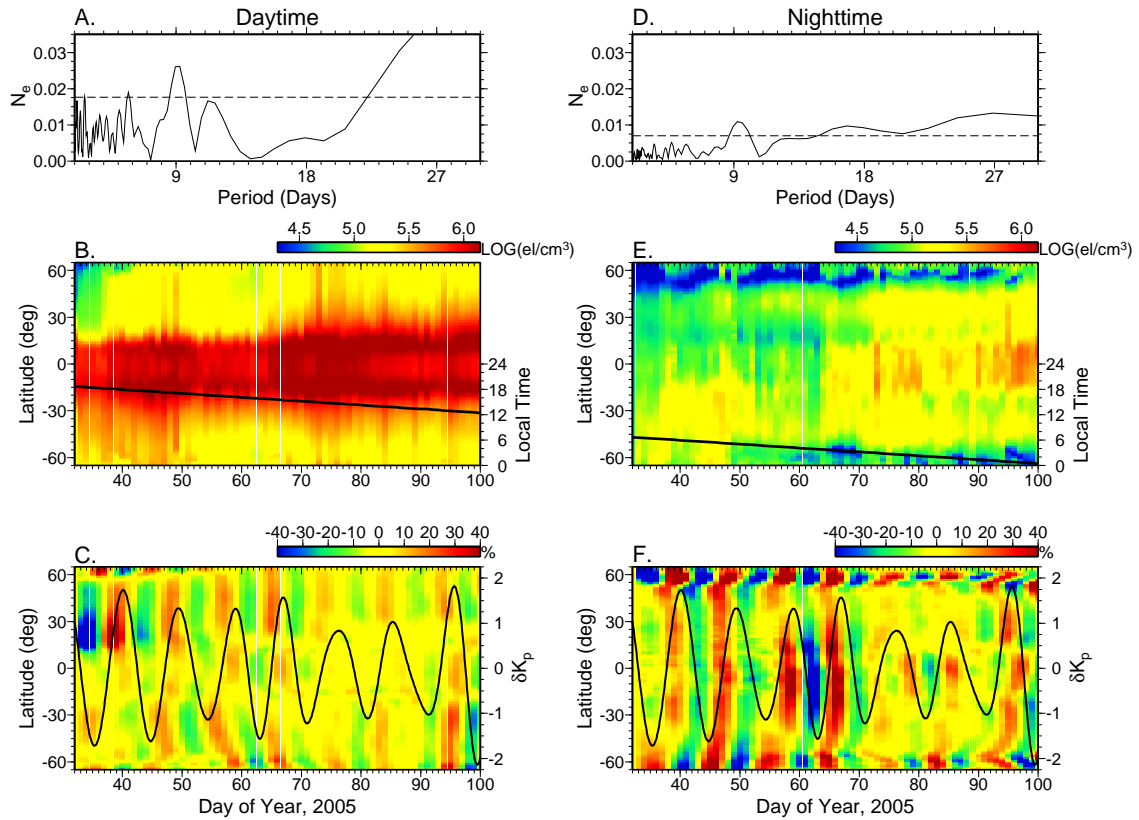


Figure 5.2: (A) Lomb-Scargle periodogram of CHAMP in-situ electron density measurements at  $45^\circ$  magnetic latitude for the descending portion of the orbit. The 95% significance level is indicated by the horizontal dashed line. (B) Descending in-situ electron densities as a function of magnetic latitude and time for days 32-100, 2005. The local time of the equatorial crossing is indicated by the solid black line and is nearly constant for the range of latitudes shown. (C) Bandpass filtered electron density residuals. Residuals are expressed as a percentage of the 11-day running mean. Overlaid are the bandpass filtered  $K_p$  values. (D-F) Same as (A-C) except for the ascending portion of the orbit.

in-phase with  $K_p$  during the daytime while high-latitudes are nearly anti-correlated with the band-pass filtered  $K_p$ . Potential causes for the different latitudinal structures observed in the response of the daytime and nighttime ionosphere to recurrent geomagnetic activity will be discussed later.

The bandpass filtered CHAMP in-situ electron density residuals presented in Figures 5.2c and 5.2f generally reveal similar latitude and local time dependencies as the GPS TEC results. However, due to the near-constant height of the CHAMP observations, some differences exist and the oscillations in CHAMP in-situ electron densities are 10-15 percent larger than those in the GPS TEC. The larger magnitude of the oscillations in CHAMP in-situ electron density observations is primarily attributed to the near-constant height of the CHAMP satellite and the influence of changes in the F-layer peak height on the observations. The periodic geomagnetic activity will introduce variations in the F-region peak height due to a combination of thermospheric heating as well as increased meridional winds. Since the CHAMP satellite is above the F-region peak, the increase in F-layer height means that the in-situ electron density observations occur at a different point with respect to the F-layer peak which can explain why larger oscillations are observed in the CHAMP electron densities compared to TEC.

#### 5.1.4 Discussion

The primary drivers of the ionospheric response to recurrent geomagnetic activity are thought to be changes in thermospheric neutral composition, temperature, and winds as well as auroral energetic particle precipitation and we will first briefly discuss how each may influence the daytime and nighttime observations of TEC and CHAMP in-situ electron densities. At night, enhanced equatorward winds increase the F-layer height at low-mid latitudes without significantly affecting the F-layer peak density or TEC due to the lack of photoionization. However, since the CHAMP satellite is above the F-layer peak height, it senses an electron density increase on the order of  $e^{\Delta z/H_p}$ , where  $\Delta z$  is the upward displacement and  $H_p$  is the plasma scale height. Thermospheric heating associated with geomagnetic activity results in a more barometrically-inflated atmosphere at night; however, since the ionosphere follows a constant pressure surface this does not change the

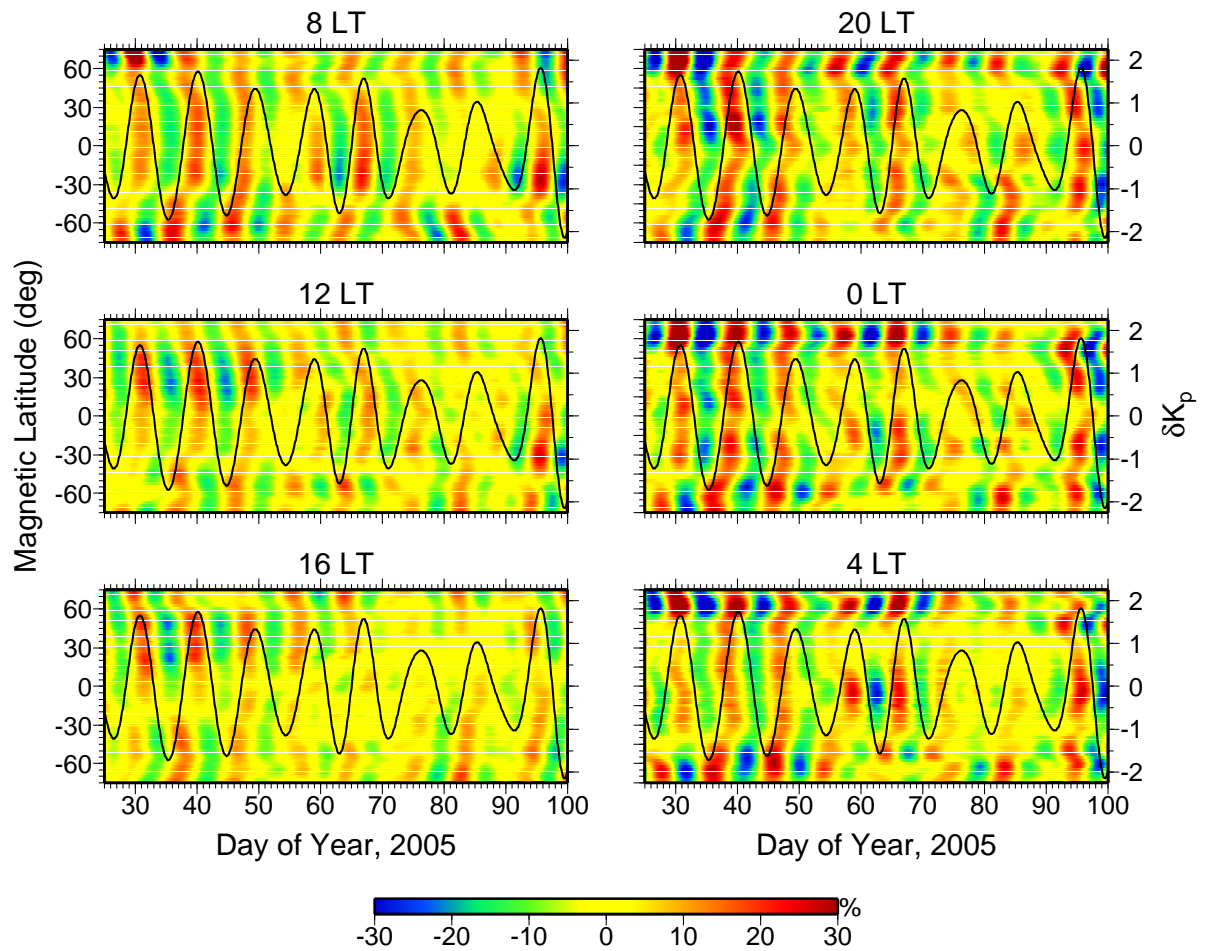


Figure 5.3: Bandpass filtered GPS TEC residuals at different local times for days 25-100, 2005. Results are expressed as a percentage of the 11-day running mean. The bandpass filtered  $K_p$  is overlaid.

F-layer peak density [Rishbeth and Edwards, 1989, 1990]. On the other hand, this may introduce small increases in TEC due to a larger scale height in the topside ionosphere. At a near-constant height, electron densities as measured by the CHAMP satellite *will* increase as a result of atmospheric expansion associated with thermospheric heating. Changes in vertical winds can increase concentrations of  $N_2$  and  $O_2$  at F-region altitudes and nighttime TEC and CHAMP in-situ electron densities will decrease in connection with enhanced chemical loss rates. Lastly, at high-latitudes, enhancements in F-region electron density and TEC occur due to an increase in particle precipitation associated with a rise in geomagnetic activity [Prölss, 1995].

During the daytime, electron densities and TEC tend to follow the  $O/N_2$  ratio since increased  $O$  implies increased production and decreases in  $N_2$  (and  $O_2$ ) reduce the loss rate, increasing the electron density. In contrast to nighttime, an elevated F-layer due to enhanced equatorward winds does increase the F-region maximum electron density [Rishbeth, 1998] and this is reflected in an increase in TEC. Similar to the nighttime, this will also result in an increase in electron densities at a near-constant height, although the effect should be more pronounced due to the combination of both an increase in F-layer peak height and density.

Based upon the above, we should be able to explain the salient features and local-time dependencies of the bandpass filtered data presented in Figures 5.2 and 5.3. We begin with the nighttime data in Figures 5.2f and 5.3 (right panels). During the first half of this period, a mean summer to winter (northward) circulation is expected to exist, that transitions to a weak poleward flow in each hemisphere as equinox (day 81) is approached [Roble et al., 1997]. Superimposed on the mean circulation are equatorward flows throughout this interval connected with the diurnal solar tide and with high-latitude heating. The nighttime perturbations in the GPS TEC and CHAMP in-situ electron densities arise primarily from changing circulation associated with geomagnetic activity, the effects of which can be assisted or impeded by the underlying solar-driven flows.

At high-latitudes in the Southern (summer) Hemisphere, a series of alternating "cells" of negative and positive TEC perturbations are observed at night as seen in Figure 5.3 (right panels). These regions are anti-correlated with the bandpass filtered  $K_p$  residuals. We interpret the negative

TEC regions as locations of enhanced  $N_2$  due to upwelling which increases the loss rate due to recombination. It is worth noting that the regions of enhanced TEC present at these latitudes should be considered as relative enhancements that occur due to the application of a bandpass filter. In other words, physical processes associated with the recurrent geomagnetic activity create a depletion in the TEC and after bandpass filtering enhancements are observed  $\sim 4.5$  days before and after the depletion. The fact that many of the increases or decreases observed in the bandpass filtered results are relative is important to consider throughout the following discussion. The regions of depleted TEC are consistent with the dayside  $O/N_2$  variations measured by the TIMED/GUVI instrument during this same period [Crowley et al., 2008] (we expect similar variations to occur at night). A few days later, as  $K_p$  is declining, negative TEC perturbations occur at low-mid latitudes in the Southern Hemisphere as a result of the equatorward transport of  $N_2$  (and enhanced chemical loss) from the polar-auroral regions towards the equator [Rishbeth et al., 2000]. Assuming a transit of  $75^\circ$  latitude in 2.5 days, a mean transport speed of 40 m/sec is inferred. Some time delay may also be associated with the atmosphere transitioning from its "mixed state" with enhanced  $N_2$ , to a diffusive equilibrium state, which would increase our estimated transport speed.

We expect that similar processes are responsible for the nighttime ionospheric response in the Northern (winter) Hemisphere, which are nearly symmetric about the geomagnetic equator. However, it is seen that the "cellular" TEC perturbations at high-latitudes in the Northern Hemisphere are opposite in-phase with those in the Southern Hemisphere (i.e. Northern Hemisphere enhancements and Southern Hemisphere depletions occur nearly simultaneously). These TEC oscillations are consistent in amplitude and phase with those known to occur in connection with enhanced auroral particle precipitation and latitudinal migration of the wintertime sub-auroral trough under conditions of varying geomagnetic activity [Field and Rishbeth, 1997], and we presume this to be the explanation for this effect. Note also that the intensity of the nighttime TEC perturbations at all latitudes diminishes during the reduced  $K_p$  perturbations between days 70 and 90. The transition from a solstice-like to equinox-like solar-driven mean circulation may also be playing a role in this behavior. This change towards a more hemispherically-symmetric circulation may also result

in enhancements in  $N_2$  at low-latitudes and may be responsible for generating the TEC minima observed over the equatorial region near days 62, 70, and 98.

The nighttime CHAMP observations presented in Figure 5.2f reveal all of the salient features present in the nighttime TEC observations, except that the oscillations are 15-20 percent larger in the CHAMP data. As discussed above, this is likely due to the fact that CHAMP is at a near-constant height and reflects both changes in electron densities due to the mechanisms previously discussed and changes in the F-layer peak height associated with variations in equatorward neutral winds and thermospheric heating.

As can be seen in Figure 5.3 (left panels), the response of the daytime ionosphere to recurrent geomagnetic activity is significantly different than the nighttime response, indicating that processes conspire differently to determine the daytime response. Near noon local time, the meridional flow associated with the solar diurnal tide is poleward in each hemisphere, thus providing resistance to the equatorward-directed flow originating from polar-auroral heating. On the other hand, the prevailing summer to winter circulation is still expected to be operative, at least until days 60-70. This combination of circulations may at least be partially responsible for the more asymmetric response in TEC between low- and high-latitudes during the daytime and the longer delay between the maximum in  $K_p$  and the maximum depletion in TEC (now 3-4 days). Furthermore, the maximum depletions, at least prior to day 60, occur at mid-latitudes in the Northern Hemisphere, implying that  $N_2$  may be piling up in this region as a result of transport from both auroral regions. In addition, and perhaps alternatively, before day 60 there are enhancements of TEC near the maxima of  $K_p$  that are likely due to uplifting of the F-layer and the accompanying increase in the F-layer maximum electron density and TEC. The abatement in meridional wind that occurs near the minimum in the bandpass filtered  $K_p$  residual would be accompanied by a relative decrease in TEC, and this may be why the time delay between the maximum in  $K_p$  and the minimum in TEC perturbations is so long on the dayside. It should be noted that a decrease in the bandpass filtered TEC does not necessarily imply that a physical process is coincidentally causing a reduction in electron densities. Rather, due to the nature of bandpass filtering, a negative TEC perturbation

can be due to an increase in TEC  $\sim 4.5$  days prior to the decrease.

We again observe similar features in the daytime CHAMP in-situ electron density perturbations (Figure 5.2c), although the oscillations are slightly higher in amplitude and the hemispheric symmetry is more clearly observed, especially beginning on day 50. One feature that is present in the CHAMP observations that is not seen in the GPS TEC data is a separation between equatorial-region and mid-latitude depletions around  $\pm 15^\circ$  magnetic latitude beginning on day 60. Since this occurs near the equatorial ionization anomaly, some connection with changes in the strength of electric fields is suggested. This effect may be due to westward daytime disturbance dynamo electric fields [Blanc and Richmond, 1980] produced by the periodic oscillations in the wind field driven by the recurrent geomagnetic activity. This may also provide an explanation for the relative plasma depletions observed in the daytime GPS TEC observations in the equatorial region.

Our ability to definitively deduce the mechanisms driving the observations reported here is limited. In fact, it is likely that some combination of changes in chemical loss rates and vertical motion of the F-layer are responsible for the observed features (whether wind-driven or electric field-driven). Due to the lack of ability to simultaneously observe all of the necessary parameters (e.g. thermosphere composition and winds, electric fields, ionospheric densities), numerical modeling is required in order to elucidate the dominant effects and it is our hope that these observations will provide the impetus for such modeling investigations.

### 5.1.5 Conclusions

The results in the present section are the first to reveal the daytime and nighttime dependence of the influence of recurrent geomagnetic activity due to solar wind high-speed streams on the ionosphere. Similar features are observed in both GPS TEC and CHAMP in-situ electron density measurements; however, the oscillations in CHAMP electron densities are 10-15 percent larger. The greater amplitude of the CHAMP oscillations is the result of the sensitivity of the in-situ observations to changes in the F-layer peak height and may also be due to the significant smoothing involved in generation of the GIMs. The ionospheric response to recurrent geomagnetic activity

is due to the same physical mechanisms that perturb the ionosphere during classical ionospheric storms that are typically considered as isolated events. However, the magnitude of the disturbance is moderate and the recurrent nature of the geomagnetic activity permits isolation of the ionospheric response to a single forcing mechanism. The nighttime response appears to be driven by changes in the electron density loss rate due to upwelling of  $N_2$  at high-latitudes in the Southern Hemisphere and subsequent transport of  $N_2$  towards equatorial regions by equatorward neutral winds. The high-latitude Northern Hemisphere response, however, appears to be dominated by the latitudinal migration of the wintertime sub-auroral trough and enhanced particle precipitation. During the daytime, the latitudinal structure of the ionospheric response is different owing to the presence of photoionization. The observed changes in GPS TEC and CHAMP in-situ electron densities during the daytime are thought to be primarily due to a combination of changes in neutral composition and uplifting of the F-layer due to enhanced equatorward winds.

## **5.2 Routine determination of the plasmopause based on COSMIC GPS TEC observations of the mid-latitude trough**

### **5.2.1 Introduction**

The plasmasphere consists of relatively cold, high-density plasma that approximately corotates with the Earth. The outer boundary of the plasmasphere, known as the plasmopause, is highly dynamic and represents the boundary between plasma controlled by the Earth's corotation electric field and plasma influenced by magnetospheric electric fields [Lemaire and Gringauz, 1998]. Due to its dynamic nature and importance for understanding mass and energy flow in the inner magnetosphere, determining the location of the plasmopause has attracted significant attention and a variety of techniques have been implemented for this purpose. Early studies of plasmopause location utilized whistler observations along with limited satellite observations [Carpenter, 1966; Carpenter et al., 1968; Gringauz and Bezrukikh, 1976]. In-situ satellite observations of the sharp plasma density gradient found at the plasmopause have also been used, resulting in the development

of several empirical relationships between geomagnetic activity level and plasmapause radius [Carpenter and Anderson, 1992; Moldwin et al., 2002; O'Brien and Moldwin, 2003]. General features of the plasmapause, such as its inward movement with increasing geomagnetic activity were revealed by these observations. More recently, the global views of the plasmasphere and plasmapause afforded by the Extreme Ultraviolet (EUV) instrument on the Imager for Magnetopause-to-Aurora Global Exploration (IMAGE) satellite provided new insight into the nature of the plasmasphere. Such global observations were able to reveal that the structure of the plasmapause is significantly more complex than previously thought and also demonstrated the connection between the plasmapause and other regions, such as the outer radiation belts [Baker et al., 2004; Darrouzet et al., 2009; Goldstein et al., 2003, 2004; Spasojevic et al., 2003].

In addition to direct observation of the plasmapause location, various ionospheric observations are correlated with the plasmapause and have thus been employed to determine its location. Observations have revealed the close relationship between the location of the mid-latitude electron density trough and the plasmapause [Grebowsky et al., 1976; Yizengaw and Moldwin, 2005; Yizengaw et al., 2005]. Additionally, Anderson et al. [2008] demonstrated that the plasmapause location corresponds closely to the light ion trough in the topside ionosphere. Although unable to reveal some of the finer scale structures as effectively as methods such as direct EUV imaging, the use of ionospheric observations to determine the plasmapause is advantageous because relatively continuous observations can be made in different local time sectors. Furthermore, this approach can help maintain continuity of observations during periods when other satellite observations of the plasmapause are unavailable.

The high-sample rate along with the global distribution of receivers make observations of the global GPS TEC ideal for study of the ionosphere and plasmasphere. Ground-based observations of GPS TEC are primarily influenced by electron densities in the F-region [Klobuchar, 1996], consequently GPS TEC observations used to study the disturbed and quiet time ionosphere predominantly reveal characteristics of the F-region ionosphere [Afraimovich et al., 2008; Coster and Komjathy, 2008; Mendillo, 2006]. Ground-based GPS TEC measurements can, however, also reveal

information concerning the structure of the plasmasphere [e.g., Foster et al., 2002]. Observations of TEC from GPS receivers onboard low-Earth orbit (LEO) satellites allow for the separation of the TEC into different altitude regions, enabling a unique perspective on the structure and dynamics of electron densities in both the F-region ionosphere and the topside ionosphere/plasmasphere. Furthermore, compared to ground-based observations, satellite observations of GPS TEC are advantageous due to the more complete global coverage that they offer. As a result of these advantages, GPS TEC observations from LEO satellites have been applied to study several geomagnetic disturbances in order to gain new insight into the dynamics of the storm-time ionosphere as well as the underlying physical mechanisms [Mannucci et al., 2005, 2008; Pedatella et al., 2009; Yizengaw et al., 2006].

The use of GPS TEC observations from LEO satellites has focused primarily on the study of ionospheric storms; however, LEO satellite observations of GPS TEC are well-suited for study of climatological features of the electron densities in the topside ionosphere/plasmasphere and the structure and dynamics of the plasmopause. Additionally, the regular sampling in different local time sectors afforded by LEO satellites makes them advantageous for use in the study of the plasmopause. In the present study, we make use of GPS TEC observations from the six satellite COSMIC to determine the location of the plasmopause throughout 2008. Based on these observations, the variation with geomagnetic activity and local time is illustrated. The COSMIC observations of the plasmopause are also used to demonstrate the occurrence of periodic oscillations in the plasmopause location. This represents a new approach for routine determination of the plasmopause location and is an innovative use of GPS receivers that are flown on LEO satellite for the primary purpose of precise orbit determination.

## 5.2.2 Data Processing

### 5.2.2.1 COSMIC Vertical TEC Observations

The present study utilizes the observations of topside ionosphere/plasmasphere TEC from the COSMIC processed using the methods outlined in Chapter 2. Sufficiently minimizing the multipath effect allows for combining multiple data arcs which improves the continuity of observations while the COSMIC satellites pass through the trough region. The ability to combine data arcs is useful in the event of carrier phase cycle slips and, in the present study, we combine VTEC observations to multiple GPS satellites if they are separated by less than 30 minutes in local time. Combining observations to multiple satellites may introduce some error due to structures in local time, however, this is done to increase the number of available plasmopause observations. Note also that only observations above  $65^\circ$  elevation angle are used in the present analysis.

### 5.2.2.2 Determination of Plasmopause

Based on the methods detailed in Chapter 2, we have obtained a high-quality set of VTEC observations from the COSMIC satellites during 2008 that can be used to determine the location of the plasmopause. As previously demonstrated by Yizengaw et al. [2005], GPS TEC observations of the ionospheric mid-latitude trough are correlated with the position of the plasmopause. In the present study, the COSMIC VTEC observations are used to determine the equatorward edge of the mid-latitude trough and we define the plasmopause to be located at this point. The equatorward edge is defined as the location equatorward of the trough minimum where the gradient exceeds  $0.10 \text{ TECu/degree}$ . Each COSMIC satellite passes through the trough region four times per orbit. The trough is known to exhibit hemispheric asymmetry due to the larger offset between the geomagnetic and geographic poles in the Southern Hemisphere [e.g., Sojka et al., 1985]. Therefore, in the present study, we have only used Northern Hemisphere observations to ensure that any hemispheric differences do not influence the results. As an illustration of our method, the VTEC for a single pass is shown in Figure 5.4 along with where the plasmopause is estimated to be. As can be seen

in Figure 5.4, the COSMIC VTEC observations are capable of identifying the trough region and subsequently determining the location of the plasmopause.

Although the observations shown in Figure 5.4 reveal a distinct mid-latitude trough and allow for estimation of the plasmopause location, it should be noted that this is not always the case for a number of reasons. First, due to only using data above a  $65^\circ$  elevation angle, data gaps are prevalent. The presence of data gaps makes it impossible to unambiguously determine the plasmopause for many passes and any data with gaps greater than 1 minute are not analyzed. Furthermore, there are occasional "jumps" in the data that may result from changes in the GPS satellites used to compute the VTEC or cycle slips in the carrier phase observations. Such "jumps" in the data may lead to inaccurate determination of the plasmopause location, and we thus do not use arcs that contain a greater than 0.3 TECu change in the VTEC from one epoch to the next. The aforementioned restrictions result in elimination of a large number of passes and based on one year of COSMIC observations the location of the plasmopause has been determined for about 1800 passes, which represents  $\sim 19\%$  of the possible crossings. Clearly, there are some drawbacks to the present method; however, the good spatial resolution and local time coverage of the COSMIC observations represent significant advantages and thus these observations provide a valuable new technique for studying the plasmopause.

### 5.2.3 Results and Discussion

#### 5.2.3.1 Variation with $K_p$

The location of the plasmopause is well known to vary with geomagnetic activity and generally moves inward (outward) with increasing (decreasing) activity levels [Carpenter and Anderson, 1992; Moldwin et al., 2002; O'Brien and Moldwin, 2003]. Therefore, we illustrate the variation with geomagnetic activity to demonstrate the effectiveness of applying the COSMIC observations for determination of the plasmopause during 2008. The plasmopause position for all local times as a function of the maximum  $K_p$  in the previous 24 hours is shown in Figure 5.5. It should be noted

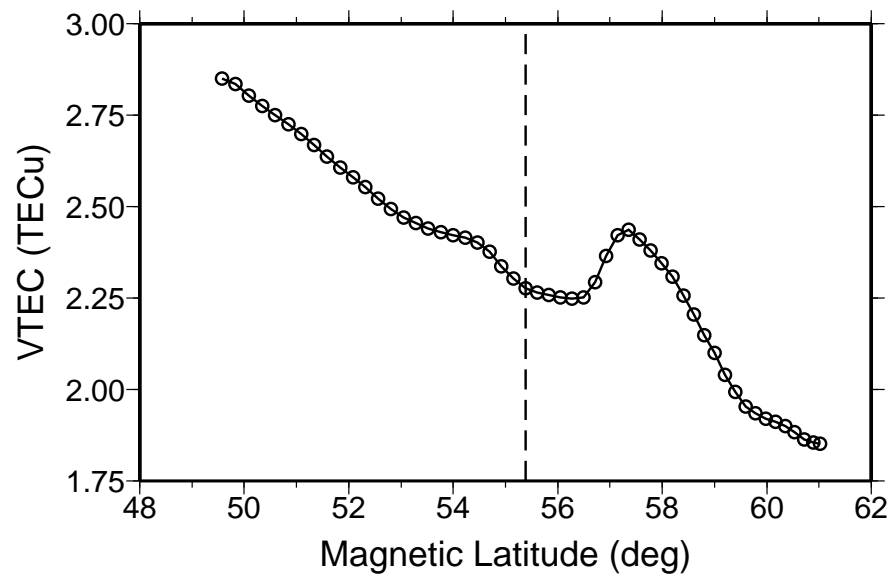


Figure 5.4: Vertical TEC observations for a single COSMIC pass. The estimate of the plasmopause location is indicated by the vertical dashed line. See text for details on determination of the plasmopause location.

that the plasmopause observations during 2008 are biased towards low geomagnetic activity level due to the relative absence of significant geomagnetic activity during this time period. Nonetheless, the reduction in plasmaspheric radius with increasing levels of geomagnetic activity is evident. The best-fit line to the COSMIC observations is also shown in Figure 5.5, along with the best-fit line to CRRES observations previously obtained by Moldwin et al. [2002]. The linear best fit is found to be  $L_{pp} = 5.322 \pm 0.040 - (0.346 \pm 0.019)K_{pmax}$ , compared to the Moldwin et al. [2002] result of  $L_{pp} = 5.390 \pm 0.072 - (0.382 \pm 0.019)K_{pmax}$ . The good agreement between the COSMIC results and previous observations indicates that VTEC observations from GPS receivers onboard LEO satellites, such as the COSMIC, represent a useful means for routine determination of the plasmopause.

### 5.2.3.2 Local Time Variation

The local time variation of the plasmopause location for different levels of geomagnetic activity during 2008 is shown in Figure 5.6. Both the raw observations and the mean plasmopause location within two hour magnetic local time bins are presented. As expected, the COSMIC observations reveal a general decrease in plasmopause radius as the geomagnetic activity level increases. It is also clearly evident that there is significant variability in the plasmopause location about the mean value, with standard deviations on the order of 0.5-1.0 L. The variability is most pronounced at low-levels of geomagnetic activity. Unfortunately, as noted previously, there are considerably fewer observations during periods of high geomagnetic activity compared to low levels of activity due to only using COSMIC observations during 2008. Therefore, the results for  $K_p$  greater than four may not be an accurate representation of the average plasmopause for high levels of geomagnetic activity.

Previous studies of the plasmopause location as a function of local time have revealed both noon-midnight and dawn-dusk asymmetries [Gringauz and Bezrukikh, 1976; Moldwin et al., 2002; O'Brien and Moldwin, 2003]. Although there is slight asymmetry of  $\sim 0.25L$ , the COSMIC observations in Figure 5.6 reveal a plasmopause that is generally invariant in local time and exhibits

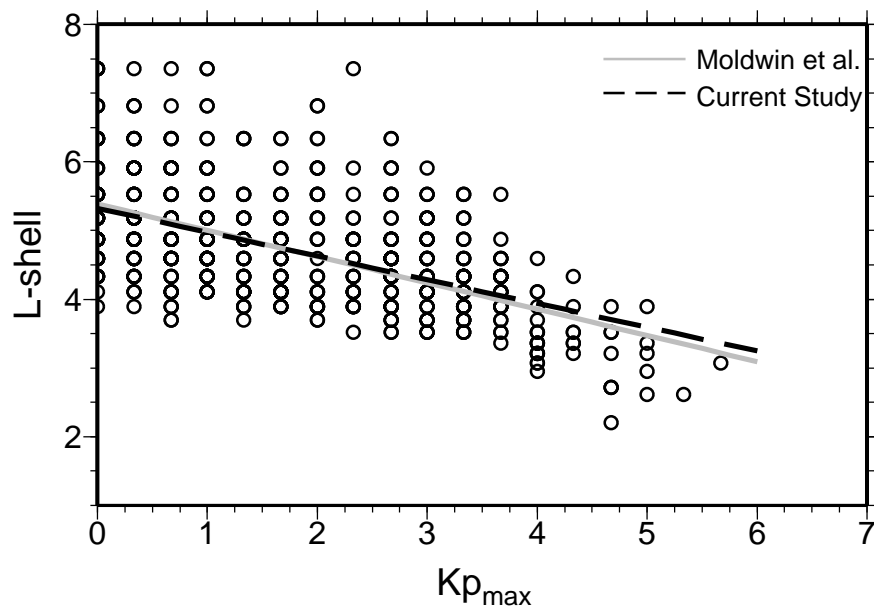


Figure 5.5: COSMIC observations of the plasmapause location during 2008 as a function of the maximum  $K_p$  in the previous 24 hours for all local times. The linear best-fit based on COSMIC observations is shown along with the Moldwin et al. [2002] relationship determined from CRRES observations. Coefficients for both fits are provided in the text.

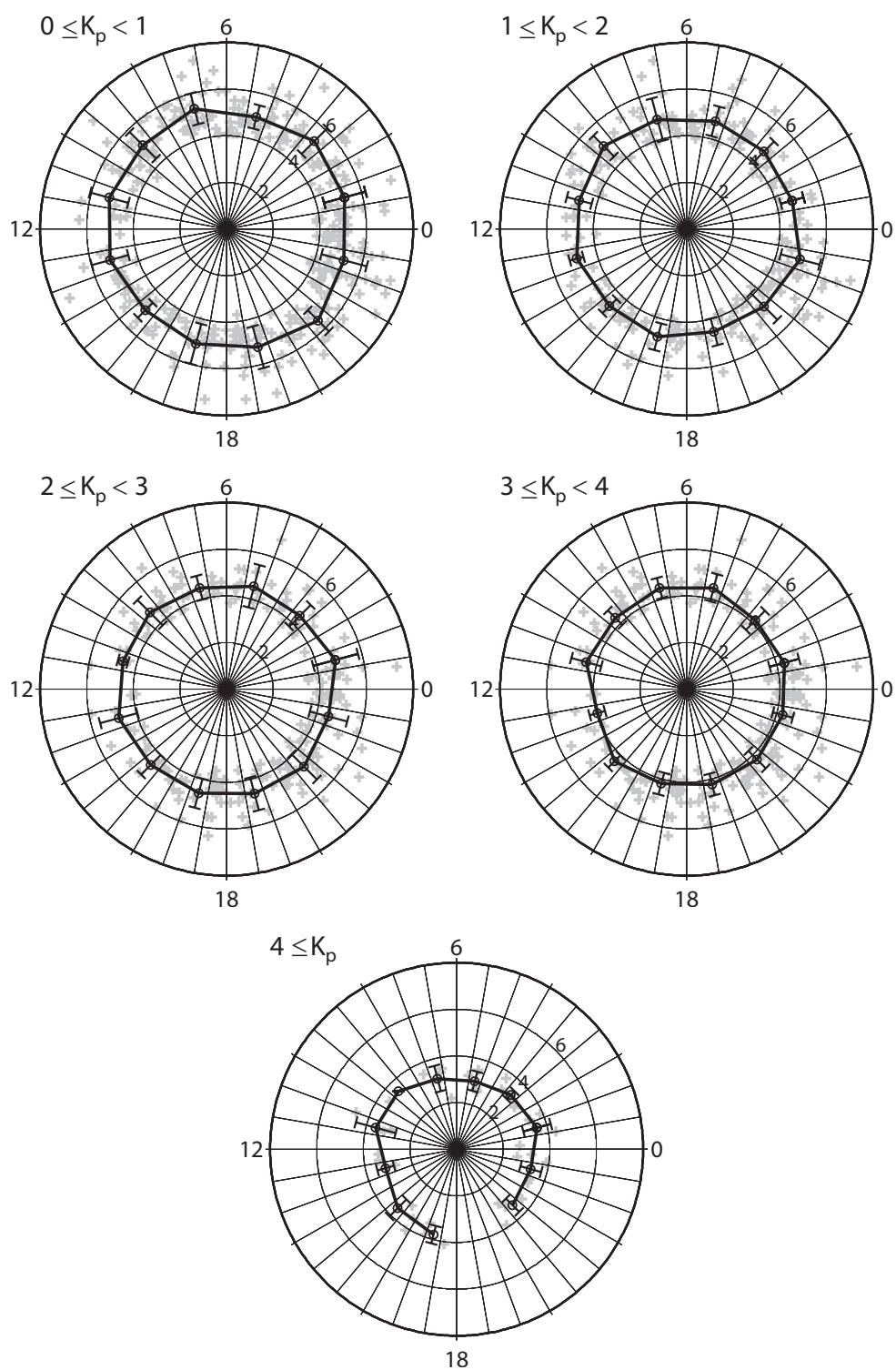


Figure 5.6: COSMIC observations of the plasmopause during 2008 as a function of magnetic local time for different levels of geomagnetic activity. Individual observations are indicated by the grey + symbol. The solid black line indicates the mean and standard deviation within 2 hour local time bins.

significant variability. There are several reasons why the COSMIC observations of the plasmopause may be more symmetric in comparison to previous observations. First, the local time variation presented in Figure 5.6 is representative of average conditions and does not reveal the instantaneous shape of the plasmopause. During periods of quiet geomagnetic activity, the plasmopause is known to exhibit significant structure in local time; however, the location of the bulge region is highly variable even over relatively short time scales [Moldwin et al., 1994]. Such variations in the local time structure of the plasmopause may result in the observed plasmopause being circular in an average sense even though the instantaneous plasmopause exhibits significant structure. Additionally, the location of the trough minimum exhibits a local time dependency that is different than that of the plasmopause [e.g., Werner and Prölss, 1997] and, furthermore Yizengaw et al. [2005] observed that the separation between the equatorward edge of the trough and the plasmopause tends to be larger during the daytime. As the present study assumes that the plasmopause is collocated with the equatorward edge of the trough, the local time structure of the trough combined with any local time difference in the relationship between the plasmopause and equatorward edge of the trough may potentially result in the observed symmetry in local time. In addition to these shortcomings in the present method, the discrepancy with prior observations may be related in part to biases in other methods which may produce a more asymmetrical plasmopause. For example, CRRES observations used by Moldwin et al. [2002] and O'Brien and Moldwin [2003] suffer from insufficient sampling at high L during the daytime which may result in greater local time asymmetry.

### **5.2.3.3 Periodicities during 2008**

During the declining phase of solar cycle 23, oscillations at periods of 7-, 9-, and 13.5-days have been observed in thermosphere neutral composition and density as well as in the ionosphere [Crowley et al., 2008; Lei et al., 2008a,b]. Similar periodicities were also observed during 2008 in auroral electron power, electron fluxes in the outer radiation belt, and solar wind velocity [Gibson et al., 2009]. These periodic oscillations in Earth's upper atmosphere are the result of recurrent geomagnetic activity due to periodic high-speed solar wind streams associated with coronal hole

distributions on the Sun. As the plasmopause location is correlated with the level of geomagnetic activity, one may surmise that the plasmopause should exhibit periodic oscillations during 2008 as well. Lomb-Scargle [Lomb, 1976; Scargle, 1982] periodogram analysis of the daytime (7-18 LT) and nighttime (20-5 LT) plasmopause locations during 2008 along with  $K_p$  are presented in Figure 5.7. Not surprisingly, 9-day periodicities are observed in  $K_p$  as well as the daytime and nighttime plasmopause. Weaker 13.5-day oscillations are also observed, although the 13.5-day period is not above the 95% significance level for the nighttime plasmopause. It is unknown why the 13.5-day oscillation is not significant in the nighttime plasmopause but this may be related to a weaker dependence on geomagnetic activity and larger variability in the plasmopause during these local times [e.g., Moldwin et al., 2002].

Combined with the numerous previous studies on periodic oscillations in Earth's upper atmosphere, the identification of periodic oscillations in the plasmopause demonstrates that the entirety of near-Earth geospace is likely to be influenced by periodic high-speed solar wind streams. Given the importance of the plasmopause for controlling the flow of mass and energy in the inner magnetosphere, the presence of periodic oscillations in the plasmopause has significant implications for this region. Furthermore, observations have demonstrated that the inner edge of the outer radiation belt is closely tied to the plasmopause location [Baker et al., 2004] and our results indicate that the location of the inner edge of outer radiation belt region may also exhibit oscillations during the current solar minimum.

#### 5.2.4 Conclusions

In the present study, the COSMIC VTEC observations are used in order to determine the plasmopause position throughout 2008. The variation of the COSMIC plasmopause observations with the level of geomagnetic activity is similar to the variation obtained by previous studies using different observation methods, indicating the effectiveness of using the COSMIC VTEC observations to routinely observe the location of the plasmopause. It is also observed that, in an average sense, the plasmopause is roughly symmetric in local time. However, there is significant variability

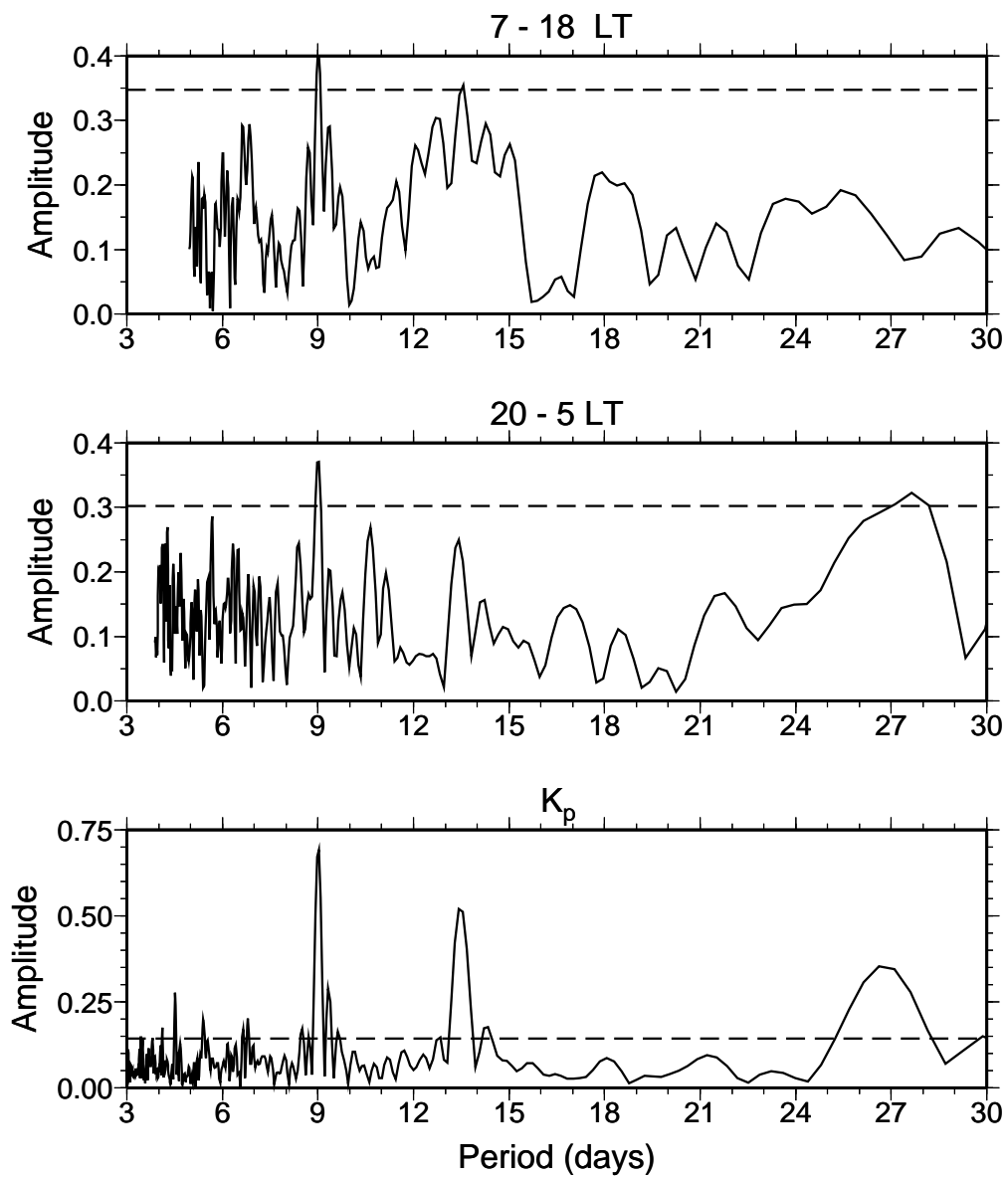


Figure 5.7: Lomb-Scargle periodograms of the COSMIC plasmopause location during 2008 for the daytime (top) and nighttime (middle) as well as  $K_p$  (bottom). The 95% significance level is indicated by the horizontal dashed lines.

and the plasmopause at any given time will exhibit significant structure in local time. Lastly, the plasmopause is found to oscillate at periods of 9- and 13.5-days during 2008 due to recurrent geomagnetic activity associated with solar wind high-speed streams. Such oscillations further demonstrate the significant influence that solar wind high-speed streams have on the Earth's upper atmosphere and inner magnetosphere during the current solar minimum.

The present study is the first to demonstrate the use of GPS TEC observations from LEO satellites for routinely determining the plasmopause. Although we have focused solely on the COSMIC satellites for this purpose, the methods are applicable to any high-inclination satellite with a dual-frequency (non-occluding) GPS receiver that records both carrier phase and pseudorange observations. A number of current satellites (e.g., CHAMP, GRACE, JASON-2) satisfy this criteria and it is anticipated that many future satellites will as well. The results of the present study demonstrate that the GPS TEC observations from these satellites provide a valuable resource for future study of the plasmopause during both quiet and disturbed time periods.

## Chapter 6

### Summary and Conclusions

In recent years there have been significant developments in the understanding of how processes occurring in the lower atmosphere induce significant variability in the ionosphere. These advances combined with recent advances in global observational methods have enabled a detailed study of periodic variability in the ionosphere and plasmasphere in response to lower atmospheric forcing. The studies presented in Chapters 3 and 4 serve to enhance the current understanding of coupling between the lower and upper atmosphere, and have provided answers to the questions laid forth in section 1.4. The chief scientific findings may be summarized as follows:

- During Northern Hemisphere winter months, the F-region ionosphere exhibits wave-2 and wave-3 variations which are attributed to the nonmigrating tides *SW2* and *DE2*. This demonstrates the importance of nonmigrating tides other than the *DE3* that is the subject of the vast majority of past studies concerning the presence of longitudinal variations in the ionosphere. Further, it demonstrates that during Northern Hemisphere winter the longitude variations of concern are wave-2 and wave-3 and not the wave-4 variation that, like *DE3*, has been the subject of numerous prior studies.
- A significant altitude dependence to the longitude variations was both observed and modeled using the newly developed GIP-TIEGCM. This was also observed to exhibit significant seasonal and local time dependencies. It also is worth noting that understanding of this altitude dependence was made possible by development of a method to reduce multipath

present in the COSMIC GPS POD observations. It was found that around equinox, during the daytime, similar longitude variations are observed in the F-region and topside ionosphere/plasmasphere. However, at night different longitude variations are observed at these two altitudes. A notable difference in the longitude variation at these altitudes at all local times was also observed and modeled during solstice time period. The results have demonstrated that the nonmigrating tides considerably perturb the ionosphere at altitudes in excess of 800 km. The effect of nonmigrating tides at these altitudes is thought to be driven by temperature variations influencing the topside ionosphere scale height. Last, it was found that, especially during solstice, the geomagnetic field plays a key role in generating longitude variations in the topside ionosphere/plasmasphere but does not significantly influence the F-region.

- Large-scale changes in tropospheric convection associated with the ENSO were found to influence the longitude variations in the ionospheric F-region. The connection between sea surface temperature variations and variability hundreds of kilometers aloft represents a new discovery, and is worthy of future investigations as discussed below.
- Satellite magnetometer observations were used to investigate longitudinal variations in the global  $Sq$  current system. This represents the first study of the complete longitude variations that are present in the  $Sq$  currents. Significant longitude variations were observed in the  $Sq$  current function. These are attributed to the combined influence of nonmigrating tides and the geomagnetic field orientation. Where past studies have focused on tidal influences on the low-latitude ionosphere, these results demonstrate the importance of nonmigrating tides on perturbing the global ionosphere.
- The quasi-16-day planetary wave was found to significantly influence the low-latitude ionosphere on a global-scale. That is, all longitudes are influenced in a similar manner. The oscillations are significant, and can reach  $\sim 45\%$  of the background electron density at a constant height. It was also found that the low-latitude ionospheric variations that are ob-

served during SSWs are connected to the nonlinear interaction between tides and planetary waves. In particular, the low-latitude *SW1* was found to be connected to the planetary wave-1 activity in the high-latitude stratosphere. This reveals observationally what has previously been shown in numerical models as a mechanism for connecting SSWs to variability in the low-latitude ionosphere.

While the above have enhanced the present understanding of the lower atmosphere on introducing spatial and temporal variability in the ionosphere, there remain some open questions. First, while the role of different nonmigrating tides and the geomagnetic field have been elucidated for the low-latitude ionosphere, this has yet to be done for the global *Sq* currents. Given the longitudinal variations observed in section 3.4, controlled numerical modeling experiments should be performed to investigate the primary sources of these variations. The connection between the ENSO and upper atmosphere is also worthy of additional study. Typical changes that occur in the MLT and upper atmosphere during both the warm and cold portions of the ENSO cycle should be investigated in detail. The connection between day-to-day variations in tropospheric convection and ionospheric variability also presents an opportunity to further investigate the connection between lower and upper atmospheric variability.

In addition to the above, periodic oscillations in the ionosphere and plasmasphere due to recurrent geomagnetic activity was studied in Chapter 5. Two facets of this connection were explored. First, the latitude and local time dependency of the ionospheric response to recurrent geomagnetic activity was investigated. This is the first time that the complete global response of the ionosphere to recurrent geomagnetic activity was studied, and significant local time variations were discovered. Although the magnitude of the variations is smaller, the ionospheric variations due to periodic geomagnetic activity were found to be driven by the same mechanisms which drive larger geomagnetic storms. A method for using LEO satellite TEC observations to study the location of the plasmopause was also developed, and subsequently used to illustrate the presence of periodic variability in the plasmopause during 2008. This demonstrates that the entirety of near-Earth

geospace was perturbed by the recurrent geomagnetic activity during the declining phase of solar cycle 23. Further, the methods developed may be used to study the response to larger geomagnetic storms. The COSMIC, combined with the increasing number of satellites equipped with GPS POD antenna (i.e., Swarm, COSMIC-II) present the opportunity to perform such studies in the future as we head towards the upcoming solar maximum.

## Bibliography

- Afraimovich, E. L., E. I. Astafyeva, A. V. Oinats, Y. V. Yasukevich, and I. V. Zhivetiev (2008), Global electron content: A new conception to track solar activity, *Ann. Geophys.*, *26*, 335-344.
- Alken, P. and S. Maus (2007), Spatio-temporal characterization of the equatorial electrojet from CHAMP, Orsted, and SAC-C satellite magnetic measurements, *J. Geophys. Res.*, *112*, A09305, doi:10.1029/2007JA012524.
- Altadill, D., E. M. Apostolov, J. G. Sole, and C. Jacobi (2001), Origin and Development of Vertical Propagating Oscillations with Periods of Planetary Waves in the Ionospheric F Region, *Phys. Chem. Earth (C)*, *26*(6), 387-393.
- Altadill, D., and E. M. Apostolov (2003), Time and scale size of planetary wave signatures in the ionospheric F region: Role of the geomagnetic activity and mesosphere/lower thermosphere winds, *J. Geophys. Res.*, *108*(A11), 1403, doi:10.1029/2003JA010015.
- Altadill, D., E. M. Apostolov, C. Jacobi, and N. J. Mitchell (2003), 6-day westward propagating wave in the maximum electron density of the ionosphere, *Ann. Geophys.*, *21*, 1577-1588.
- Anderson, P. C., W. R. Johnston, and J. Goldstein (2008), Observations of the ionospheric projection of the plasmopause, *Geophys. Res. Lett.*, *35*, L15110, doi:10.1029/2008GL033978.
- Angelats i Coll, M., and J. M. Forbes (2002), Nonlinear interactions in the upper atmosphere: The  $s = 1$  and  $s = 3$  nonmigrating semidiurnal tides, *J. Geophys. Res.*, *107*(A8), 1157, doi:10.1029/2001JA900179.
- Anthes, R. A. (2011), Exploring the Earth's atmosphere with radio occultation-contributions to weather, climate and space weather, *Atmos. Meas. Tech. Discuss.*, *4*, 135-212, doi:10.5194/amtd-4-135-2011.
- Anthes, R., et al. (2008), The COSMIC/FORMOSAT-3 mission: Early results, *Bull. Am. Meteorol. Soc.*, *89*, 313-333.
- Appleton, E. V. (1946), Two anomalies in the ionosphere, *Nature*, *157*, 691-693.
- Appleton, E. V., and L. J. Ingram (1935), Magnetic storms and upper-atmospheric ionisation, *Nature*, *136*, 548-549.
- Baker, D. N., S. G. Kanekal, X. Li, S. P. Monk, J. Goldstein, and J. L. Burch (2004), An extreme distortion of the Van Allen belt arising from the 'Halloween' solar storm in 2003, *Nature*, *432*, 878, doi:10.1038/nature03116.

- Berkner, L. V., H. W. Wells, and S. L. Seaton (1939), Ionospheric effects associated with magnetic disturbances, *Terrestrial Magnetism and Atmospheric Elec.*, *44*, 283-311.
- Bernhardt, P. A., D. A. Antoniadis, and A. V. daRosa (1976), Lunar perturbations in columnar electron content and their interpretation in terms of dynamo electrostatic fields, *J. Geophys. Res.*, *81*(34), 5957-5963.
- Blanc, M., and A. D. Richmond (1980), The ionospheric disturbance dynamo, *J. Geophys. Res.*, *85*, 1669-1680.
- Borries, C., N. Jakowski, Ch. Jacobi, P. Hoffmann, and A. Pogoreltsev (2007), Spectral analysis of planetary waves seen in ionospheric total electron content (TEC): First results using GPS differential TEC and stratospheric reanalyses, *J. Atmos. Sol. Terr. Phys.*, *69*, 2442-2451.
- Buonsanto, M. J. (1999), Ionospheric storms - A review, *Space Sci. Rev.*, *88*, 563-601.
- Burns, A. G., S. C. Solomon, W. Wang and T. L. Killeen (2007), The ionospheric and thermospheric response to CMEs: Challenges and successes, *J. Atmos. Sol. Terr. Phys.*, *69*, 77-85.
- Byun, S. H., G. A. Hajj, and L. E. Young (2002), Development and application of GPS signal multipath simulator, *Radio Sci.*, *37*(6), 1098, doi:10.1029/2001RS002549
- Campbell, W., and S. Matsushita (1982), Sq Currents: A Comparison of Quiet and Active Year Behavior, *J. Geophys. Res.*, *87* (A7), 5305-5308.
- Carpenter, D. L. (1966), Whistler studies of the plasmopause in the magnetosphere, 1. Temporal variations in the position of the knee and some evidence on plasma motions near the knee, *J. Geophys. Res.*, *71*(3), 693-709.
- Carpenter, D. L., and R. R. Anderson (1992), An ISEE/Whistler Model of Equatorial Electron Density in the Magnetosphere, *J. Geophys. Res.*, *97* (A2), 1097 V1108.
- Carpenter, D. L., F. Walter, R. E. Barrington, and D. J. McEwen (1968), Alouette 1 and 2 observations of abrupt changes in whistler rate and of VLF noise variations at the plasmopause - A satellite-ground study, *J. Geophys. Res.*, *73*, 2929.
- Chang, L. C., S. E. Palo, and H.-L. Liu (2009), Short-term variation of the s=1 nonmigrating semidiurnal tide during the 2002 stratospheric sudden warming, *J. Geophys. Res.*, *114*, D03109, doi:10.1029/2008JD010886.
- Chapman, S., and J. Bartels (1940), *Geomagnetism*, vols. 1, 2, Oxford University Press, New York.
- Chapman, S., and R. S. Lindzen (1970), *Atmospheric Tides*, D. Reidel, Hingham, Mass.
- Chau, J. L., B. G. Fejer, and L. P. Goncharenko (2009), Quiet variability of equatorial E x B drifts during a sudden stratospheric warming event, *Geophys. Res. Lett.*, *36*, L05101, doi:10.1029/2008GL036785.
- Chen, P.-R. (1992), Two-Day Oscillation of the Equatorial Ionization Anomaly, *J. Geophys. Res.*, *97*(A5), 6343-6357.
- Cheng, C.-Z. F., Y.-H. Kuo, R. A. Anthes, and L. Wu (2006), Satellite constellation monitors global and space weather, *EOS Trans. AGU*, *87*(17), 166.

- Cho, Y.-M., G. G. Shepherd, Y.-I. Won, S. Sargoytchev, S. Brown, and B. Solheim (2004), MLT cooling during stratospheric warming events, *Geophys. Res. Lett.*, *31*, L10104, doi:10.1029/2004GL019552.
- Coco, D. S., C. Coker, S. R. Dahlke, and J. R. Clynch (1991), Variability of GPS satellite differential group delay biases, *IEEE Trans. Aerosp. Electron. Syst.*, *27*, 931.
- Coster, A., and A. Komjathy (2008), Space Weather and the Global Positioning System, *Space Weather*, *6*, S06D04, doi:10.1029/2008SW000400.
- Crowley, G., A. Reynolds, J. P. Thayer, J. Lei, L. J. Paxton, A. B. Christensen, Y. Zhang, R. R. Meier, and D. J. Strickland (2008), Periodic modulations in thermospheric composition by solar wind high speed streams, *Geophys. Res. Lett.*, *35*, L21106, doi:10.1029/2008GL035745.
- Darrouzet, F., D. L. Gallagher, N. Andre, D. L. Carpenter, I. Dandouras, P. M. E. Decreau, J. Keyser, R. E. Denton, J. C. Foster, J. Goldstein, M. B. Moldwin, B. W. Reinisch, B. R. Sandel, and J. Tu (2009), Plasmaspheric Density Structures and Dynamics: Properties Observed by the CLUSTER and IMAGE Missions. *Space Sci. Rev.*, *145*(1-2), 55.
- Dow, J. M., R. E. Neilan, and G. Gendt (2005), The International GPS Service (IGS): Celebrating the 10th Anniversary and Looking to the Next Decade, *Adv. Space Res.*, *36*(3), 320-326, doi:10.1016/j.asr.2005.05.125.
- Doumouya, V., and Y. Cohen (2004), Improving and testing the empirical equatorial electrojet model with CHAMP satellite data, *Ann. Geophys.*, *22*, 3323-3333.
- England, S. L., S. Maus, T. J. Immel, and S. B. Mende (2006), Longitudinal variation of the E-region electric fields caused by atmospheric tides, *Geophys. Res. Lett.*, *33*, L21105, doi:10.1029/2006GL027465.
- England, S. L., X. Zhang, T. J. Immel, J. M. Forbes, and R. DeMajistre (2009), The effect of non-migrating tides on the morphology of the equatorial ionospheric anomaly: seasonal variability, *Earth Planets Space*, *61*(4), 493-503.
- England, S. L., T. J. Immel, J. D. Huba, M. E. Hagan, A. Maute, and R. DeMajistre (2010), Modeling of multiple effects of atmospheric tides on the ionosphere: An examination of possible coupling mechanisms responsible for the longitudinal structure of the equatorial ionosphere, *J. Geophys. Res.*, *115*, A05308, doi:10.1029/2009JA014894.
- Fang, T.-W., H. Kil, G. Millward, A. D. Richmond, J.-Y. Liu, and S.-J. Oh (2009), Causal link of the wave-4 structures in plasma density and vertical plasma drift in the low-latitude ionosphere, *J. Geophys. Res.*, *114*, A10315, doi:10.1029/2009JA014460.
- Fejer, B. G., J. W. Jensen, and S.-Y. Su (2008), Quiet time equatorial F region vertical plasma drift model derived from ROCSAT-1 observations, *J. Geophys. Res.*, *113*, A05304, doi:10.1029/2007JA012801.
- Fejer, B. G., M. E. Olson, J. L. Chau, C. Stolle, H. Luhr, L. P. Goncharenko, K. Yumoto, and T. Nagatsuma (2010), Lunar Dependent Equatorial Ionospheric Electrodynamic Effects During Sudden Stratospheric Warmings, *J. Geophys. Res.*, *115*, A00G03, doi:10.1029/2010JA015273.

- Field, P. R., and H. Rishbeth (1997), The response of the ionospheric F2-layer to geomagnetic activity: an analysis of worldwide data, *J. Atmos. Sol. Terr. Phys.*, 59, 163-180.
- Forbes, J. M. (1995), Tidal and Planetary Waves, in *The Upper Mesosphere and Lower Thermosphere: A Review of Experiment and Theory*, vol. 87, edited by R. M. Johnson and T. L. Killeen, 67-87.
- Forbes, J. M. (1996), Planetary waves in the thermosphere-ionosphere system, *J. Geomag. Geoelec.*, 48, 91-98.
- Forbes, J. M., and R. S. Lindzen (1976), Atmospheric solar tides and their electrodynamic effects, I, The global Sq current system, *J. Atmos. Terr. Phys.*, 38, 891-910.
- Forbes, J. M., and H. B. Garrett (1979), Theoretical studies of atmospheric tides, *Rev. Geophys. Space Phys.*, 17, 1951-1981.
- Forbes, J. M., and S. Leveroni (1992), Quasi-16 day oscillation in the ionosphere, *Geophys. Res. Lett.*, 19(10), 981-984.
- Forbes, J. M., M. E. Hagan, S. Miyahara, F. Vial, A. H. Manson, C. E. Meek, and Y. I. Portnyagin (1995a), Quasi 16-day oscillation in the mesosphere and lower thermosphere, *J. Geophys. Res.*, 100(D5),9149-9163.
- Forbes, J. M., N. A. Makarov, and Y. I. Portnyagin (1995b), First results from the meteor radar at South Pole: A large 12-hour oscillation with zonal wavenumber one, *Geophys. Res. Lett.*, 22, 3247-3250.
- Forbes, J. M., R. Guffee, S. Zhang, D. Fritts, D. Riggin, A. H. Manson, C. Meek, and R. A. Vincent (1997), Quasi 2-day oscillation of the ionosphere during the summer of 1992, *J. Geophys. Res.*, 102, 7301-7305.
- Forbes, J. M., S. E. Palo, and X. Zhang (2000), Variability of the ionosphere, *J. Atmos. Sol. Terr. Phys.*, 62, 685-693.
- Forbes, J. M., X. Zhang, and M. E. Hagan (2001), Simulations of diurnal tides due to tropospheric heating from the NCEP/NCAR Reanalysis Project, *Geophys. Res. Lett.*, 28, 3851-3854.
- Forbes, J. M., X. Zhang, E. R. Talaat, and W. Ward (2003), Nonmigrating diurnal tides in the thermosphere, *J. Geophys. Res.*, 108 (A1), 1033, doi:10.1029/2002JA009262.
- Forbes, J. M., J. Russell, S. Miyahara, X. Zhang, S. Palo, M. Mlynczak, C. J. Mertens, and M. E. Hagan (2006), Troposphere-thermosphere tidal coupling as measured by the SABER instrument on TIMED during July-September 2002, *J. Geophys. Res.*, 111, A10S06, doi:10.1029/2005JA011492.
- Forbes, J. M., X. Zhang, S. Palo, J. Russell, C. J. Mertens, and M. Mlynczak (2008), Tidal variability in the ionospheric dynamo region, *J. Geophys. Res.*, 113, A02310, doi:10.1029/2007JA012737.
- Forbes, J. M., S. L. Bruinsma, X. Zhang, and J. Oberheide (2009), Surface-exosphere coupling due to thermal tides, *Geophys. Res. Lett.*, 36, L15812, doi:10.1029/2009GL038748.
- Foster, J. C., P. J. Erickson, A. J. Coster, J. Goldstein, and F. J. Rich (2002), Ionospheric signatures of plasmaspheric tails, *Geophys. Res. Lett.*, 29(13), 1623, doi:10.1029/2002GL015067.

- Fuller-Rowell, T. J., M. V. Codrescu, R. J. Moffett, and S. Quegan (1994), Response of the Thermosphere and Ionosphere to Geomagnetic Storms, *J. Geophys. Res.*, *99*(A3), 3893-3914.
- Gallagher, D. L., P. D. Craven, and R. H. Comfort (2000), Global core plasma model, *J. Geophys. Res.*, *105*(A8), 18,819-18,833.
- Gauss, C. F. (1841), General theory of terrestrial magnetism, English translation in *Scientific Memoirs*, edited by R. Taylor, vol. 2, 184, London.
- Gibson, S. E., J. U. Kozyra, G. de Toma, B. A. Emery, T. Onsager, and B. J. Thompson (2009), If the Sun is so quiet, why is the Earth ringing? A comparison of two solar minimum intervals, *J. Geophys. Res.*, *114*, A09105, doi:10.1029/2009JA014342.
- Goldstein, J., M. Spasojevic, P. H. Reiff, B. R. Sandel, W. T. Forrester, D. L. Gallagher, and B. W. Reinisch (2003), Identifying the plasmopause in IMAGE EUV data using IMAGE RPI in situ steep density gradients, *J. Geophys. Res.*, *108*(A4), 1147, doi:10.1029/2002JA009475.
- Goldstein, J., B. R. Sandel, M. R. Hairston, and S. B. Mende (2004), Plasmopause undulation of 17 April 2002, *Geophys. Res. Lett.*, *31*, L15801, doi:10.1029/2004GL019959.
- Goncharenko, L., and S.-R. Zhang (2008), Ionospheric signatures of sudden stratospheric warming: Ion temperature at middle latitude, *Geophys. Res. Lett.*, *35*, L21103, doi:10.1029/2008GL035684.
- Grebowsky, J. M., N. C. Maynard, Y. K. Tulunay, and L. J. Lanzerotti (1976), Coincident observations of ionosphere trough and the equatorial plasmopause, *Planet. Space Sci.*, *24*, 1177-1185.
- Gringauz, K. I., and V. V. Bezrukikh (1976), Asymmetry of the Earth's plasmasphere in the direction noon-midnight from Prognoz and Prognoz 2 data, *J. Atmos. Terr. Phys.*, *38*, 1071.
- Gu, D., and S. G. H. Philander (1994), Secular Changes of Annual and Interannual Variability in the Tropics during the Past Century, *J. Climate*, *8*, 864-876.
- Gurubaran S., R. Rajaram, T. Nakamura, and T. Tsuda (2005), Interannual variability of diurnal tide in the tropical mesopause region: A signature of the El Nino-Southern Oscillation (ENSO), *Geophys. Res. Lett.*, *32*, L13805, doi:10.1029/2005GL022928.
- Hagan, M. E., and J. M. Forbes (2002), Migrating and nonmigrating diurnal tides in the middle and upper atmosphere excited by tropospheric latent heat release, *J. Geophys. Res.*, *107*(D24), 4754, doi:10.1029/2001JD001236.
- Hagan, M. E. and J. M. Forbes (2003), Migrating and nonmigrating semidiurnal tides in the upper atmosphere excited by tropospheric latent heat release, *J. Geophys. Res.*, *108*, 1062, doi:10.1029/2002JA009466.
- Hagan, M. E., and R. G. Roble (2001), Modeling diurnal tidal variability with the NCAR TIME-GCM, *J. Geophys. Res.*, *106*, 24,869-24,882.
- Hagan, M. E., A. Maute, R. G. Roble, A. D. Richmond, T. J. Immel, and S. L. England (2007), Connections between deep tropical clouds and the Earth's ionosphere, *Geophys. Res. Lett.*, *34*, L20109, doi:10.1029/2007GL030142.
- Hagan, M. E., A. Maute, and R. G. Roble (2009), Tropospheric tidal effects on the middle and upper atmosphere, *J. Geophys. Res.*, *114*, A01302, doi:10.1029/2008JA013637.

- Hartman, W. A., and R. A. Heelis (2007), Longitudinal variations in the equatorial vertical drift in the topside ionosphere, *J. Geophys. Res.*, *112*, A03305, doi:10.1029/2006JA011773.
- Hasegawa, M. (1960), On the Position of the Focus of Geomagnetic  $Sq$  Current System, *J. Geophys. Res.*, *65*(5), 1437-1447.
- Häusler, K., H. Lühr, M. E. Hagan, A. Maute, and R. G. Roble (2010), Comparison of CHAMP and TIME-GCM nonmigrating tidal signals in the thermospheric zonal wind, *J. Geophys. Res.*, *115*, D00108, doi:10.1029/2009JD012394.
- He, M., L. Liu, W. Wan, J. Lei, and B. Zhao (2010), Longitudinal modulation of the  $O/N_2$  column density retrieved from TIMED/GUVI measurement, *Geophys. Res. Lett.*, *37*, L20108, doi:10.1029/2010GL045105.
- Heise, S., N. Jakowski, A. Wehrenpfennig, Ch. Reigber, and H. Lühr (2002), Sounding of the topside ionosphere/plasmasphere based on GPS measurements from CHAMP: Initial results, *Geophys. Res. Lett.*, *29*(14), 1699, doi:10.1029/2002GL014738.
- Holton, J. R. (1980), The dynamics of sudden stratospheric warmings, *Annu. Rev. Earth Planet. Sci.*, *8*, 169-190.
- Huang, C.-S., F. J. Rich, O. de La Beaujardiere, and R. A. Heelis (2010), Longitudinal and seasonal variations of the equatorial ionospheric ion density and eastward drift velocity in the dusk sector, *J. Geophys. Res.*, *115*, A02305, doi:10.1029/2009JA014503.
- Hugentobler, U., S. Schaer, G. Beutler, H. Bock, R. Dach, A. Jaggi, M. Meindl, C. Urschl, L. Mervart, M. Rothacher, U. Wild, A. Wiget, E. Brockmann, D. Ineichen, G. Weber, H. Habrich, and C. Boucher (2004), CODE IGS Analysis Center Technical Report 2002, in *IGS 2001-2002 Technical Reports*, edited by K. Gowey, R. Neilan, and A. Moore, IGS Central Bureau, JPL, Pasadena, CA.
- Immel, T. J., E. Sagawa, S. L. England, S. B. Henderson, M. E. Hagan, S. B. Mende, H. U. Frey, C. M. Swenson, and L. J. Paxton (2006), Control of equatorial ionospheric morphology by atmospheric tides, *Geophys. Res. Lett.*, *33*, L15108, doi:10.1029/2006GL026161.
- Immel, T. J., S. L. England, X. Zhang, J. M. Forbes, and R. Demajistre (2009), Upward propagating tidal effects across the E- and F-regions of the ionosphere, *Earth, Planets and Space*, *61*, 505-512.
- Irish, K., K. Gold, G. Bonn, A. Reichert, and P. Axelrad (1998), Precision orbit determination for the Geosat Follow-on Satellites, *J. Spacecr. Rockets*, *35*(5), 336-341.
- Jadhav, G., M. Rajaram, and R. Rajaram (2002), A detailed study of the equatorial electrojet phenomenon using Oersted satellite observations, *J. Geophys. Res.*, *107*(A8), 1175, doi:10.1029/2001JA000183.
- Jin, H., Y. Miyoshi, H. Fujiwara, and H. Shinagawa (2008), Electrodynamics of the formation of ionospheric wave number 4 longitudinal structure, *J. Geophys. Res.*, *113*, A09307, doi:10.1029/2008JA013301.
- Kelley, M. C. (2009), *The earth's ionosphere: plasma physics and electrodynamics*, Academic Press, San Diego, Calif.

- Kelley, M. C., V. K. Wong, N. Aponte, C. Coker, A. J. Mannucci, and A. Komjathy (2009), Comparison of COSMIC occultation-based electron density profiles and TIP observations with Arecibo incoherent scatter radar data, *Radio Sci.*, *44*, RS4011, doi:10.1029/2008RS004087.
- Kil, H., R. DeMajistre, L. J. Paxton, and Y. Zhang (2006), Nighttime *F* region morphology in the low and middle latitudes seen from DMSP F15 and TIMED/GUVI, *J. Atmos. Sol. Terr. Phys.*, *68*, 1672-1681, doi:10.1026/j.jastp.2006.05.024.
- Kil, H., S.-J. Oh, M. C. Kelley, L. J. Paxton, S. L. England, E. Talaat, K.-W. Min, and S.-Y. Su (2007), Longitudinal structure of the vertical  $\mathbf{E} \times \mathbf{B}$  drift and ion density seen from ROCSAT-1, *Geophys. Res. Lett.*, *34*, L14110, doi:10.1029/2007GL030018.
- Kil, H., E. R. Talaat, S.-J. Oh, L. J. Paxton, S. L. England, and S.-Y. Su (2008), Wave structures of the plasma density and vertical  $\mathbf{E} \times \mathbf{B}$  drift in low-latitude *F* region, *J. Geophys. Res.*, *113*, A09312, doi:10.1029/2008JA013106.
- Klobuchar, J. A. (1996), Ionospheric Effects on GPS, in *Global Positioning System: Theory and Applications*, Vol. I, edited by B. W. Parkinson and J. J. Spilker, AIAA, 485-515.
- Kursinski, E. R., G. A. Hajj, J. T. Schofield, R. P. Linfield, and K. R. Hardy (1997), Observing Earth's atmosphere with radio occultation measurements using the Global Positioning System, *J. Geophys. Res.*, *102*(D19), 23, 429-23,465.
- Kuvshinov, A., C. Manoj, N. Olsen, and T. Sabaka (2007), On induction effects of geomagnetic daily variations from equatorial electrojet and solar quiet sources at low and middle latitudes, *J. Geophys. Res.*, *112*, B10102, doi:10.1029/2007JB004955.
- Langel, R. A., T. J. Sabaka, R. T. Baldwin, and J. A. Conrad (1996), The near-Earth magnetic field from magnetospheric and quiet-day ionospheric sources and how it is modeled, *Phys. Earth Planet. Inter.*, *98*, 235-267.
- Lastovicka, J. (2006), Forcing of the ionosphere by waves from below, *J. Atmos. Sol. Terr. Phys.*, *68*, 479-497.
- Lastovicka, J., P. Krizan, P. Sauli, and D. Novotna (2003), Persistence of the planetary wave type oscillations in foF2 over Europe, *Ann. Geophys.*, *21*, 1543-1552.
- Lastovicka, J., P. Sauli, and P. Krizan (2006), Persistence of planetary wave type oscillations in the middle ionosphere, *Annals of Geophysics*, *49*(6), 1235-1246.
- Lei, J., et al. (2007), Comparison of COSMIC ionospheric measurements with ground-based observations and model predictions: Preliminary results, *J. Geophys. Res.*, *112*, A07308, doi:10.1029/2006JA012240.
- Lei, J., J. P. Thayer, J. M. Forbes, E. K. Sutton, and R. S. Nerem (200a8), Rotating solar coronal holes and periodic modulation of the upper atmosphere, *Geophys. Res. Lett.*, *35*, L10109, doi:10.1029/2008GL033875.
- Lei, J., J. P. Thayer, J. M. Forbes, Q. Wu, C. She, W. Wan, and W. Wang (2008b), Ionosphere response to solar wind high-speed streams, *Geophys. Res. Lett.*, *35*, L19105, doi:10.1029/2008GL035208.

- Lemaire, J. F. and Gringauz, K. I. (1998), *The Earth's Plasmasphere*, Cambridge University Press, New York.
- Lichten, S. M., and J. S. Border (1987), Strategies for high-precision Global Positioning System orbit determination, *J. Geophys. Res.*, *92*, 12,751-12,762.
- Lieberman, R. S. (1991), Nonmigrating diurnal tides in the equatorial middle atmosphere, *J. Atmos. Sci.*, *48*, 112-1123.
- Lieberman, R. S., D. M. Riggin, D. A. Ortland, S. W. Nesbitt, and R. A. Vincent (2007), Variability of mesospheric diurnal tides and tropospheric diurnal heating during 1997-1998, *J. Geophys. Res.*, *112*, D20110, doi:10.1029/2007JD008578.
- Lin, C. H., W. Wang, M. E. Hagan, C. C. Hsiao, T. J. Immel, M. L. Hsu, J. Y. Liu, L. J. Paxton, T. W. Fang, and C. H. Liu (2007), Plausible effect of atmospheric tides on the equatorial ionosphere observed by the FORMOSAT-3/COSMIC: Three-dimensional electron density structures, *Geophys. Res. Lett.*, *34*, L11112, doi:10.1029/2007GL029265.
- Lindzen, R. S. (1970), Internal gravity waves in atmospheres with realistic dissipation and temperature, part I. Mathematical development and propagation of waves into the thermosphere, *Geophys. Fluid. Dyn.*, *1*, 303-355.
- Liu, H. and S. Watanabe (2008), Seasonal variation of the longitudinal structure of the equatorial ionosphere: Does it reflect tidal influences from below?, *J. Geophys. Res.*, *113*, A08315, doi:10.1029/2008JA013027.
- Liu, H.-L., and R. G. Roble (2002), A study of a self-generated stratospheric sudden warming and its mesospheric-lower thermospheric impacts using the coupled TIME-GCM/CCM3, *J. Geophys. Res.*, *107*(D23), 4695, doi:10.1029/2001JD001533.
- Liu, H.-L., W. Wang, A. D. Richmond, and R. G. Roble (2010), Ionospheric variability due to planetary waves and tides for solar minimum conditions, *J. Geophys. Res.*, *115*, A00G01, doi:10.1029/2009JA015188.
- Liu, L., M. He, W. Wan, and M.-L. Zhang (2008), Topside ionospheric scale heights retrieved from Constellation Observing System for Meteorology, Ionosphere, and Climate radio occultation measurements, *J. Geophys. Res.*, *113*, A10304, doi:10.1029/2008JA013490.
- Lodge, O. (1902), Mr Marconi's results in day and night wireless telegraphy. *Nature*, *66*, 222.
- Lomb, N. R. (1976), Least-squares frequency analysis of unequally spaced data, *Astrophys. Space Sci.*, *39*, 447-462.
- Low, N. C., T. H. Roelofs, and P. C. Yuen (1975), Electron content power spectral estimates: Periods of 2 days to 1/2 year, *Planet. Space Sci.*, *23*, 133-141.
- Lühr, H., and S. Maus (2006), Direct observation of the F region dynamo currents and the spatial structure of the EEJ by CHAMP, *Geophys. Res. Lett.*, *33*, L24102, doi:10.1029/2006GL028374.
- Lühr, H., S. Maus, and M. Rother (2004), Noon-time equatorial electrojet: Its spatial features as determined by the CHAMP satellite, *J. Geophys. Res.*, *109*, A01306, doi:10.1029/2002JA009656.

- Lühr, H., K. Häusler, and C. Stolle (2007), Longitudinal variation of F region electron density and thermospheric zonal wind caused by atmospheric tides, *Geophys. Res. Lett.*, *34*, L16102, doi:10.1029/2007GL030639.
- Lühr, H., M. Rother, K. Häusler, P. Alken, and S. Maus (2008), The influence of nonmigrating tides on the longitudinal variation of the equatorial electrojet, *J. Geophys. Res.*, *113*, A08313, doi:10.1029/2008JA013064.
- Le Sager, P., and T. S. Huang (2002), Longitudinal dependence of the daily geomagnetic variation during quiet time, *J. Geophys. Res.*, *107* (A11), 1397, doi:10.1029/2002JA009287.
- Madden, R. A. (1979), Observations of large-scale traveling Rossby waves, *Rev. Geophys.*, *17*(8), 1935-1949.
- Manney, G. L., M. J. Schwartz, K. Kruger, M. L. Santee, S. Pawson, J. N. Lee, W. H. Daffer, R. A. Fuller, and N. J. Livesey (2009), Aura Microwave Limb Sounder observations of dynamics and transport during the record-breaking 2009 Arctic stratospheric major warming, *Geophys. Res. Lett.*, *36*, L12815, doi:10.1029/2009GL038586.
- Mannucci, A. J., B. D. Wilson, D. N. Yuan, C. H. Ho, U. J. Lindqwister, and T. F. Runge (1998), A global mapping technique for GPS-derived ionospheric total electron content measurements, *Radio Sci.*, *33*(3), 565-582.
- Mannucci, A. J. B. A. Iijima, U. J. Lindqwister, X. Pi, L. Sparks, and B. D. Wilson (1999), GPS and ionosphere, in *Review of Radio Science 1996-1999*, edited by W. R. Stone, Int. Union of Radio Sci., Ghent, Belgium, 625-665.
- Mannucci, A. J., B. T. Tsurutani, B. A. Iijima, A. Komjathy, A. Saito, W. D. Gonzalez, F. L. Guarnieri, J. U. Kozyra and R. Skoug (2005), Dayside global ionospheric response to the major interplanetary events of October 29-30, 2003 "Halloween Storms", *Geophys. Res. Lett.*, *32*, L12S02, doi:10.1029/2004GL021467.
- Mannucci, A. J., B. T. Tsurutani, M. A. Abdu, W. D. Gonzalez, A. Komjathy, E. Echer, B. A. Iijima, G. Crowley, and D. Anderson (2008), Superposed epoch analysis of the day-side ionospheric response to four intense geomagnetic storms, *J. Geophys. Res.*, *113*, A00A02, doi:10.1029/2007JA012732.
- Manson, A. H., J. B. Gregory, and C. E. Meek (1981), Atmospheric waves ( $\sim 10$ min-30 days) in the mesosphere and thermosphere at Saskatoon ( $52^\circ\text{N}$ ,  $107^\circ\text{W}$ ), October 1978-September 1979, *Planet. Space Sci.*, *29*, 615-625.
- Marquardt, D. W. (1970), Generalized inverses, ridge regression, biased linear estimation and nonlinear estimation, *Technometrics*, *12*, 591-612.
- Matsuno, T. (1971), A dynamical model of the stratospheric sudden warming, *J. Atmos. Sci.*, *28*, 1479-1494.
- Matsushita, S. (1967), Solar quiet and lunar daily variation fields, in *Physics of Geomagnetic Phenomena*, chap. II-1, edited by S. Matsushita and W. Campbell, pp.301-424, Academic, New York.

- Matsushita, S., and H. Maeda (1965), On the Geomagnetic Solar Quiet Daily Variation Field during the IGY, *J. Geophys. Res.*, *70* (11), 2535-2558.
- Maus, S., C. Manoj, J. Rauberg, I. Michaelis, and H. Lühr (2011), NOAA/NGDC candidate models for the 11th generation International Geomagnetic Reference Field and the concurrent release of the 6th generation Pomme magnetic model, *Earth Planets Space*, in press.
- McDonald, S. E., K. F. Dymond, and M. E. Summers (2008), Hemispheric asymmetries in the longitudinal structure of the low-latitude nighttime ionosphere, *J. Geophys. Res.*, *113*, A08308, doi:10.1029/2007JA012876.
- McIlwain, C. E. (1961), Coordinates for Mapping the Distribution of Magnetically Trapped Particles, *J. Geophys. Res.*, *66*(11), 3681-3691.
- Mendillo, C., L. Bosheng, and J. Aarons (2000), The application of GPS observations to equatorial aeronomy, *Radio Sci.*, *35*(3), 885-904.
- Mendillo, M. (2006), Storms in the ionosphere: Patterns and processes for total electron content *Rev. Geophys.*, *44*, RG4001, doi:10.1029/2005RG000193.
- Mendillo, M., and K. Schatten (1983), Influence of Solar Sector Boundaries on Ionospheric Variability, *J. Geophys. Res.*, *88*(A11), 9145-9153.
- Millward, G. H., I. C. F. Muller-Wodarg, A. D. Aylward, T. J. Fuller-Rowell, A. D. Richmond, and R. J. Moffett (2001), An investigation into the influence of tidal forcing on F region equatorial vertical ion drift using a global ionosphere thermosphere model with coupled electrodynamics, *J. Geophys. Res.*, *106*, 24,733-24,744, doi:10.1029/2000JA000342.
- Millward, G. H., A. D. Richmond, T. J. Fuller-Rowell, and A. D. Aylward (2007), Modeling the effects of changes in the terrestrial magnetic field on the climatology of the mid- and low-latitude ionosphere, *Eos Trans. AGU*, *88*(52), Fall Mett. Suppl., Abstract SA21B-08.
- Miyoshi, Y. (2006), Temporal variation of nonmigrating diurnal tide and its relation with the moist convective activity, *Geophys. Res. Lett.*, *33*, L11815, doi:10.1029/2006GL026072.
- Moldwin, M. B., M. F. Thomsen, S. J. Barne, D. J. McComas, and K. R. Moore (1994), An Examination of the Structure and Dynamics of the Outer Plasmasphere Using Multiple Geosynchronous Satellites, *J. Geophys. Res.*, *99*(A6), 11,475-11,481.
- Moldwin, M. B., L. Downward, H. K. Rassoul, R. Amin, and R. R. Anderson (2002), A new model of the location of the plasmopause: CRRES results, *J. Geophys. Res.*, *107*(A11), 1339, doi:10.1029/2001JA009211.
- O'Brien, T. P., and M. B. Moldwin (2003), Empirical plasmopause models from magnetic indices, *Geophys. Res. Lett.*, *30*(4), 1152, doi:10.1029/2002GL016007.
- Oberheide, J., and J. M. Forbes (2008a), Thermospheric nitric oxide variability induced by nonmigrating tides, *Geophys. Res. Lett.*, *35*, L16814, doi:10.1029/2008GL034825
- Oberheide, J., and J. M. Forbes (2008b), Tidal propagation of deep tropical cloud signatures into the thermosphere from TIMED observations, *Geophys. Res. Lett.*, *35*, L04816, doi:10.1029/2007GL032397.

- Oberheide, J., Q. Wu, T. L. Killeen, M. E. Hagan, and R. G. Roble (2006), Diurnal nonmigrating tides from TIMED Doppler Interferometer wind data: Monthly climatologies and seasonal variations, *J. Geophys. Res.*, *111*, A10S03, doi:10.1029/2005JA011491.
- Oberheide, J., J. M. Forbes, K. Häusler, Q. Wu, and S. L. Bruinsma (2009), Tropospheric tides from 80 to 400 km: Propagation, interannual variability, and solar cycle effects, *J. Geophys. Res.*, *114*, D00105, doi:10.1029/2009JD012388.
- Oberheide, J., J. M. Forbes, X. Zhang, and S. L. Bruinsma (2011), Wave-driven variability in the ionosphere-thermosphere-mesosphere system from TIMED observations: What contributes to the "wave 4"? , *J. Geophys. Res.*, *116*, A01306, doi:10.1029/2010JA015911.
- Olsen, N. (1997), Ionospheric F region currents at middle and low latitudes estimated from Magsat data, *J. Geophys. Res.*, *102* (A3), 4563-4576.
- Olsen, N., T. J. Sabaka, and F. Lowes (2005), New parameterization of external and induced fields in geomagnetic field modeling, and a candidate model for IGRF 2005, *Earth Planets Space*, *57*, 1141-1149.
- Palo, S. E., M. E. Hagan, and R. G. Roble (1999), Middle atmosphere effects of the quasi-two-day wave determined from a General Circulation Model, *Earth Planets Space*, *51*, 629-647.
- Pancheva, D. and P. Mukhtarov (2010), Strong evidence for the tidal control on the longitudinal structure of the ionospheric F-region, *Geophys. Res. Lett.*, *37*, L14105, doi:10.1029/2010GL044039.
- Pancheva, D. V., et al. (2006), Two-day wave coupling of the low-latitude atmosphere-ionosphere system, *J. Geophys. Res.*, *111*, A07313, doi:10.1029/2005JA011562.
- Pancheva, D., P. Mukhtarov, and B. Andonov (2009), Nonmigrating tidal activity related to the sudden stratospheric warming in the Arctic winter of 2003/2004, *Ann. Geophys.*, *27*, 975-987.
- Pedatella, N. M., and J. M. Forbes (2010), Global structure of the lunar tide in ionospheric total electron content, *Geophys. Res. Lett.*, *37*, L06103, doi:10.1029/2010GL042781.
- Pedatella, N. M., J. M. Forbes, and J. Oberheide (2008), Intra-annual variability of the low-latitude ionosphere due to nonmigrating tides, *Geophys. Res. Lett.*, *35*, L18104, doi:10.1029/2008GL035332.
- Pedatella, N. M., J. Lei, K. M. Larson, and J. M. Forbes (2009), Observations of the ionospheric response to the 15 December 2006 geomagnetic storm: long duration positive storm effect, *J. Geophys. Res.*, *114*, A12313, doi:10.1029/2009JA014568.
- Picone, J. M., A. E. Hedin, D. P. Drob, and A. C. Aikin (2002), NRLMSISE-00 empirical model of the atmosphere: Statistical comparisons and scientific issues, *J. Geophys. Res.*, *107*(A12), 1468, doi:10.1029/2002JA009430.
- Pogoreltsev, A. I., A. A. Vlasov, K. Fröhlich, and Ch. Jacobi (2007), Planetary waves in coupling the lower and upper atmosphere, *J. Atmos. Sol. Terr. Phys.*, *69*, 2083-2101.
- Prölss, G. W. (1995), Ionospheric F-region storms, in *Handbook of Atmospheric Electrodynamics*, edited by H. Volland, CRC Press, Boca Raton, Fla.

- Rastogi, R. G., H. Chandra, and G. Sethia (1985), Solar and lunar variations in TEC at low latitudes in India, *J. Atmos. Terr. Phys.*, *47*(4), 309-317.
- Ray, J. K., and M. E. Cannon (2001), Synergy between Global Positioning System code, carrier, and signal-to-noise ratio multipath errors, *J. Guid. Contr. Dyn.*, *24*(1), 54-63.
- Ren, Z., W. Wan, J. Xiong, and L. Liu (2010), Simulated wave number 4 structure in equatorial F-region vertical plasma drifts, *J. Geophys. Res.*, *115*, A05301, doi:10.1029/2009JA014746.
- Richmond, A. D. (1989) Modeling the ionosphere wind dynamo: A review, *Pure Appl. Geophys.*, *47*, 413-435.
- Richmond, A. D. (1995a), Ionospheric Electrodynamics, in *Handbook of Atmospheric Electrodynamics*, edited by H. Volland, CRC Press, Boca Raton, Fla.
- Richmond, A. D. (1995b), Ionospheric electrodynamics using Magnetic Apex Coordinates *J. Geomagn. Geoelectr.*, *47*, 191-212.
- Richmond, A. D., and R. G. Roble (1987), Electrodynamic Effects of the Thermospheric Winds from the NCAR Thermospheric General Circulation Model, *J. Geophys. Res.*, *92* (A11), 12,365-12,376.
- Richmond, A., S. Matsushita, and J. Tarpley (1976), On the Production Mechanism of Electric Currents and Fields in the Ionosphere, *J. Geophys. Res.*, *81* (4), 547-555.
- Richmond, A. D., E. C. Ridley, and R. G. Roble (1992), A thermosphere/ionosphere general circulation model with coupled electrodynamics, *Geophys. Res. Lett.*, *19*(6), 601-604, doi:10.1029/92GL00401.
- Rishbeth, H. (1998), How the thermospheric circulation affects the ionospheric F2-layer, *J. Atmos. Terr. Phys.*, *60*, 1385-1402.
- Rishbeth, H. and O. Garriott (1967), *Introduction to ionospheric physics*, Winsdell Publishing Company, New York.
- Rishbeth, H., and R. Edwards (1989), The isobaric F2-Layer, *J. Atmos. Terr. Phys.*, *51*, 321-338.
- Rishbeth, H., and R. Edwards (1990), Modeling the F2 layer peak height in terms of atmospheric pressure, *Radio Sci.*, *25*, 757-769.
- Rishbeth, H. Muller-Wodarg, I. C. F. Zou, L., Fuller-Rowell, T. J., Millward, G. H., Moffett, R. J., Idenden, D. W., and Aylward, A. D. (2000), Annual and semiannual variations in the ionospheric F2-layer: II. Physical discussion, *Ann. Geophys.*, *18*, 945-956.
- Roble, R., R. Dickinson, and E. Ridley (1977), Seasonal and Solar Cycle Variations of the Zonal Mean Circulation in the Thermosphere, *J. Geophys. Res.*, *82*(35), 5493-5504.
- Rocken, C., Y.-H. Kuo, W. Schreiner, D. Hunt, S. Sokolovskiy, and C. McCormick (2000), COSMIC system description, *Terr. Atmos. Ocean Sci.*, *11*, 21-52.
- Ropelewski, C. F., and M. S. Halpert (1987), Global and regional scale precipitation patterns associated with the El Nino/Southern Oscillation, *Mon. Wea. Rev.*, *115*, 1606-1626.

- Rother, M. S. Choi, W. Mai, H. Luhr, and D. Cook (2004), Status of the CHAMP ME Data Processing, in *Earth Observation with CHAMP: Results from Three Years in Orbit*, edited by C. Reigber et al., pp 413-418, Springer, New York.
- Sagawa, E., T. J. Immel, H. U. Frey, and S. B. Mende (2005), Longitudinal structure of the equatorial anomaly in the nighttime ionosphere observed by IMAGE/FUV, *J. Geophys. Res.*, *100*, A11302, doi:10.1029/2004JA010848.
- Salby, M. L. (1981a), Rossby normal modes in nonuniform background configurations, Part I, Simple fields, *J. Atmos. Sci.*, *38*, 1803-1826.
- Salby, M. L. (1981b), Rossby normal modes in nonuniform background configurations, Part II, Equinox and solstice conditions, *J. Atmos. Sci.*, *38*, 1827-1840.
- Salby, Murry L. (1984), Survey of planetary-scale traveling waves: The state of theory and observations, *Rev Geophys*, *22*(2), 209.
- Scargle, J. D. (1982), Studies in astronomical time series analysis. II. Statistical aspects of spectral analysis of unevenly spaced data, *Astrophys. J.*, *263*, 835-853.
- Scherliess, L., D. C. Thompson, and R. W. Schunk (2008), Longitudinal variability of low-latitude total electron content: Tidal influences, *J. Geophys. Res.*, *113*, A01311, doi:10.1029/2007JA012480.
- Schoeberl, M. R. (1978), Stratospheric Warmings: Observations and Theory, *Rev. Geophys.*, *16*(4), 521-538.
- Schunk, R. W. (1996), *Solar-Terrestrial Energy Program: Handbook of Ionospheric Models*, edited by R. W. Schunk, Utah State University.
- Schunk, R. W. and A. F. Nagy (2000), *Ionospheres: Physics, Plasma Physics, and Chemistry*. Cambridge University Press, Cambridge.
- Schuster, A. (1889), The diurnal variation of terrestrial magnetism, *Phil. Trans. Roy. Soc. London*, *A*, *208*, 163-204.
- Sojka, J. J., W. J. Raitt, R. W. Schunk, L. Parish, and F. J. Rich (1985), Diurnal Variation of the Dayside, Ionospheric, Mid-latitude Trough in the Southern Hemisphere at 800 km: Model and Measurement Comparison, *Planet Space Sci.*, *33*(12), 1375-1382.
- Smith, T. M., R. W. Reynolds, T. C. Peterson, and J. Lawrimore (2008), Improvements to NOAA's Historical Merged Land-Ocean Surface Temperature Analysis (1880-2006), *J. Climate*, *21*, doi:10.1175/1007JCLI2100.1.
- Spasojevic, M., J. Goldstein, D. L. Carpenter, U. S. Inan, B. R. Sandel, M. B. Moldwin, and B. W. Reinisch (2003), Global response of the plasmasphere to a geomagnetic disturbance, *J. Geophys. Res.*, *108*(A9), 1340, doi:10.1029/2003JA009987.
- Sridharan, S., S. Sathishkumar, and S. Gurubaran (2009), Variabilities of mesospheric tides and equatorial electrojet strength during major stratospheric warming events, *Ann. Geophys.* *27*(11), 4125-4130.

- Stening, R. J. (1969), An assessment of the contributions of various tidal winds to the *Sq* current system, *Planet. Space Sci.*, *17*, 889-908.
- Stening, R. J. (1971), Longitude and Seasonal Variations of the *Sq* Current System, *Radio Sci.*, *6* (2), 133-137.
- Stening, R. J. (1977), Field-aligned currents driven by the ionospheric dynamo, *J. Atmos. Terr. Phys.*, *39*, 933-937.
- Stening, R. J. (1989), A calculation of ionospheric currents due to semidiurnal antisymmetric tides, *J. Geophys. Res.*, *94*(A2), 1525-1531, doi:10.1029/JA094iA02p01525.
- Stening, R. J., and B. G. Fejer (2001), Lunar tide in the equatorial F region vertical ion drift velocity, *J. Geophys. Res.*, *106*(A1), 221-226.
- Stewart, B. (1883), Hypothetical views regarding the connection between the state of the sun and terrestrial magnetism, in *Encyclopaedia Britannica*, Vol. 16, 181-184, Edinburgh.
- Takeda, M. (2002), Features of the global geomagnetic *Sq* field from 1980 to 1990, *J. Geophys. Res.*, *107*(A9), 1252, doi:10.1029/2001JA009210.
- Takeda, M., Y. Yamada, and T. Araki (1986), Simulation of ionospheric currents and geomagnetic field variations of *Sq* for different solar activity, *J. Atmos. Terr. Phys.*, *48* (3), 277-287.
- Talaat, E. R., and R. S. Lieberman (1999), Nonmigrating diurnal tides in mesospheric and lower thermospheric winds and temperatures, *J. Atmos. Sci.*, *56*, 4073-4087.
- Talaat, E. R. and R. S. Lieberman (2010), Direct observations of nonmigrating diurnal tides in the equatorial thermosphere, *Geophys. Res. Lett.*, *37*, L04803, doi:10.1029/2009GL041845.
- Tarpley, J. D. (1970), The ionospheric wind dynamo - II. Solar tides, *Planet. Space Sci.*, *18*, 1091-1103.
- Teitelbaum, H., and F. Vial (1991), On tidal variability by nonlinear interaction with planetary waves, *J. Geophys. Res.*, *96*, 14, 169-14,178.
- Thayer, J. P., J. Lei, J. M. Forbes, E. K. Sutton, and R. S. Nerem (2008), Thermospheric density oscillations due to periodic solar wind high-speed streams, *J. Geophys. Res.*, *113*, A06307, doi:10.1029/2008JA013190.
- Thuillier, G., J. W. King, and A. J. Slater (1976), An explanation of the longitudinal variation of the O<sup>1</sup>D (630 nm) tropical nightglow intensity, *J. Atmos. Terr. Phys.*, *38*(2), 155-158.
- Trenberth, K. E. (1976), Spatial and temporal variations of the Southern Oscillation, *Quart. J. R. Met. Soc.*, *102*, 639-653.
- Trenberth, K. E., J. M. Caron, D. P. Stepaniak, and S. Worley (2002), Evolution of El Niño-Southern Oscillation and global atmospheric surface temperatures, *J. Geophys. Res.*, *107*(D8), 4065, doi:10.1029/2000JD000298.
- Tsurutani, B. T., and W. D. Gonzalez (1997), The interplanetary causes of magnetic storms: A review, in *Magnetic Storms*, *Geophys. Monogr. Ser.*, vol. 98, edited by B. T. Tsurutani et al., 77-89.

- Vial, F., J. M. Forbes, and S. Miyahara (1991), Some Transient Aspects of Tidal Propagation, *J. Geophys. Res.*, *96*, 1215-1224.
- Vincent, R. A. (1990), Long-period motions in the equatorial mesosphere, *J. Atmos. Terr. Phys.*, *55*, 1067-1080.
- Vineeth, C., T. K. Pant, C. V. Devasia, and R. Sridharan (2007), Atmosphere-Ionosphere coupling observed over the dip equatorial MLTI region through the quasi 16-day wave, *Geophys. Res. Lett.*, *34*, L12102, doi:10.1029/2007GL030010.
- Wan, W., L. Liu, X. Pi, M. L. Zhang, B. Ning, J. Xiong, and F. Ding (2008), Wavenumber-4 patterns of the total electron content over the low latitude ionosphere, *Geophys. Res. Lett.*, *35*, L12104, doi:10.1029/2008GL033755.
- Wan, W., J. Xiong, Z. Ren, L. Liu, M.-L. Zhang, F. Ding, B. Ning, B. Zhao, and X. Yue (2010), Correlation between the ionospheric WN4 signature and the upper atmospheric DE3 tide, *J. Geophys. Res.*, *115*, A11303, doi:10.1029/2010JA015527.
- Werner, S., and G. W. Pröls (1997), The Position of the Ionospheric Trough as a Function of Local Time and Magnetic Activity, *Adv. Space Res.*, *20*(9), 1717-1722.
- Wilcox, J. M. (1968), The interplanetary magnetic field: Solar origin and terrestrial effects, *Space Sci. Rev.*, *8*, 258-328.
- Winch, D. E. (1981), Spherical Harmonic Analysis of Geomagnetic Tides, 1964-1965, *Phil Trans. Roy. Soc. London, A*, *303*, 1-104.
- Xue, Y., T. M. Smith, and R. W. Reynolds (2003), Interdecadal changes of 30-yr SST normals during 1871-2000, *J. Climate*, *16*, 1601-1612.
- Yanowitch, M. (1967), The effect of viscosity on gravity waves and the upper boundary condition, *J. Fluid Mech.*, *29*, 209-231.
- Yi, L., and P.-R. Chen (1993), Long period oscillations in the Equatorial Ionization Anomaly correlated with the neutral wind in the mesosphere, *J. Atmos. Terr. Phys.*, *55*(10), 1317-1323.
- Yin, P., C. N. Mitchell, P. S. J. Spencer, and J. C. Foster (2004), Ionospheric electron concentration imaging using GPS over the USA during the storm of July 2000, *Geophys. Res. Lett.*, *31*, L12806, doi:10.1029/2004GL019899.
- Yizengaw, E., and M. B. Moldwin (2005), The altitude extension of the mid-latitude trough and its correlation with plasmopause position, *Geophys. Res. Lett.*, *32*, L09105, doi:10.1029/2005GL022854.
- Yizengaw E., H. Wei, M. B. Moldwin, D. Galvan, L. Mandrake, A. Mannucci, X. Pi (2005), The correlation between mid-latitude trough and the plasmopause, *Geophys. Res. Lett.*, *32*, L10102, doi:10.1029/2005GL022954.
- Yizengaw E., M. B. Moldwin, A. Komjathy, A. J. Mannucci (2006), Unusual topside ionospheric density response to the November 2003 superstorm, *J. Geophys. Res.*, *111*, A02308, doi:10.1029/2005JA011433.

- Yizengaw, E., M. B. Moldwin, P. L. Dyson, and E. A. Essex (2007), Using tomography of GPS TEC to routinely determine ionospheric average electron density profiles, *J. Atmos. Sol. Terr. Phys.*, *69*(3), doi:10.1026/j.jastp.2006.07.023.
- Yue, X., Schreiner, W. S., Lei, J. Sokolovskiy, S. V., Rocken, C. Hunt, D. C., and Kuo, Y.-H. (2010), Error analysis of Abel retrieved electron density profiles from radio occultation measurements, *Ann. Geophys.*, *28*, 217-222, doi:10.5192/angeo-28-217-2010.
- Zhang, J., et al. (2007), Solar and interplanetary sources of major geomagnetic storms ( $D_{st} \leq -100$  nT) during 1996-2005, *J. Geophys. Res.*, *112*, doi:10.1029/2007JA012321.
- Zhang, X., J. M. Forbes, M. E. Hagan, J. M. Russell III, S. E. Palo, C. J. Mertens, and M. G. Mlynczak (2006), Monthly tidal temperatures 20-120 km from TIMED/SABER, *J. Geophys. Res.*, *111*, A10S08, doi:10.1029/2005JA011504.